Motion at the Nanoscale in Polymer Solutions with Application to Biophysical Problems

Thesis by

Krzysztof Sozański

prepared under supervision of

prof. dr hab. Robert Hołyst

within the International PhD Studies at the
Institute of Physical Chemistry of the Polish Academy of Sciences
Department of Soft Condensed Matter and Fluids
Kasprzaka 44/52, 01-224 Warsaw

Warsaw, March 2015

"Forty-two,"
said Deep Thought,
with infinite majesty and calm.

– Douglas Adams,
The Hitchhiker's Guide to the Galaxy

Acknowledgements

I would never have gotten along the scientific path to this point if it was not for a few very special people:

my Father, who planted in me insatiable curiosity, sharing his urge for understanding the ways of nature without settling for superficial explanations;

prof. Robert Hołyst, who has been much more than just a boss and advisor, infecting me with his obsession for genuine science as a true and inspiring mentor;

dr Jan Paczesny and **dr Tomasz Kalwarczyk**, who taught me the tricks of the researcher's trade, treating me as a friend rather than a student and forcing me to think and invent rather than follow commands and reproduce.

This Thesis is your accomplishment as much as it is mine.

I gracefully acknowledge all my other co-workers who were involved in the work described herein: **Agnieszka Wiśniewska, dr Tomasz Piasecki, dr Karol Waszczuk, dr Anna Ochab-Marcinek, prof. Teodor Gotszalk, Felix Ruhnow, prof. Stefan Diez,** and **dr Marcin Tabaka**.

I would also like to express my gratitude for all my colleagues from the **Soft Matter Group** for their sincere support and great help, as well as for making the time of my PhD studies enjoyable and joyful.

This work was supported by
the Ministry of Science and Higher Education of Poland
within the Diamond Grant DI2011 015341

and by the National Science Centre
within the Maestro Grant 2011/02/A/ST3/00143.

List of publications

Publications directly related to the Thesis

1. K. Sozański, A. Wiśniewska, T. Kalwarczyk, R. Hołyst, *Activation Energy for Mobility of Dyes and Proteins in Polymer Solutions: From Diffusion of Single Particles to Macroscale Flow*, Physical Review Letters **111**:228301, 2013 (IF=7.94)

2. K. Sozański, A. Wiśniewska, T. Piasecki, K. Waszczuk, A. Ochab-Marcinek, T. Gotszalk, R. Hołyst, *A Depletion Layer in Polymer Solutions at an Interface Oscillating at the Subnano- to Submicrometer Scale*, Soft Matter **10**:7762, 2014 (IF=4.15)

3. K. Sozański, F. Ruhnow, A. Wiśniewska, M. Tabaka, S. Diez, R. Hołyst, *Small Crowders Slow Down Kinesin-1 Motors by Increasing the Local Viscosity*, submitted, 2015

Other publications

4. J. Paczesny, P. Nitoń, A. Żywociński, K. Sozański, R. Hołyst, M. Fiałkowski, R. Kieffer, B. Glettner, C. Tschierske, D. Pociecha, E. Górecka, *Stable, Ordered Multilayers of Partially Fluorinated Bolaamphiphiles at the Air-Water Interface*, Soft Matter **8**:5262, 2012 (IF=3.91)

5. J. Paczesny, K. Sozański, A. Żywociński, R. Hołyst, B. Glettner, R. Kieffer, C. Tschierske, K. Nikiforov, D. Pociecha, E. Górecka, *Spontaneous Self-Assembly of Partially Fluorinated Bolaamphiphiles into Ordered Layered Structures*, Physical Chemistry Chemical Physics **14**:14365, 2012 (IF=3.83)

6. J. Paczesny, K. Sozański, I. Dzięcielewski, A. Żywociński, R. Hołyst, *Formation of Net-Like Patterns of Gold Nanoparticles in Liquid Crystal Matrix*

at the Air-Water Interface, Journal of Nanoparticle Research **14**:826, 2012 (IF=2.18)

7. J. Paczesny, A. Kamińska, W. Adamkiewicz, K. Winkler, K. Sozański, M. Wadowska, I. Dzięcielewski, R. Hołyst, *Three Steps of Hierarchical Self-Assembly Toward a Stable and Efficient Surface Enhanced Raman Spectroscopy Platform*, Chemistry of Materials **24**:3667, 2012 (IF=8.24)

8. J. Paczesny, M. Wójcik, K. Sozański, K. Nikiforov, C. Tschierske, A. Lehmann, E. Górecka, J. Mieczkowski, R. Hołyst, *Self-Assembly of Gold Nanoparticles into 2D Arrays Induced by Bolaamphiphilic Ligands*, Journal of Physical Chemistry C **117**:24056, 2013 (IF=4.81)

9. D. Kałuża, W. Adamiak, T. Kalwarczyk, K. Sozański, M. Opałło, M. Jönsson-Niedziółka, *Anomalous Effect of Flow Rate on the Electrochemical Behavior at a Liquid/Liquid Interface Under Microfluidic Conditions*, Langmuir **29**:16034, 2013 (IF=4.19)

10. A. Wiśniewska, K. Sozański, T. Kalwarczyk, K. Kędra-Królik, C. Pieper, S. A. Wieczorek, S. Jakieła, J. Enderlein, R. Hołyst, *Scaling of Activation Energy for Macroscopic Flow in Poly(Ethylene Glycol) Solutions: Entangled – Non-Entangled Crossover*, Polymer **55**:4651, 2014 (IF=3.77)

11. T. Kalwarczyk, K. Sozański, S. Jakieła, A. Wiśniewska, E. Kalwarczyk, K. Kryszczuk, S. Hou, R. Hołyst, *Length-Scale Dependent Transport Properties of Colloidal and Protein Solutions for Prediction of Crystal Nucleation Rates*, Nanoscale **17**:10340, 2014 (IF=6.74)

12. X. Zhang, A. Poniewierski, S.Hou, K. Sozański, A. Wiśniewska, S. A. Wieczorek, T. Kalwarczyk, L. Sun, R. Hołyst, *Tracking Structural Transitions of Bovine Serum Albumin in Surfactant Solutions by Fluorescence Correlation Spectroscopy and Fluorescence Lifetime Analysis*, Soft Matter **11**:2512, 2015 (IF=4.15)

13. T. Kalwarczyk, K. Sozański, A. Ochab-Marcinek, J. Szymański, M. Tabaka, S. Hou, R. Hołyst, *Motion of Nanoprobes in Complex Liquids*, submitted, 2015

Patents

14. J. Paczesny, K. Sozański, R. Hołyst, I. Dzięcielewski, A. Żywociński, W. Adamkiewicz, *Sposób pokrywania powierzchni ciała stałego nanocząstkami*, P-395009, 2014 (also submitted and accepted in Switzerland as *Verfahren zur Beschichtung von Festkörperoberfläche mit Nanopartikeln und nach dem Verfahren beschichtete Festkörperoberfläche*, CH 705019, 2014)

15. J. Paczesny, K. Sozański, A. Żywociński, W. Adamkiewicz, I. Dzięcielewski, K. Winkler, A. Kamińska, R. Hołyst, *Sposób pokrywania powierzchni ciała stałego dwuwymiarową siecią nanocząstek i powierzchnia ciała stałego pokryta tym sposobem*, P-397169, 2014

16. J. Paczesny, K. Sozański, I. Dzięcielewski, W. Adamkiewicz, K. Winkler, A. Żywociński, A. Kamińska, R. Hołyst, *Platforma do pomiarów SERS oraz sposób jej wykonania*, P-397249, 2014

Contents

List of essential symbols and abbreviations

A_i	initial amplitude of oscillations of the quartz tuning fork (QTF)
a	scaling parameter of the order of unity
b	scaling parameter of the order of unity
c	concentration
d_{RMS}	root mean square displacement of polymer mesh during a single QTF oscillation period
D	diffusion coefficient
D_0	diffusion coefficient in pure solvent
Đ	dispersity, traditionally known as polydispersity index (PDI)
E_{a}	activation energy
ΔE_{a}	difference in activation energy for mobility between solution and pure solvent
$G(\tau)$	autocorrelation function (ACF)
h	Planck constant
I	signal intensity
$\mathbf{J}$	diffusion flux vector
K	spring constant
k	reaction rate
M_{n}	number-average molecular weight
M_{w}	weight-average molecular weight
M_{z}	Z-average molecular weight

N_A	Avogadro constant
n	index of refraction
p	fraction of molecules in the triplet state (in FCS)
$\mathbf{q}$	wave vector
R	gas constant
$\langle\mathbf{R}\rangle$	mean end-to-end vector (polymer chain size measure)
R_eff	effective probe radius (see Equation 1.27)
R_g	radius of gyration
R_h	hydrodynamic radius of crowders
r_p	hydrodynamic radius of a probe
T	absolute temperature
t	time
t_c	decay time of QTF oscillations
V_det	volume of Gaussian detection spheroid (in FCS)
v	kinesin stepping velocity
v_mol	molar volume
w_0	beam waist (in FCS)
z_0	size of the detection volume along the beam direction (in FCS)
α	electromechanical coupling coefficient
γ	system-dependent energy scaling coefficient (see page 69)
η	dynamic viscosity
η_0	solvent viscosity
η_eff	effective, size-dependent viscosity
θ	scattering angle
κ	detection volume structure parameter (in FCS)
λ	laser wavelength
ν	Flory scaling exponent
ξ	correlation length
Π	osmotic pressure
τ	lag time

τ_{D}	characteristic diffusion time (in FCS or DLS)
τ_{t}	triplet state lifetime
τ_{osc}	oscillation period of the QTF
τ_{shear}	shear stress
χ	Flory interaction parameter
ω	radial frequency

ACF	autocorrelation function
ATP	adenosine triphosphate
DL	depletion layer
DLS	dynamic light scattering
DNA	deoxyribonucleic acid
FCS	fluorescence correlation spectroscopy
GFP	green fluorescent protein
GPC	gel permeation chromatography
MSD	mean square displacement
MT	microtubule
NA	numerical aperture
PEG	polyethylene glycol
QCM	quartz crystal microbalance
QTF	quartz tuning fork
SPAD	single photon avalanche photodiode
SSE	Stokes-Sutherland-Einstein (equation)
TCSPC	time-correlated single photon counting
TetraEG	tetraethylene glycol
TIRF	total internal reflection fluorescence

Abstract

All living organisms, irrespective of the level of biological complexity, are from the point of view of physical chemistry dynamic, far-from-equilibrium systems. The recent rapid development of biochemistry and molecular biology revealed in detail the chemical structure of these systems – both in terms of constitution and function of different molecular species, as well as biochemical pathways connecting them into functional items. A new arising challenge is to capture the dynamics, grounding the intricate regulation and synchronization mechanisms in the basis of thermodynamics. This, however, cannot be achieved without an accurate description of passive and active matter transport at molecular and mesoscopic level. In case of complex systems, whose transport properties are strongly length-scale-dependent, it is not trivial. The hereby presented Thesis is an experiment-based contribution to elucidation of this issue.

Convenient model complex systems used throughout the Thesis are aqueous polymer solutions, where the crucial length scales are clearly defined. Moreover, such solutions are of high interest *per se* due to broad industrial applications and recent dynamic development of polymer sciences. Within this experimental framework, a few related problems are investigated and discussed. The main theses are as follows:

1. Diffusion is an activated process. In case of complex liquids, activation energy for diffusion depends on the probe size and structure of the liquid; this relationship is equivalent to the viscosity scaling and can be utilized to

assess interactions in complex systems;

2. At short time scales, the rate of response of the polymer mesh to mechanical disturbances determines the effective viscosity of the solution. Due to a depletion-layer-like effect, oscillators overrunning the polymer relaxation experience viscosity reduced by orders of magnitude compared to the steady state value;

3. Viscosity scaling is crucial for active transport. Model motor protein, kinesin, comes to a stall upon a moderate increase of activation energy for diffusion of its domains. Such behaviour confirms a mechanism of the protein's processive motion which implies ubiquitous exploitation of Brownian diffusion in natural molecular machines.

The text is divided into five chapters. Chapter 1 gives a comprehensive introduction to the topic and presents the current state of knowledge on transport properties of complex liquids. Chapter 2 provides background on the experimental techniques utilized in the presented studies: fluorescence correlation spectroscopy (FCS), rheometry, dynamic light scattering (DLS), quartz tuning fork oscillation decay and total internal reflection fluorescence (TIRF) microscopy. In Chapter 3, technical details on all the performed experiments are given. Chapter 4 contains experimental results along with their discussion, grouped according to the three main theses listed above. Finally, Chapter 5 gives a brief overview of the obtained results and final conclusions.

Streszczenie

Organizmy żywe, niezależnie od stopnia biologicznej złożoności, są z fizykochemicznego punktu widzenia dynamicznymi układami dalekimi od stanu równowagi. Rozwój biochemii i biologii molekularnej przyniósł w ostatnich dekadach odpowiedzi na wiele pytań dotyczących struktury i funkcji biologicznie istotnych cząstek oraz szlaków przemian chemicznych łączących je w funkcjonalną całość. Nowym wyzwaniem staje się zbadanie dynamiki żywych układów: zrozumienie, jak z podstawowych praw termodynamiki wynikają złożone mechanizmy regulacji i synchronizacji procesów metabolicznych. Krokiem w tym kierunku jest stworzenie uniwersalnego, ilościowego opisu transportu materii na poziomie molekularnym i mezoskopowym. W wypadku złożonych układów, których właściwości silnie zależą od skali długości, problem ten jest nietrywialny. Niniejsza praca ma na celu doświadczalne zbadanie jego wybranych aspektów.

W rozprawie opisywane są głównie eksperymenty na układach modelowych – wodnych roztworach polimerów. Charakteryzują się one precyzyjnie określonymi wewnętrznymi skalami długości, co ułatwia poszukiwanie fizycznych zależności ilościowych. Ponadto, roztwory tego typu stanowią przedmiot zainteresowania dynamicznie rozwijającej się gałęzi fizykochemii polimerów. Modele eksperymentalne wykorzystane są tutaj w celu zbadania kilku powiązanych zagadnień. Główne tezy stawiane w rozprawie brzmią następująco:

1. Dyfuzja jest procesem aktywowanym. W wypadku płynów złożonych, energia aktywacji dyfuzji jest funkcją rozmiaru próbnika (dyfundującej cząstki)

oraz struktury płynu złożonego (charakterystycznych skal długości). Zależność ta jest powiązana ze skalowaniem lepkości i może być wykorzystywana do oceny oddziaływań międzycząsteczkowych.

2. W odpowiednio krótkiej skali czasu, efektywna lepkość odczuwana przez obiekt poruszający się w roztworze polimeru zależy od szybkości relaksacji sieci polimerowej. W roztworze polimeru w pobliżu granicy faz występuje efekt tzw. warstwy zubożonej (*depletion layer*), a szybkość odbudowy tej warstwy w odpowiedzi na bodźce mechaniczne determinuje efektywną lepkość roztworu. Mikrooscylator „prześcigający" relaksację otoczenia może więc pracować przy oporze hydrodynamicznym mniejszym o rzędy wielkości od oczekiwanego na podstawie makroskopowej lepkości płynu, co może mieć znaczenie m. in. dla mechanoenzymów.

3. Lokalna lepkość jest kluczowym parametrem dla transportu aktywnego. Kinezyna, będąca modelowym silnikiem molekularnym, przestaje działać już przy niewielkim podniesieniu bariery energetycznej dla dyfuzji jej domeny funkcyjnej. Jest to potwierdzeniem postulowanego mechanizmu ruchu kinezyny, który wykorzystuje ruchy Browna.

Tekst podzielony jest na pięć rozdziałów. Rozdział 1 to zwarte wprowadzenie do tematyki badań i oparta o dostępną literaturę prezentacja aktualnego stanu wiedzy na temat właściwości transportowych płynów złożonych. W Rozdziale 2 opisane są podstawy teoretyczne i zasady działania technik eksperymentalnych wykorzystywanych w ramach niniejszej pracy: spektroskopii korelacji fluorescencji, reometrii rotacyjnej, dynamicznego rozpraszania światła, elektromechanicznych pomiarów lepkości oraz mikroskopii fluorescencyjnej całkowitego wewnętrznego odbicia. W Rozdziale 3 zebrane są detale techniczne dotyczące aparatury, odczynników i procedur eksperymentalnych. Rozdział 4 zawiera wyniki pomiarów wraz z ich szczegółową dyskusją, przedstawione zgodnie z trzema głównymi tezami pracy. Rozdział 5 stanowi natomiast krótkie podsumowanie wyników, podkreślając kluczowe wnioski i rysując perspektywę ich dalszego wykorzystania.

Chapter 1

Introduction

In this chapter, the essential notions of diffusion (Section 1.1) and viscosity (Section 1.2) are introduced. The fundamental Stokes-Sutherland-Einstein equation, connecting these two notions, is presented – along with the issues concerning its application to complex liquids. In Section 1.4, a brief overview of the physical description of polymer solutions – which are used as model complex liquids – is given. On this basis, the empirical viscosity scaling paradigm (Section 1.5) is presented. Next, Eyring's approach placing molecular motion within the framework of activated processes is discussed (Section 1.3). Finally, a model system of active cellular transport is introduced (Section 1.7).

1.1 Diffusion

Scientific investigations of diffusion date back to the experiments of Thomas Graham from the 1820s [1, 2]. He observed that chemically different gases tend to *diffuse through each other* when brought into contact. Although the notion of diffusion coefficient had not been introduced yet, Graham's experiments provided quantitative data on mobility of different gases, which later on proved to be surprisingly accurate [3]. It was also Graham who first systematically investigated diffusion in liquids, showing that it was slower than is gases by orders of magnitude.

Fick's Laws

The foundation of physical description of molecular diffusion was laid by Adolf Fick in the 1850s [4]. He treated diffusion as a simple process of transfer of mass, analogous to flow of heat and electric current – which in fact come down to transfer of thermal energy and charge, respectively. The process is caused by a gradient of concentration present in a system. Diffusion occurring against the concentration gradient is a manifestation of the system's tendency to maximization of entropy (which is realized by even distribution of particles across the whole system). Spontaneous diffusive flux is described by two differential equations, known as Fick's laws.

Fick's first law concerns a steady state, where the concentration gradient is constant in time. It is written as

$$\mathbf{J} = -D\nabla c. \tag{1.1}$$

$\mathbf{J}$ is here the diffusion flux vector, whose value is interpreted as the amount of substance crossing a unit area in a unit time. c is the concentration, given as amount of substance per volume unit (in case of nonideal solutions, activity should be used instead of concentration). D is a proportionality factor, originally described

by Fick as *a constant dependent upon the nature of the substances* [4] – currently known as the diffusion coefficient. Expressed in $m^2 \cdot s^{-1}$, it is a basic measure of mobility of molecular species.

Fick's second law was derived following Fourier's approach to heat transfer and the matter conservation principle [3]. It is a second degree partial derivative equation, which in a concise form can be written as

$$\frac{\partial \phi}{\partial t} = D\nabla^2 \phi \ . \tag{1.2}$$

The equation refers to the situation when concentration gradient is not constant. It is therefore useful for description of changes of concentration with time, t, caused by diffusion.

Fick also pointed out a dependence between rates of diffusion and temperature, suggesting however that it was not a simple one. To properly understand the temperature dependence of diffusion coefficients, it is necessary to look into the underlying molecular mechanism.

Diffusion and Brownian Motion

Usually, diffusion is interpreted as macroscopic spreading of a substance in a medium against the concentration gradient, which is described by Fick's laws. However, at a molecular level, it is nothing by random Brownian motion of particles – evening out the concentration across the system is not due to some specific force pulling the particles towards the lower concentration region, but solely due to the stochasticity of their movements.

The first observation of random motions of microscopic objects is attributed to Robert Brown. The simple experiments, meticulously described in Brown's 1827 paper [5], were originally intended as a study of reproduction mechanisms in plants. Using a simple microscope, Brown noticed that pollen grains suspended in water constantly perform random movements. To his surprise, he found that not only pollen freshly collected from living plants, but also dried or immersed in spirit

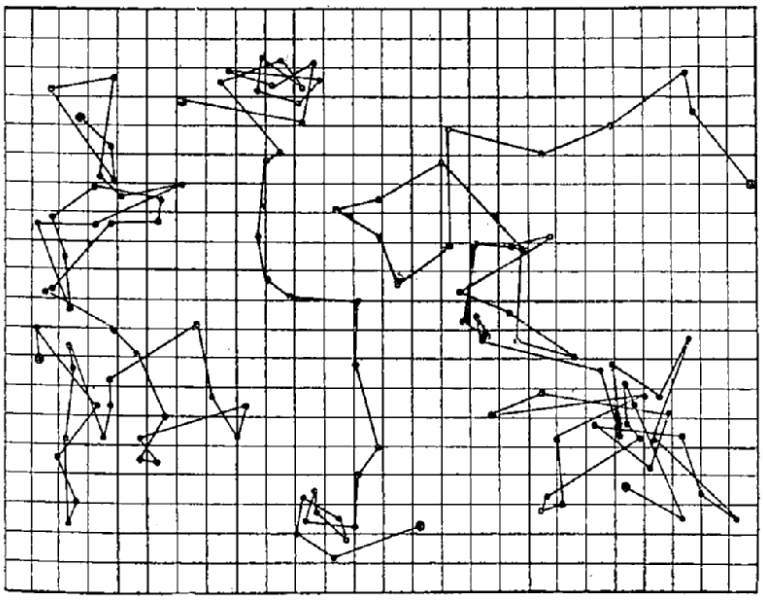

Figure 1.1: 2-dimensional projection of random movements of a grain of mastic of diameter of 0.53 μm in solution. Points correspond to the particle's positions observed at 30 s intervals; mesh size is 3.2 μm. Figure reproduced from a 1913 book by Jean Perrin [12], p. 165.

exhibited such behaviour. Brown extended his experiments to a great variety of different organic and non-organic substances (including wood, coal, glass, as well as various minerals and metals), observing constant motion for any powder fine enough to be suspended in water, irrespective of its chemical nature. The key, revolutionary conclusion was that the motion was a universal property of dispersed fine matter rather than a manifestation of some kind of *vis vitalis* and could not be interpreted as an evidence of the particles being animated [6].

In his papers, Brown did not attempt to provide a physical explanation for the observed particle movements. The theory was developed at the beginning of the XXth century, independently by William Sutherland [7], Albert Einstein [8,9], and Marian Smoluchowski [10, 11]. Interestingly, Einstein learned about Brown's experimental results after he derived from the molecular-kinetic theory of heat the equations that actually describe them.[1]

[1]Einstein explicitly made such statement in his letter to Michele Besso from Jan 6th, 1948.

The trajectories of particles undergoing Brownian motion are random (at sufficiently long time scales), as depicted in Figure 1.1. The momentary velocity and direction of a particle is determined by a resultant force of impacts of surrounding particles. However, since the frequency of collisions of a particle diffusing in a liquid is of the order of 10^{21} per second [13], it is not convenient to describe this motion within the framework of classical mechanics. Since Brownian motion is fractal in nature, the length of actual path travelled by a given particle in a given period of time is not known [14]. However, it is possible to asses the mobility of the particle within an approach where the average extent of space probed by the particle during a given time is measured. It is given by the mean square displacement (MSD):

$$\mathrm{MSD} = \langle (\mathbf{r}(t) - \mathbf{r}(0))^2 \rangle \ . \tag{1.3}$$

$\mathbf{r}(t)$ denotes the position of a particle at time t. Einstein's derivation of the description of Brownian motion from diffusion equations [8] yields

$$\mathrm{MSD} = \epsilon D t, \tag{1.4}$$

where ϵ is a dimensionality parameter equal to 2, 4, or 6 for 1-, 2-, or 3-dimensional diffusion, respectively. Thus, the diffusion coefficient, originally being a proportionality constant describing miscibility rates of fluids, gains a direct molecular interpretation.

The basic picture of diffusion as a random walk with sharp changes of direction (as in Figure 1.1) does not hold at the extremely short time and length scales, where single collisions between particles are considered: if the speed or direction of an object was to change discontinuously, it would require an infinite force [15]. It was already suggested by Einstein [9] that in such situation, where the inertia plays a key role, a model of ballistic motion is more accurate [15] and the particle actually follows a smooth path. However, to observe such behaviour an extremely high spatial and temporal resolution is necessary (sub-nm and ns, respectively). It was not until the 2010s that the hypothesis of ballistic motion was confirmed

experimentally, first in gasses at low pressure [16], then also in liquids [14]. Such model of motion at sub-nm length scales is interesting from the physical point of view and may be relevant to binding in some biological processes [15] and molecular recognition mechanisms. However, at the length and time scales accessible using the methods applied within this Thesis, only the regime of the diffusive motion can be discussed.

It should be stressed that Fickian diffusion is a manifestation of stochastic thermal motion of molecules. Therefore, even at equilibrium conditions diffusion in liquids still occurs (with concentration gradients locally generated by fluctuating molecules). In such case, the rate of this process is given by the self-diffusion coefficient, D^* [17]:

$$D^* = D\frac{\partial \ln c}{\partial \ln A}, \tag{1.5}$$

where c and A denote concentration and activity of a given species, respectively. Since in the experiments described in this Thesis tracer molecules are mostly used at low concentrations (of the order of 10^{-9} M in case of fluorescence correlation spectroscopy), an infinite dilution approximation is relevant and D^* is treated as equivalent to D.

1.2 Viscosity

Diffusion coefficient is a notion often used in a context of motion of single particles. On the other hand, viscosity is usually understood as a macroscopic property of a fluid, applied under the assumption that the fluid is a uniform, continuous medium. Later on (in Section 1.5), it will be shown that such division is not obligatory and viscosity-based description can also prove useful at molecular length-scales. However, a classical definition of fluid viscosity needs to be introduced first.

Let us take a system where uniform fluid is placed between two flat planes, as in Figure 1.2. The bottom plane is immobile, while the top one is moved along

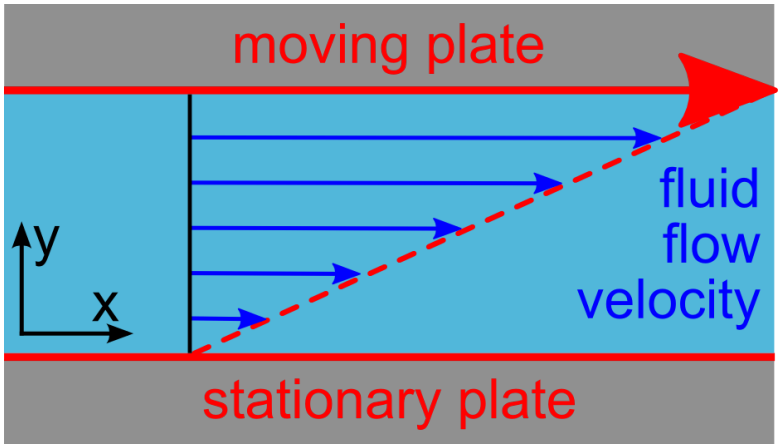

Figure 1.2: Idealized scheme of laminar flow between a mobile and a stationary plane. Top plane is moved along the x axis at a velocity v_0. A gradient of velocity of motion of the fluid appears along the y direction.

a given direction at a velocity of v_0. The flow is laminar and no edge effects are observed. The fluid can then be considered as an assembly of layers parallel to the planes of infinitesimal thickness. Momentum is transferred between these layers due to friction (according to a molecular interpretation, fluid particles randomly move along the y direction, thus transferring the x component of their momentum between the layers [18]). In such case, a gradient of velocity along the direction normal to the planes is observed, $\frac{\partial v}{\partial y}$, which is defined as shear rate. To maintain a constant motion of the top plate, a constant force per unit area of the plate needs to be applied along the x direction to balance the losses of energy due to friction. This force per unit area is denoted as shear stress, τ_{shear}. As was originally expressed by Isaac Newton, the magnitude of shear stress is proportional to the velocity gradient:

$$\tau_{\text{shear}} = \eta \frac{\partial v}{\partial y}. \tag{1.6}$$

The proportionality constant η appearing in the above equation is the dynamic viscosity of the fluid. In simple terms, η can be interpreted as a measure of internal friction in a fluid, *i.e.* its resistance against flow. An analogous concept, frequently applied while analysing the Reynolds numbers, is the kinematic viscosity, defined

as the ratio of dynamic viscosity to the fluid density [17]. However, to avoid confusion, it will not be used throughout this thesis – the notion of viscosity should be understood here as dynamic viscosity, η, unless specifically stated otherwise.

In most simple fluids, η is independent of the shear stress. These are called Newtonian fluids, since they obey Newton's law of viscosity (Equation 1.6) with η as a simple numeric parameter (at a given temperature). However, there's a number of fluids whose behaviour deviates from this law significantly, generally designated as non-Newtonian. In case of shear thickening liquids, viscosity increases with the shear stress – which is why a ball of *Silly Putty* can withstand a hit with a hammer, but is easily modelled by hand when gently touched, or why one could run across a pool of starch solution, but would sink if tried to walk slowly. An opposite effect is observed in shear thinning liquids – which is why modern paints wet the painted surface well (the shear of the brush decreases their viscosity), but do not drip or flow after application. Generally, such non-Newtonian effects are often due to interactions on a mesoscopic scale; therefore, they are frequently observed in complex liquids.

1.3 Activation Energy for Mobility

The key concept underlying the modern understanding of chemical kinetics is that all reactions are activated processes: irrespective of the total Gibbs free energy of the reaction, some energy must be first delivered to the system to overcome an activation barrier [18]. On the free energy landscape, this barrier is a saddle separating local minima, corresponding to substrates and products (which is explained at the molecular level by the transition state theory). The canonic equation connecting the magnitude of the barrier – *i.e.* the activation energy, E_a – with the reaction rate, k, was coined by Svante Arrhenius in 1889 [19]. In a basic form, it is expressed as

$$k = A \exp\left(\frac{-E_\mathrm{a}}{RT}\right) , \tag{1.7}$$

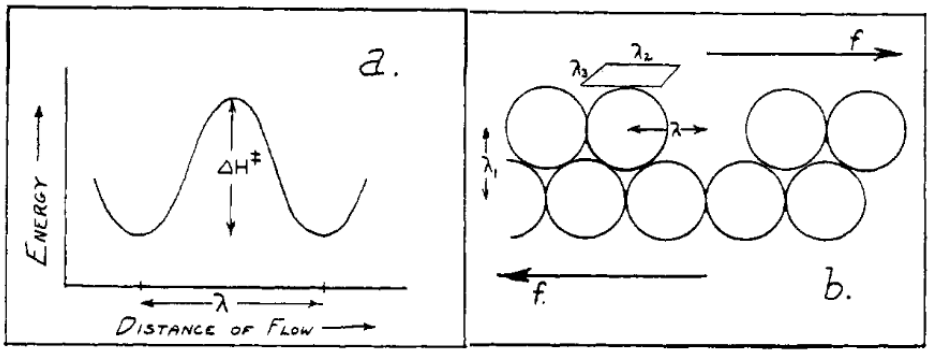

Figure 1.3: Reproduction of a figure from a 1940 paper by Kauzmann and Eyring [23], picturing viscous flow as an activated process. Liquid flow is regarded as combination of single acts of translation of molecules in a semi-crystalline lattice. The diffusing particle needs empty space to jump to and acquire enough energy to overcome the energetic barrier.

where A is a numeric pre-exponential factor, R is the gas constant, and T is the absolute temperature. Soon after the publication of Arrhenius' work it was found that his formulation is very general and can be applied to processes other than chemical reactions. In 1922 Dushman and Langmuir proposed an Arrhenius-like equation for diffusion:

$$D = A \exp\left(\frac{-E_\mathrm{a}}{RT}\right) \ . \tag{1.8}$$

A complete description of diffusion within the absolute reaction rate theory was given by Henry Eyring [20, 21]. In this model molecules are treated as interacting hard spheres, while the fluid is a pseudo-crystalline assembly of such spheres. Diffusion is considered as a series of single, discrete acts of translation of a molecule from one equilibrium state to an adjacent one. For such a movement to occur, a hole must first be created into which the molecule can move (since two molecules cannot occupy the same space), which is the slow step of the process. Additional energy is also required to break the weak bonds between the particle and its neighbours to allow for the movement (see Figure 1.3). The total probability of a single movement act is therefore a product of probabilities of acquiring enough energy by the particle and creation of a hole in its vicinity [22].

Eyring drew an analogy between molecular diffusion and vaporization, as during the flow of molecules same intermolecular bonds are broken as in vaporization. On the other hand, there is no entropy gain and no pressure-volume work is done. It was suggested that the energy of activation of diffusion can be estimated as 1/2.45 of the heat of vaporization for simple liquids [21, 24].

In macroscopic viscous flow, momentum is transferred between molecular layers of the liquid due to diffusion of particles in the direction perpendicular to the flow. Therefore, viscous flow can be described – similarly as diffusion – within the absolute reaction rate theory, as an activated process. According to Erring, viscosity of a simple fluid can be expressed as [20, 24]

$$\eta = \frac{N_{\mathrm{a}} h}{v_{\mathrm{mol}}} \exp\left(\frac{E_{\mathrm{a}}}{RT}\right) \ , \tag{1.9}$$

where h – Planck constant, v_{mol} – molar volume. To avoid using negative values of E_{a}, the minus sign is removed from the exponent in the above notation (it should be noted that viscosity is what opposes the activated diffusive motion of a particle). The E_{a} values calculated using Equation 1.9 proved to be in agreement with the estimations based on heat of vaporization for some liquids [21, 24].

The key point of the single movement act of a particle is creation of a hole in its vicinity. From the statistical point of view, such holes appear due to local fluctuations of the fluid density. In 1970, Turnbull and Cohen [25] developed from this idea the free volume theory. According to this theory, the distribution of free volume within the liquid is such that the overall entropy of the system is maximized. Such approach was merged with Eyring's absolute reaction rate theory to provide a description of diffusion and viscosity within the paradigm of statistical thermodynamics [22, 26]. Both theoretical and experimental efforts were made to develop the model and prove its validity, allowing for accurate explanation of temperature dependencies of viscosity and diffusion coefficients (see *e.g.* references [27–30]). However, no previous literature record of application of the reaction rate theory to viscosity and diffusion in complex liquids is available.

1.4 Polymer Chains in Solutions

In case of simple substances, at least two distinct fluid phases can be observed: gas and liquid. For more complex systems, comprising highly anisotropic particles or flexible macromolecules, even in the liquid state a wide variety of phases and structures can be found, which greatly influences their physical properties. Such systems are referred to as *complex fluids* [31]. A key role is played therein by interactions at the mesoscopic scale, *i.e.* at the nano- or even micrometer range.

Polymer solutions are frequently used as model complex liquids. The spatial structure of a linear polymer chain can be fairly easily described and therefore the crucial length-scales of the liquid can be estimated. This facilitates the analysis of any structure-related phenomena and enables quantitative physical conclusions. Moreover, properties of polymer melts and solutions are of great general interest to different branches of industry. Therefore, polymer solutions are also a system of choice for the investigations described in this thesis.

The main feature distinguishing polymers from other forms of matter is the extent of the covalent structure of a single polymer particle, many times greater than in case of particles of simple compounds [32]. The hypothesis of covalent structure of polymer particles was introduced by Hermann Staudinger in 1920 [33], opening the field of polymer science – beforehand, substances such as starch or rubber had been considered as colloids, interconnected by van der Waals forces. The basic physical theory of long chains was then developed during the 1930s and 1940s, notably by Debye, Kuhn, and Flory. Below, a short summary of the basic concepts concerning the structure of polymers in solutions is presented.

Polymer Chain Models

Since single polymer chains are composed of a great number of atoms – frequently exceeding 10^6 – it is not feasible to explicitly describe or model their structure. However, chains are composed of small repetitive units, monomers [17], which can

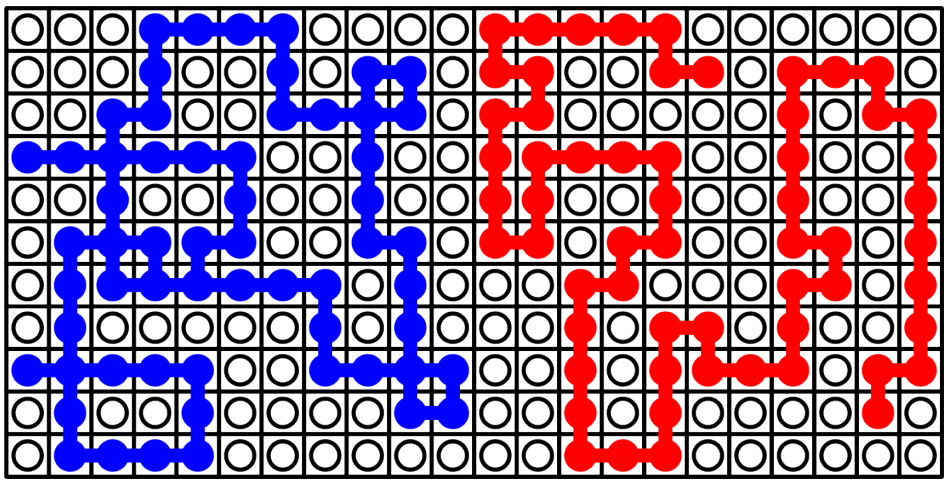

Figure 1.4: Random walk model of a polymer chain on a 2D square lattice: blue – ideal random chain; red – real chain, including the excluded volume.

be treated as basic building blocks. In more coarse-grained models, even larger segments are used, which dramatically simplifies the description of a polymer chain. For example, if segments of length corresponding to the Kuhn length are considered, they can be thought of as freely jointed and randomly oriented, independent of the conformation of other segments. Such treatment removes from the model the local restrictions imposed on the backbone of the chain by possible rotational angles of the chemical bonds and steric interactions. Persistence length – being one half of the Kuhn length – is the length-scale above which the chain can be considered as a uniform, elastic thread [34]. Such chain assumes in a solution a structure of a random coil [35].

Random coil can be easily modelled. Chain segments are placed on a discrete lattice instead of continuous space. Figure 1.4 depicts a simplest case of a 2-dimensional square lattice. Interconnected segments occupy nodes and are placed along a random walk path – *i.e.*, subsequent segments of the chain are located at neighbouring nodes, but the choice on nodes (direction of chain propagation on the lattice) is random. In this ideal chain case, it is possible for the chain to „return" to the same node. However, two physical monomers cannot occupy the same space – which is why an excluded volume model (Figure 1.4, red chain) is introduced

to describe real chains. The ideal chain model includes only interactions between monomers placed at short distances along the polymer backbone (neighbouring monomers). However, the chain is elastic and may form loop-like structures. Then, even monomers separated by a long stretch of the chain may happen to be in a close proximity in a given chain conformation and interact with each other. Such interactions are included in the real chain model. They have a crucial influence on the statistical description of the behaviour of the polymer.

Polymer-Solvent Interactions

A quantitative measure of the excluded volume effect is given by the dimensionless Flory parameter, χ. It is a measure of the enthalpy of mixing of pure polymer and solvent. χ multiplied by the $k_{\mathrm{B}}T$ energetic term (Boltzmann constant times temperature) gives the difference in energy of a solvent molecule in pure solvent and in pure polymer. [36] If the polymer-solvent interactions are favourable, $\chi < 0.5$, the system is in the good solvent regime and coil swelling is observed: the gyration radius, R_{g}, of the polymer coil increases respective to the random walk model value due to extensive penetration of the coil by solvent molecules. If $\chi > 0.5$, the poor solvent effect is observed: coil becomes compressed, as polymer-polymer interactions are favoured. $\chi = 0.5$ is referred to as θ conditions (satisfied for a given polymer-solvent system at a given θ temperature) [35]. In such case, the chain behaves ideally and the real R_{g} is equal to the value expected by the random walk model with zero excluded volume (ideal chain). Solvent quality (understood in terms of χ value) is also related to the solubility of the polymer: for good solvent conditions, high solubility is expected (up to gelation at high polymer concentration, or full miscibility for short polymers).

Concentration Regimes

Even in a relatively simple case of polymer dissolved in a good solvent, a number of qualitatively different mesoscale structures may be observed, depending on the chain length and concentration. Polymer solutions are therefore assigned to the so-called concentration regimes. According to the simplest handbook division, there are three main concentration regimes: dilute, semi-dilute and concentrated [35,37].

In the dilute regime polymer chains are well separated from each other, forming random coils (Figure 1.5a). The dynamics of the chain is heavily influenced by hydrodynamic interactions, so that the Zimm model is applicable [38,39]. The coils can be treated as hard spheres [40] (which can however be penetrated by the solvent). It has been suggested that the coil size varies slightly with polymer concentration in this regime due to the shrinking effect [41,42]. It happens so due to repulsive interactions between monomers belonging to different chains: coils shrink to minimize the occupied volume fraction and, consequently, repulsion. Light scattering and viscometric studies [43–45] implied existence of a critical concentration above which the coil shrinking effect becomes prominent. On this basis, a subdivision of the dilute regime has been suggested to distinguish the extremely dilute regime [41–43]. Such solutions approach in fact the infinite di-

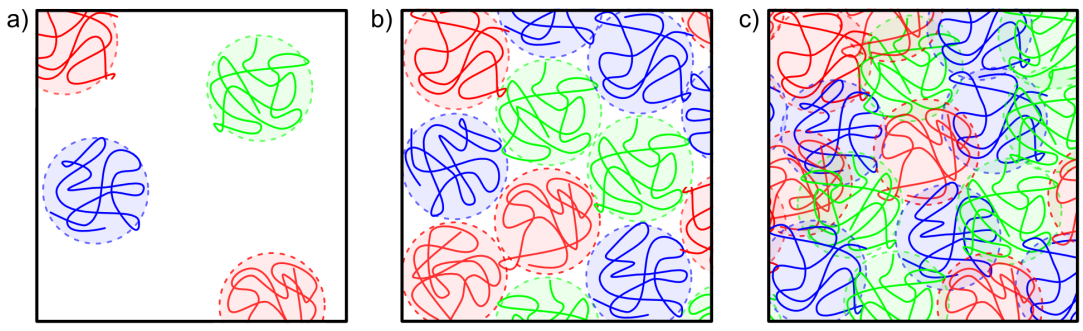

Figure 1.5: 2D cartoon model of flexible polymer solution at different concentrations. a) Coils are separated from each other – dilute regime; b) At overlap concentration, c^*, coils fill all the available space; c) In the semi-dilute regime coils start to overlap and entangle.

lution model and are potentially interesting from the theoretical point of view. However, due to low polymer concentration, this regime is hardly accessible for detailed experimental studies and does not seem to be of significant practical interest. Therefore, the extremely dilute regime will not be further discussed within this thesis and all solutions where polymer coils are separated from each other will be simply referred to as dilute.

As the polymer concentration is increased, the system enters the semi-dilute regime, where coils are no longer separated, forming a uniform mesh. The crossover between these two regimes is referred to as the overlap concentration, c^* [35,37,46], and defined as

$$c^* = \frac{M_\mathrm{w}}{4/3\pi R_\mathrm{g}^3 N_\mathrm{A}} \ , \tag{1.10}$$

where M_w – weight-average molecular weight, R_g – gyration radius of the polymer coil, N_A – Avogadro constant. At the overlap concentration the whole available volume is occupied by polymer coils (they are in contact), however, they do not interpenetrate each other significantly (Figure 1.5b). Although c^* marks a crossover in the dynamic behaviour of the polymer system, it should not be treated as a sharp boundary [47,48]. Alternate definitions of c^* have been proposed [35,49,50] that provide estimates sightly different than Equation 1.10. Moreover, the slight concentration dependence of R_g may impair exact calculation of c^*.

Recently it has been pointed out that the actual shift in flow and scaling properties of polymer solutions may correspond not to the onset of overlap, but rather to entanglement of the chains [51]. In an entangled solution [34] not only do the coil volumes overlap, but also the number of contact points between chains is high enough to obtain a uniform mesh of topologically constrained chains (Figure 1.5c). Chain entanglements may have a crucial influence on the physical properties of solutions [52]. According to Graessley *et al.* [49], the semi-dilute regime should be subdivided to semi-dilute entangled and semi-dilute non-entangled. However, the definitions of critical concentrations of overlap and entanglement are still debated upon and the crossovers represent rather a gradual change than a rapid shift.

Moreover, overlap and entanglement limits do not seem to be clearly separated and may both constitute a single, continuous crossover from dilute, non-entangled to semi-dilute, entangled systems [51]. Therefore, throughout this thesis only the dilute–semi-dilute division is taken into consideration. The definition of c^* from Equation 1.10 is applied as a convenient estimate of the crossover point between the concentration regimes.

With further increase of the polymer volume fraction above the semi-dilute regime, the concentrated regime is reached, where the system approaches polymer melt conditions. The chains are then assumed to be ideal. However, since most biologically and applicationally relevant complex systems fall within the semi-dilute conditions, the concentrated regime will not be discussed within this thesis in detail. It can be regarded as an ideal limiting case for the described studies.

Polymer Chain Dimensions and Length-Scales

For a physical description of polymer solutions it is crucial to introduce robust measures of the coil size. The scaling approach heavily relies on proper definition of crucial length-scales defining the macromolecular mesh. Below, the basic measures of polymer chain dimensions are introduced [34,35]. A graphical summary is given in Figure 1.6.

Let us consider a homopolymer consisting of N monomers. $\mathbf{s_i}$ is a vector corresponding to the backbone fragment of the i-th monomer. Although the monomers are randomly oriented in space (within the bounds imposed by the possible rotation angles of the chemical bonds within the backbone), their lengths are equal ($|\mathbf{s}_1| = |\mathbf{s}_2| = ... = |\mathbf{s}_N| = l$). In such case, we can define the chain contour length as $L = Nl$. L is therefore the maximum length of the fully extended chain. It can be experimentally assessed by means of single molecule AFM, which is particularly interesting for protein mechanics and folding studies [53, 54], but has also been applied to linear homopolymers such as polyethylene glycol [55].

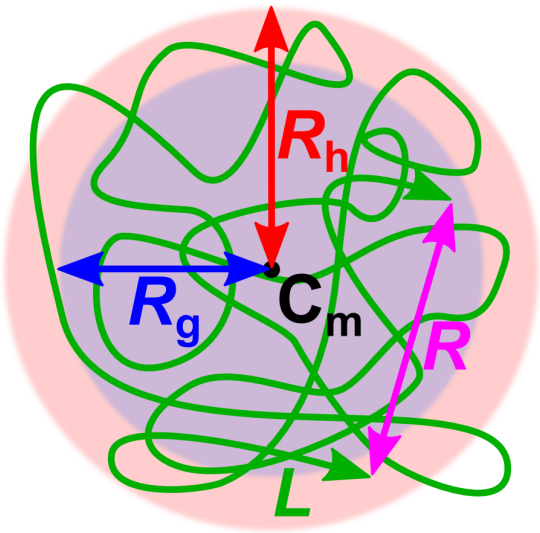

Figure 1.6: Schematic representation of the key parameters describing the size of a polymer chain (green) in solution. R_g – gyration radius, R_h – hydrodynamic radius, R – end-to-end distance, L – contour length, C_m – centre of mass.

Flexible and semi-flexible polymers in solutions do not adopt an extended conformation, but form coil-like structures, whose dimensions are far below L. If a vector sum of $\mathbf{s}_i$ is calculated and averaged across all possible chain conformations (averaging denoted here by angle brackets), the mean end-to-end vector $\langle \mathbf{R} \rangle$ is obtained:

$$\langle \mathbf{R} \rangle = \left\langle \sum_{i=1}^{N} \mathbf{s}_i \right\rangle = \langle \mathbf{r}_N - \mathbf{r}_1 \rangle. \tag{1.11}$$

$\mathbf{r}_1$ and $\mathbf{r}_N$ refer to positions of both end monomers in an arbitrary coordinate system. Mean end-to-end distance R is calculated as $\sqrt{\langle \mathbf{R}^2 \rangle}$. In contrast to L, the value of R does carry information about the actual coil size in solution. However, a more universal and easier to use measure of coil dimension is its radius of gyration, R_g. It is a square root of the second moment around the centre of mass of the chain [35]. Centre of mass $\mathbf{r}_G$ is calculated as

$$\mathbf{r}_G = \frac{1}{N} \sum_{i=1}^{N} \mathbf{r}_i, \tag{1.12}$$

with assumption that monomers are treated as material points. Then, R_g is given

by

$$R_{\mathrm{g}} = \sqrt{\frac{1}{N}\sum_{i=1}^{N}\langle(\mathbf{r}_i - \mathbf{r}_G)^2\rangle}. \tag{1.13}$$

Summation and averaging are interchangeable here. If the total weight of the chain is m, the product mR_{g} gives the total moment of inertia of the coil. R_{g} can be regarded as the radius of the sphere occupied by the polymer chain. It is possible to measure it experimentally using scattering techniques, such as static light scattering (SLS) [56] or neutron/X-ray scattering in case of small molecules (radius below ∼50 nm).

Another measure of the coil size is its hydrodynamic radius, R_{h}. It is defined as radius of an equivalent hard sphere diffusing at the same rate as the polymer coil. Coil is therefore approximated here as a perfect, isolated sphere, subject to laminar flow of the solvent, while the hydrodynamic radius is given by the magnitude of hydrodynamic friction (*i.e.* based on the Stokes-Sutherland-Einstein equation; see Section 1.5). Although the values of R_{g} and R_{h} are usually of the same order of magnitude, $R_{\mathrm{h}} > R_{\mathrm{g}}$ since in the hydrodynamic radius hydration sphere, as well as shape- and flow-related effects are also included.

The radii defined above refer to single polymer coils. However, in the semi-dilute regime a transient network of loosely connected chains is formed and the key length-scale is the mesh size of this network. A quantitative definition of this length-scale, introduced by de Gennes [37], is the correlation length, ξ:

$$\xi = R_{\mathrm{g}}\left(\frac{c}{c^*}\right)^{-\beta}. \tag{1.14}$$

c is here the polymer concentration and β is a scaling parameter. In a good solvent, ξ in the semi-dilute regime depends only on c and not on the chain length. At the overlap concentration, the mesh size is comparable to the gyration radius of the coil. To satisfy both the above conditions, the β exponent must equal 3/4 [37]. β is related to the swelling parameter ν [37, 57, 58]:

$$\beta = \frac{-\nu}{1-3\nu}. \tag{1.15}$$

ν connects the coil size to the molecular weight of the polymer: $R_{\mathrm{g}} \propto M_{\mathrm{w}}^{\nu}$. It accounts for the excluded volume interactions. For a three-dimensional coil in a good solvent ν is equal to 3/5 [40], which is in agreement with the β value of 0.75.

The correlation length corresponds to the blob size in the reptation theory of de Gennes [37]. It can be interpreted as the mean radius of a sphere centred at a given monomer, in which only monomers belonging to the same chain are found. Therefore, it is also a measure of the distance between entanglements of the chains.

Definitions of Molecular Weight of Polymers

The aforementioned parameters are defined for a perfect situation where the length of polymer chains is well defined and uniform. However, in real experiments the parameters should be rather treated as an average over all polymer coils present in the sample. It is an important issue, appearing due to a non-zero width of distribution of N (number of monomers in a chain). Although modern synthesis techniques, such as living polymerization [59], allow for good control over the process, a perfect monodispersity of the product is hardly ever obtained and precise separation of chains of a given length is usually not feasible.[2] Therefore, polymer samples are usually described not by the number of monomers, but by average molecular weight (which is easy to measure, along with its distribution, by chromatographic methods). Depending on the chosen way of averaging, the sample can be described by number-, weight-, or Z-average molecular mass (M_{n}, M_{w},and M_{z}, respectively). If N_{i} is the amount of chains of molecular weight of M_{i} in the sample, the averages are given by:

$$M_{\mathrm{n}} = \frac{\sum_i N_i M_i}{\sum_i N_i} \; ; \tag{1.16}$$

[2] A notable exception is natural synthesis of some biopolymers, such as proteins, where a nearly perfect uniformity – both in terms of length as well as tertiary structure of the molecules – is obtained. In this case complex, enzyme-based systems of transfer of biochemical information and synthesis control are involved. However, biohomopolymers synthesised *in vivo* whose exact structure is not essential for the cell viability, such as polysaccharides, usually present broad molecular weight distribution.

$$M_{\mathrm{w}} = \frac{\sum_i N_i M_i^2}{\sum_i N_i M_i} \ ; \tag{1.17}$$

$$M_{\mathrm{z}} = \frac{\sum_i N_i M_i^3}{\sum_i N_i M_i^2} \ . \tag{1.18}$$

M_{n} is the ordinary arithmetic mean of molecular weight of chains. It can be measured by gel permeation chromatography, nuclear magnetic resonance or viscometry. M_{w} can be obtained from scattering experiments. Large molecules have more impact on its value than the smaller ones. Finally, in case of Z-average the balance is shifted even more towards long chains. M_{z} is experimentally determined by means of ultracentrifugation. Overall, different experimental methods yield different averages due to the nature of physical effects they are based on. Although the discrepancies between the three averages may be significant, the relation $M_{\mathrm{n}} \leqslant M_{\mathrm{w}} \leqslant M_{\mathrm{z}}$ is always satisfied.

A measure of uniformity of a polymer sample is dispersity,[3] $Đ_{\mathrm{M}}$. It is calculated as a ratio of weight- to number-average molecular mass:

$$Đ_{\mathrm{M}} = \frac{M_{\mathrm{w}}}{M_{\mathrm{n}}}. \tag{1.19}$$

In case of a perfectly uniform polymer, $Đ_{\mathrm{M}}$=1. The higher the $Đ_{\mathrm{M}}$ value is, the less uniform the polymer.

1.5 Viscosity Scaling

Usually, viscosity is treated as a macroscopic property of a liquid, while diffusion is referred to motion at the molecular scale. However, there is an intimate relation between these two values, known as the Stokes-Sutherland-Einstein equation. While its application to simple liquids is straightforward, in case of complex systems it requires an advanced approach where effective viscosity is related to the system's length-scales.

[3]Dispersity is equivalent to polydispersity index, PDI, which has been used traditionally. However, the latter expression is currently discouraged by IUPAC [60].

Stokes-Sutherland-Einstein (SSE) Equation

In the theoretical works on Brownian motion, Smoluchowski [10] and Einstein [8] included the temperature dependence of the diffusion rates. The developed equation, currently known as the Einstein-Smoluchowski equation, can be written in a generalized form as [61]

$$D = \mu k_{\mathrm{B}} T, \tag{1.20}$$

where the μ coefficient is interpreted as the ratio of the probe's velocity $\mathbf{v}$ to the force $\mathbf{F}$ applied to it. If a model system of perfectly spherical probe diffusing in a fluid of a low Reynolds number (laminar flow) is applied, μ can be substituted using the Stokes' law:

$$\mathbf{F} = 6\pi\eta r_{\mathrm{p}}\mathbf{v} \qquad \Rightarrow \qquad \mu = \frac{1}{6\pi\eta r_{\mathrm{p}}}, \tag{1.21}$$

where r_{p} denotes the probe radius. Then, a fundamental relation known as the Stokes-Sutherland-Einstein (SSE) equation is obtained:

$$D = \frac{k_{\mathrm{B}} T}{6\pi\eta r_{\mathrm{p}}} \ . \tag{1.22}$$

It should be noted that according to the original interpretation of the SSE equation, viscosity is a parameter characteristic for a fluid at given conditions (set temperature and pressure, measurement at zero-shear conditions).

Apparent Breakdown of the SSE Equation in Complex Liquids

From the point of view of statistical thermodynamics, the SSE equation belongs to the class of fluctuation-dissipation relations [62]. The diffusing probe experiences drag (*i.e.* viscosity of the environment), which causes dissipation of its kinetic energy, while heat is produced. The corresponding fluctuation is the Brownian motion. According to the fluctuation-dissipation theorem [63], diffusion coefficient is inversely proportional to the friction experienced during the motion – and,

consequently, to the viscosity. Therefore, if we denote the values corresponding to pure solvent with a „0" index, the diffusion coefficient D of a given probe in a complex liquid and the viscosity of this liquid η should follow the dependence:

$$\frac{\eta}{\eta_0} = \frac{D_0}{D}. \tag{1.23}$$

Probably the first experimental results undermining the above equation were published in a 1952 letter by Schachman and Harrington [64]. The authors studied sedimentation rates of different colloidal particles (such as polystyrene beads or viruses) in solutions of deoxyribonucleic acid (DNA) during ultracentrifugation. For small probes they observed sedimentation rates significantly higher that what was expected from the measurements of macroscopic viscosity of the solutions. They suggested that the large probes (for which no anomalies in sedimentation times were observed) needed to disrupt the macromolecular mesh, while the small ones could diffuse through the mesh much easier – which later proved to be a valid explanation.

The breakdown of the SSE equation in complex liquids was intensively studied by means of various methods including sedimentation during ultracentrifugation [65, 66], fluorescence recovery after photobleaching [67], pulsed field gradient nuclear magnetic resonance [68], holographic interferometry [69], capillary electrophoresis [70–72], and dynamic light scattering [73]. In all cases, in complex liquids a dramatic drop in viscosity was observed for sufficiently small probes. However, it was found that the validity of the SSE equation was retained for all systems on condition that viscosity was treated not as a constant, but as a function of probe size [74]. Throughout this thesis, such scale-dependent, effective viscosity experienced by the probe is denoted as η_{eff} to avoid confusion with macroscopic viscosity η (which is the large probe limit for η_{eff}). A general dependence, which currently is widely agreed upon [37, 67, 74–82], is a stretched exponential:

$$\eta_{\text{eff}} \propto \exp\left(r_{\text{p}}^{a}\right), \tag{1.24}$$

where a is a parameter of the order of unity. In such case, Equation 1.23 ought to be rewritten for complex liquids as

$$\frac{\eta_{\text{eff}}}{\eta_0} = \frac{D_0}{D}. \tag{1.25}$$

Although most of the aforementioned studies on breach of the SSE relation focused on polymer solutions, the effects of length-scale dependence of viscosity are also pronounced in other complex systems, such as hard-sphere-like colloids [83–86], micellar systems [87] and protein solutions [86,88,89]. Importantly, analogous observations were also made for diffusion in model biological systems, such as cytoplasm of *E. coli* [90] and HeLa cells [91].

Scaling in Polymer Solutions

It was observed that probes diffusing in polymer solutions experience macroscopic viscosity when the probe radius exceeds the radius of gyration of the polymer coil, *i.e.* $r_{\text{p}} > R_{\text{g}}$ [92–94]. In 2009, Hołyst *et al.* published a study on polyethylene glycol solutions, comparing macroscopic viscosity data with local viscosity experienced by nanoscopic probes, measured by capillary electrophoresis and fluorescence correlation spectroscopy [95]. A scaling relation was suggested in a two-case form:

$$\frac{\eta_{\text{eff}}}{\eta_0} = \begin{cases} \exp\left(b\left(\frac{r_{\text{p}}}{\xi}\right)^a\right), & \text{if} \quad r_{\text{p}} < R_{\text{g}} \\ \exp\left(b\left(\frac{R_{\text{g}}}{\xi}\right)^a\right), & \text{if} \quad r_{\text{p}} > R_{\text{g}} \end{cases}. \tag{1.26}$$

a and b are parameters of the order of unity. In the second case, macroscopic viscosity is reproduced: $\eta_{\text{eff}} = \eta$, if $r_{\text{p}} > R_{\text{g}}$. The polymer gyration radius was designated as the crossover length-scale between the „macro" and „nano" regimes, which was supported by studies of nanoparticle mobility [94]. Such result was also in line with results of probe mobility measurements in micellar systems, where the crossover was found at a length-scale of the order of the micelle persistence length [87]. Theoretical predictions by Cai *et al.* [96], based on the reptation

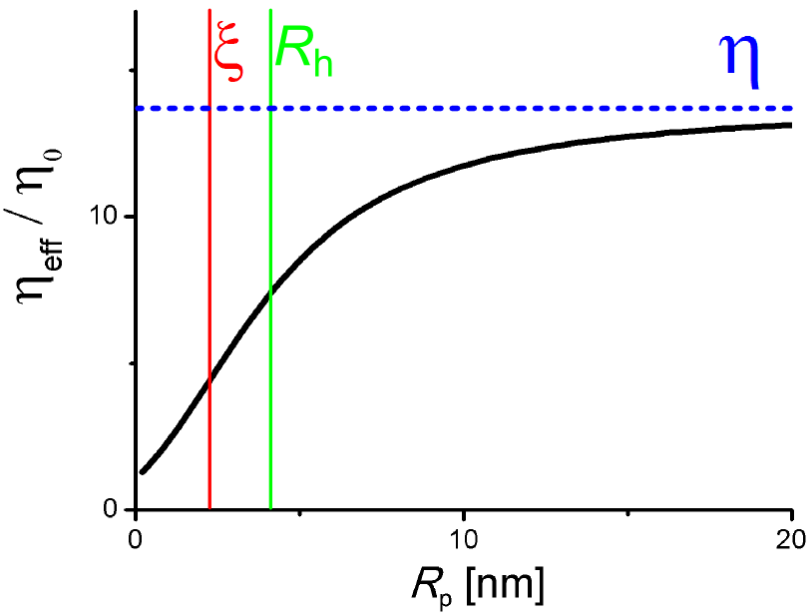

Figure 1.7: Exemplary scaling curve, plotted according to Equation 1.28 for a 10% polyethylene glycol aqueous solution. Effective viscosity η_{eff} (scaled by solvent viscosity, η_0) increases with the probe radius r_{p} and approaches macroscopic viscosity η in the large probe limit. The crossover from the „nano" to the „macro" range is gradual and smooth.

model, suggested two distinct crossover length-scales, corresponding to the correlation length and tube diameter in the entangled system.

The scaling form was amended by Kalwarczyk *et al.* [97] by introduction of the notion of effective radius R_{eff}, defined by the equation:

$$R_{\text{eff}}^{-2} = R_{\text{h}}^{-2} + r_{\text{p}}^{-2}. \tag{1.27}$$

This led to modification of the scaling equation to

$$\frac{\eta_{\text{eff}}}{\eta_0} = \exp\left[b\left(\frac{R_{\text{eff}}}{\xi}\right)^{a}\right]. \tag{1.28}$$

Importantly, the above equation covers the whole probe size range, from small particles to macroscopic probes. Instead of a sharp crossovers at given length-scales, it features a gradual, continuous shift in the effective viscosity with changing probe size. The shape of the resultant η_{eff} *vs.* r_{p} curve is depicted in Figure 1.7. Equation 1.28 proved to be applicable not only to polymer solutions, but also to probe diffusion in HeLa and Swiss 3T3 cells [97].

1.6 Depletion Layer Effect

Another phenomenon important for description of motion in polymer systems, complimenting the viscosity scaling, is the depletion layer (DL) effect. It is defined as a decrease of polymer concentration in solution in proximity of a non-adsorbing surface [98, 99], as depicted in Figure 1.8. The origin of this effect is entropic [100, 101]. A polymer chain located in direct proximity of the solution boundary (centre of mass of the chain less than R_g from the wall) exhibits limited conformational freedom – since the chain cannot penetrate the wall, some chain arrangements are prohibited. This decreases the conformational entropy of the chain, thus making such location of a chain thermodynamically unfavourable. Depletion interactions were first observed during experimental analysis of aggregation processes [102], since they promote interactions between objects immersed in a polymer solution. Although the thickness of the depletion layer is of the order of the gyration radius of a polymer coil (typically, in the range of nm), its existence has profound consequences for *e.g.* flocculation processes [101], mobility in complex systems [103], as well as rates of biochemical reactions [104].

It was suggested that the DL effect contributes to the enhancement of probe

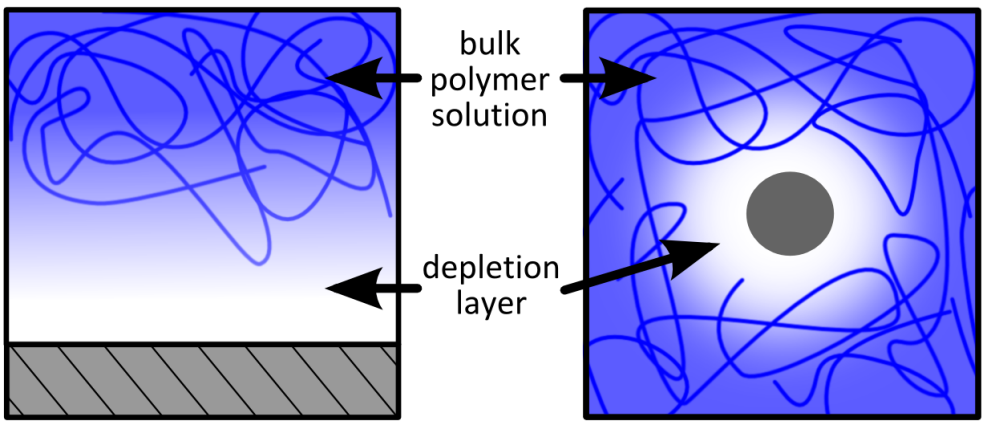

Figure 1.8: Schematic representation of a depletion layer in a polymer solution near a flat plane (left) and microsphere (right).

diffusion in complex liquids [105, 106]. This is due to the fact that at the probe surface the polymer concentration is lowered, and therefore the local viscosity is decreased. A depletion layer forming around the probe corresponds to a viscosity gradient. The locally reduced viscosity facilitates rotational diffusion, as well as translational diffusion at short time scales (when the probe only moves within the DL bounds) [105]. However, at long time scales, also the movement of the DL through the bulk solution is observed. The movement of the DL together with the particle was first discussed theoretically by Odijk [107]. Ochab-Marcinek and Hołyst [108] postulated a *walking confined diffusion* model, where the probe motion is characterized by two diffusion coefficients, corresponding to the motion of the probe within the DL and motion of the whole depleted sphere (see Figure 1.8b). The model was further adjusted to account for polymer flexibility and polydispersity [109] and merged with the viscosity scaling approach [89, 110]. The DL was included in the scaling model by modification of the R_{eff} definition. However, it only resulted in a numeric correction, while the general scaling form was preserved. Moreover, the DL effect was substantial only when $r_{\mathrm{p}} \approx R_{\mathrm{h}}$. In case of motion of probes significantly larger or smaller than the coil size, the DL influence could be disregarded.

The depletion layer has been viewed and modelled exclusively as a static phenomenon, occurring at the surface of an immobile plane/sphere [111, 112] or around a diffusing particle [101, 108, 113]. Even in the latter case, a silent assumption has been made that depletion is an equilibrium state and its size and properties can be therefore treated as constant. However, due to the elasticity of the polymer mesh and its non-zero relaxation time, its dynamics should also be considered. Although the DL at flat interfaces has been directly observed by optical methods [114–117], none of these experiments allowed to probe the dynamics of the DL or capture the response of the polymer to mechanical stimuli.

1.7 Kinesin – Model Molecular Motor

Diffusion is the foundation of all biological systems of passive transport. However, there is also a wide range of active transport systems, where the motion of (macro)molecular cargo does not necessarily occur against the concentration gradient, but requires external supply of energy. Usually, active transport is associated with transmembrane proteins, acting as ATP-powered pumps [118], which produce concentration gradients – such as *e.g.* the sodium-potassium pump. However, there is also another class of active transport, used in eukaryotic cells to move cargo over relatively large distances. It is based on mechanoenzymes walking along microtubules, which constitute the cellular scaffolding. A model, ATP-dependent protein of this kind is kinesin-1 [119–121]. It is capable of binding and pulling cargo, such as *e.g.* vesicles. Kinesins play a key role during cell division.

The motor domain of the Kinesin-1 consists of two identical globular subunits, referred to as heads, connected to the stalk via a flexible neck linker [123]. The stalk is a coiled-coil at whose end tail domain is located, where cargo can be bound. Schematic structure of a dimerised kinesin is presented in Figure 1.9. Kinesin moves along microtubules – asymmetric (polar) filaments composed of coiled strands of α- and β-tubulin. The movement is realized by distinct, single

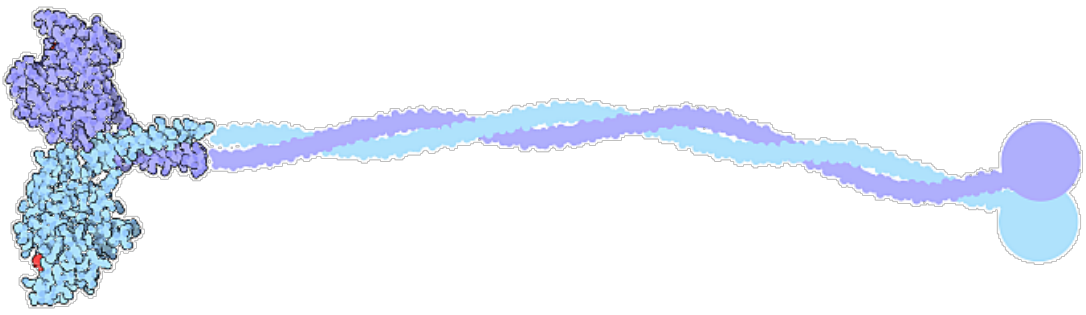

Figure 1.9: Kinesin dimer drawn according to X-ray crystal structures. The heads (left) constitute the motor domain: they bind to a microtubule and perform a synchronized walking-like motion, switching between the leading and the trailing position. The heads are connected via a linker to the stalk. At the end of the stalk cargo can be attached. Image by David S. Goodsell, RCSB PDB [122].

steps of 8 nm [120], which corresponds to two tubulin units. Dimeric kinesin exhibits high processivity and velocity: numerous *in vitro* experiments revealed continuous runs over distances of several micrometers at over 800 nm/s [120, 124–127]. According to optical trapping studies, single kinesin molecules can perform mechanical work against a significant extraneous force of up to 5-7 pN [124–126, 128, 129]. Such values are consistent with the few available studies of behaviour of kinesin working against a viscous load [130, 131]. However, these results refer only to motion of relatively large cargo pulled by kinesin in solutions of polymers of high molecular weight. Should we simplistically consider the Stokes' drag as the only important factor determining mobility of kinesin in crowded environment, a cargoless motor (roughly approximated by a sphere of diameter of 6 nm) should retain its processivity even in extremely viscous solutions, up to hundreds of Pa·s.

It is now widely agreed that the kinesin steps are performed in a hand-over-hand fashion [120, 132–136], *i.e.* while one of the heads is bound to the microtubule, the other passes it and moves to the subsequent binding spot. Therefore, the leading and trailing heads switch places during every step – the whole process is sometimes metaphorically depicted as resembling human walk. The fine mechanochemical synchronization of subsequent stages of the step is crucial for the protein's processivity. Even though the kinesin class has been intensively studied since the early 1990s, the molecular mechanics of the kinesin step is still debated [120]. Since the motor domain reveals much similarity to the actuator of myosin, the primary mammalian muscle protein, some investigators suggest a similar force generation mechanism, based on so-called power strokes [137–140]. However, the kinesin dimer does not possess a stiff, rod-like lever to transduce the generated force. An alternative hypothesis to the power stroke is that the mechanochemical cycle of kinesin is responsible for the directionality of the movement, but translocation of the head is mostly due to diffusion [125, 126, 141]. It was even suggested that the reason for the enzyme's directionality is asymmetry of barriers for forward and backward diffusive movement [125]. It should be noted

that the two mechanisms, power stroke and head diffusion, are not necessarily mutually exclusive [119,120]. Elucidation of the exact working principle and stepping mechanism of this model and ubiquitous molecular motor still remains an open challenge.

Chapter 2

Experimental Techniques

The thesis comprises results obtained by means of several different experimental techniques, often featuring some novel approach or modifications. Therefore, it is essential for correct interpretation of the data to first provide an insight into the working principles and background of these techniques. Within this chapter, an introduction to fluorescence correlation spectroscopy (Section 2.1), total internal reflection fluorescence microscopy (Section 2.2), rheometry (Section 2.3), dynamic light scattering (Section 2.4), and microelectromechanical oscillator techniques (Section 2.5) can be found.

2.1 Fluorescence Correlation Spectroscopy (FCS)

Fluorescence correlation spectroscopy is a non-invasive, optical technique allowing for determination of diffusion coefficients of fluorescent probes. It relies on observation of a focal spot wherein only single probes are present at a given moment. Due to Brownian motion, the probes move in and out of the observed volume, causing fluorescence fluctuations. Time correlation patterns can be found in the signal fluctuations, which correspond to the mean time of residence of the probe in the observed volume. Provided proper instrument calibration, these data allow for calculation of the probe diffusion coefficient. In the following paragraphs, a broader introduction to the technique is given.

The Phenomenon of Fluorescence

Fluorescence is defined as a type of luminescence – spontaneous emission of electromagnetic radiation from an excited species – which occurs essentially only during irradiation of the species [17]. The emitted radiation differs in wavelength from the beam used to excite the fluorescent species. First reports of such phenomenon come from the XVI century and concern infusion of the so-called kidney wood; later on, the natural fluorescent compound observed in this case was identified as matlaline [142]. The term fluorescence was coined by Stokes [143], who was the first one to analyse it systematically and observe that visible fluorescence can be obtained by irradiation with UV light (hence the term *Stokes shift*, introduced later on to denote the difference in wavelength between the excitation and emission radiation).

The physical principle of fluorescence is a sequence of excitation and relaxation processes [18]. When a molecule (or nanostructure) interacts with a photon whose energy corresponds to the difference between the ground and excited states of the molecule, it may absorb the photon. However, this excited state is out of the thermodynamic equilibrium. Therefore, the molecule tends to return to the

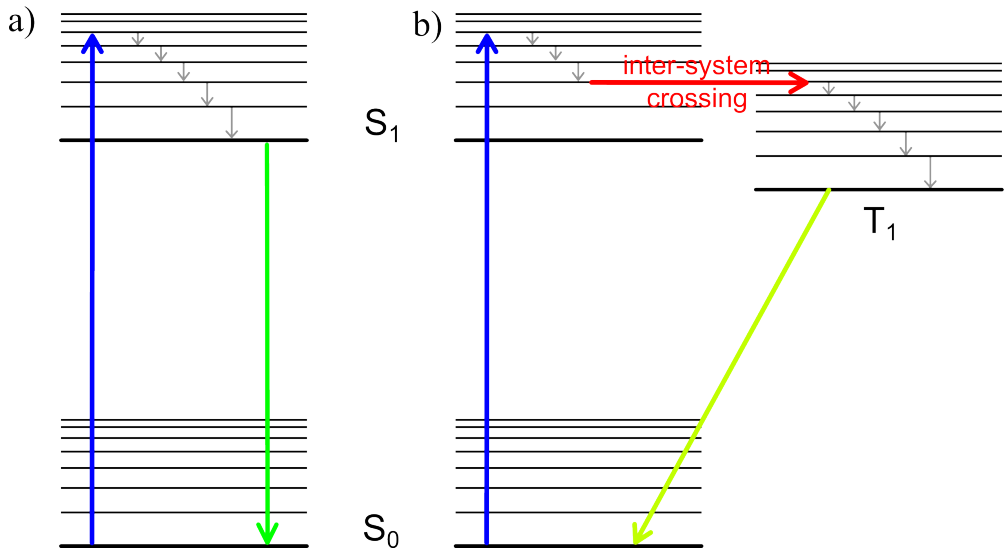

Figure 2.1: Exemplary Jablonski diagram for a) fluorescence; b) phosphorescence. S_0 and S_1 correspond to ground and first excited singlet electronic states; T_1 is the triplet state. Thin horizontal lines correspond to vibrational excited states.

equilibrium ground state. In most cases, relaxation happens in a non-radiative manner – energy is dissipated to the surroundings and heat is produced. However, in case of some species a radiative relaxation may occur, where the extra portion of energy is emitted as a photon – which is observed as fluorescence. The probability of radiative relaxation depends on the electronic structure of the molecule and spaces between its energy levels, as well as the environment (*e.g.* solvent). This probability is expressed as quantum yield, which is defined as a ratio of number of photons absorbed by the molecule to the number of emitted photons [144].

Photon emission does not happen instantaneously; in case of fluorescence, it usually takes few nanoseconds. During this time, some energy of the excited molecule is dissipated, which is the reason why the Stokes shift is observed. The transitions occurring during the fluorescence process are schematically presented in a Jablonski diagram in Figure 2.1a.

If there exists a vibrational state of the excited molecule whose geometry is identical to the geometry of the molecule in a triplet state, inter-system crossing may occur. Relaxation to the ground singlet state requires both a change of the

relative position of nuclei as well as change of the system's multiplicity (which is a forbidden transition; it occurs only due to spin-orbit coupling). Therefore, the probability of such transition is relatively low, and so the lifetime of a triplet excited state – *i.e.* phosphorescence lifetime – is much longer than in case of fluorescence: usually, a particle is trapped in a triplet state for a time of the order of microseconds, although some cases are known where phosphorescence lasts for minutes or even hours.

Currently, there is a broad range of synthetic fluorescent compounds available. An effective dye for application in imaging and fluorescence correlation spectroscopy needs to satisfy several basic conditions:

1. High stability, low photobleaching;
2. Low probability of inter-system crossing (no significant blinking);
3. Solubility in water (for use with biological samples);
4. High quantum yield;
5. Absorption/emission spectrum suited to the experimental setup (available light sources and filters).

Experimental Realization of FCS

Although FCS is a microscopy-based technique, it does not rely on imaging, but focuses on a single, (usually) immobile spot. Since the information on diffusion of fluorophores is retrieved from the fluctuations of fluorescence intensity at the observed spot, the magnitude of these fluctuations needs to be as high as possible. Ultimately, at a given time point the amount of probes in the detection volume should be of the order of unity – then, a single molecule entering or leaving this volume causes a significant relative change in the observed fluorescence intensity. This requires advanced optics to allow for minimization of the observed volume and detectors of high sensitivity to capture the fluorescence of single molecules.

The answer to these requirements is confocal microscopy coupled with a single-photon counting systems [145]. A schematic representation of a typical FCS setup is presented in Figure 2.2. A laser beam is directed via a dichroic mirror to a microscope objective. The objective is one of crucial components of the system, since it determines the shape of the light beam inside the sample and therefore influences the observation volume. Low aberrations and high numerical aperture (NA) are required. The latter parameter determines the fraction of photons emitted from the illuminated volume that are collected by the objective. Numerical aperture is defined as

$$\mathrm{NA} = n \sin \theta_{\mathrm{lens}}, \tag{2.1}$$

where n is the refraction index of the medium in which the lens is immersed, while θ_{lens} is the half-angle of the light cone reaching the lens. To achieve proper geom-

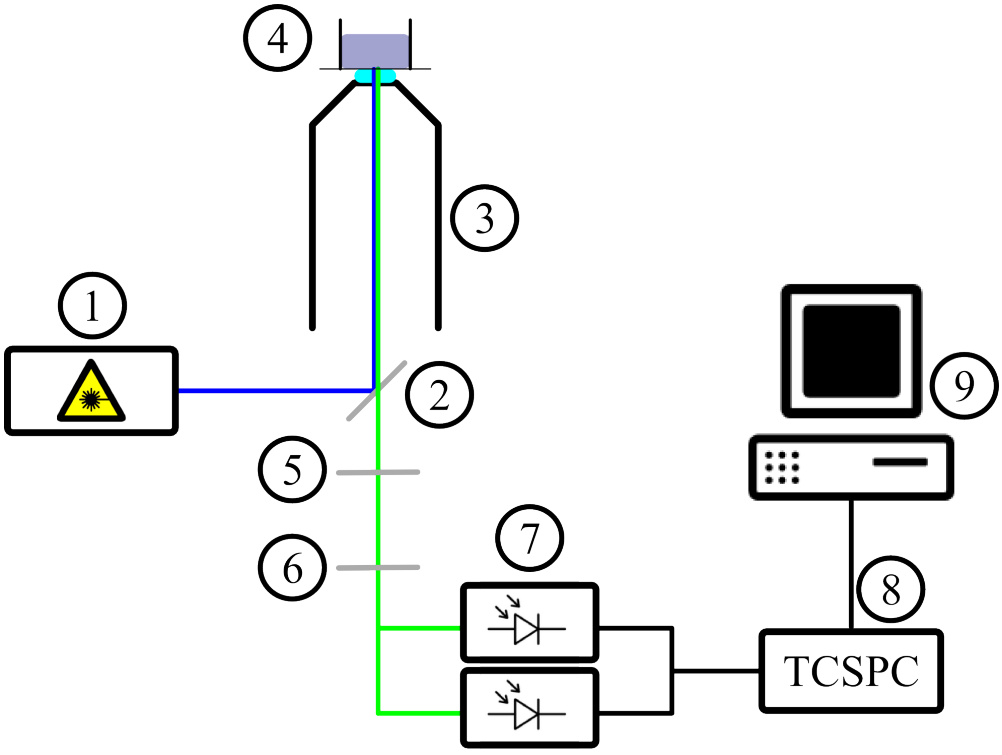

Figure 2.2: A standard FCS setup. **1** – laser, **2** – dichroic mirror, **3** – objective, **4** – sample, **5** – pinhole, **6** – wavelength filter, **7** – detectors (preferably two, working in parallel), **8** – time-correlated single-photon counting module, **9** – data analysis workstation.

etry of the focal spot and good efficiency of photon collecting, usually objectives of NA >1 are used. This implicates use of immersion objectives, where between the lens and sample a droplet of water (n=1.33) or oil (n>1.4) is placed.

Fluorescence collected by the objective is focused and passed through the pinhole, which is an essential feature of a confocal microscopes. Pinhole was originally introduced in scanning microscopes to improve the resolution along the z axis (*i.e.* in the direction of the beam propagation in the sample). It is a narrow aperture which rejects all the out-of-focus fluorescence. This allows to minimize the detection volume to $2 \cdot 10^{-16}$ l (0.2 fl) or even less. A special case where pinhole is not necessary in an FCS system is a two-photon excitation setup, where the small dimensions of the observed volume are due to low volume of effective illumination (there is a square dependence of probability of absorption event on the light intensity, instead of linear as in case of single-photon illumination) [146].

Next, the beam goes through a set of wavelength filters. They are matched so that they would allow the fluorescence band through, blocking the background light of other wavelengths. Most importantly, the filters cut away the excitation beam: laser intensity is higher than fluorescence intensity by orders of magnitude, therefore even a fraction of the beam that is backscattered in the sample or reflected from the cover-glass would cover up the fluorescence signal and could even damage the detectors.

The detectors need to present high sensitivity (high quantum efficiency of the detector) and good time resolution. Two main technologies are currently used: single-photon avalanche diode (SPAD) and photomultiplier tube (PMT). Recently, a new generation of hybrid detectors was introduced, which combines the advantages of both technologies. The detectors are coupled with a time-correlated single-photon counting device, which allows to pin a time tag to every photon detection event and produce digital data that are correlated and analysed using dedicated software.

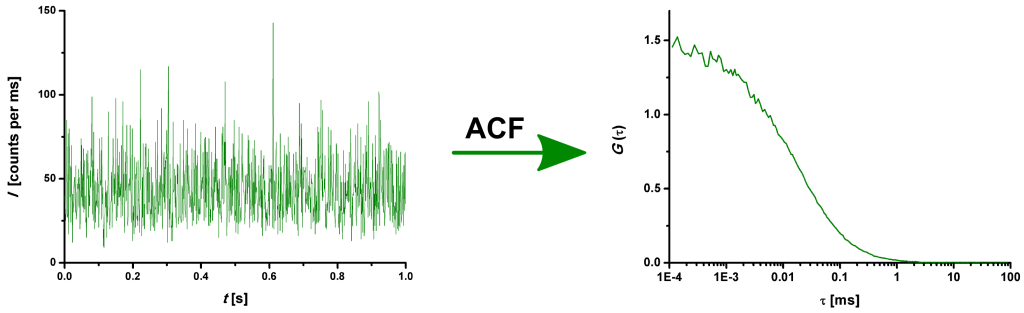

Figure 2.3: The raw data in FCS are fluorescence intensity I values given as a function of real experiment time t. The autocorrelation function transforms these data into a plot of magnitude of correlation versus lag time τ. From the $G(\tau)$ plot, via fitting of an appropriate physical diffusion model characteristic diffusion time of the probe can be inferred.

Theory of FCS

Fluorescence correlation technique is based on analysis of fluctuations – the foundation of its theory lies in the physics of noise (see *e.g.* [147, 148]). First implementation of this theory to monitoring of chemical dynamics via observation of fluorescence fluctuations is credited to Magde, Elson and Webb [149, 150].[1]

The pivot point of data analysis in FCS is the autocorrelation function (ACF, here denoted as $G(\tau)$). Its principle is to find fluctuation patterns in the raw fluorescence signal and measure the time scales of these patterns – *i.e.* pinpoint the temporal correlations. The fluorescence intensity at time t is compared to intensity at time $t + \tau$ and correlation at a lag time τ is quantitatively assessed across the whole data set. Therefore, data recorded in the real time domain are transformed to the lag time domain, as illustrated in Figure 2.3). In a simplest form, the ACF can be written as [145]:

$$G(\tau) = \frac{\langle \delta I(t) \delta I(t+\tau) \rangle}{\langle I(t) \rangle^2} \ . \tag{2.2}$$

[1] Although these landmark articles come from early 1970s, FCS was not broadly applied until late 1990s when instrumentation started to keep up with the theory and confocal microscopes as well as ultrasensitive detectors became commercially available

where $\delta I(t)$ is the variance of fluorescence intensity at time t:

$$\delta I(t) = I(t) - \langle I(t) \rangle \tag{2.3}$$

Therefore, the value of ACF is in fact a measure of autocovariance of fluorescence intensity. The denominator in Equation 2.2 is a normalization factor. Due to large temporal range of phenomena observed in FCS, $G(\tau)$ is usually drawn against a logarithmic scale.

$G(\tau)$ carries information on the time scale of residence of a fluorophore in the detection volume. However, a key to elucidation of this information is proper description of the geometry of the detection volume. Usually, a three-dimensional Gaussian profile is used to approximate the detection profile [145]:

$$I(\mathbf{r}) = I_0 \exp\left(\frac{-2(x^2+y^2)}{w_0^2} - \frac{2z^2}{z_0^2}\right). \tag{2.4}$$

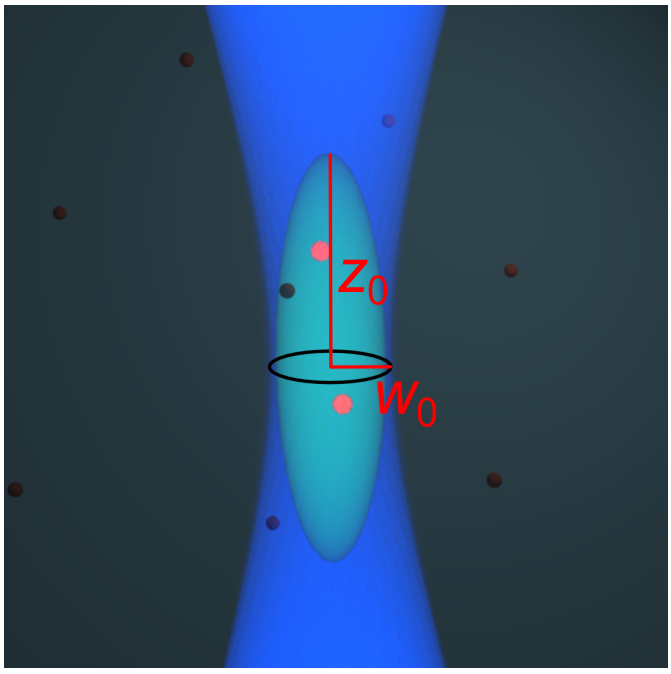

Figure 2.4: The detection volume in FCS is an elongated ellipsoid with a 3D Gaussian distribution of probability of detecting a molecule at a given point. It is located in the waist of the focused illumination beam and has axial symmetry. w_0 and z_0 are the short and long radii of the ellipsoid. The dimensions correspond to the $1/e^2$ surface of the Gaussian distribution.

I is a measure of signal intensity, w_0 is the beam waist along the x and y axis (the detection volume has axial symmetry) and z_0 is the dimension of the Gaussian profile in the direction of light propagation. The boarders of the detection limit are not sharp: the waist corresponds to a distance from the spheroid centre where the probability of detecting a molecule decreases to a fraction of $1/e^2$ of the maximum value. A volume of such spheroid, V_{det}, can be calculated as

$$V_{\mathrm{det}} = \pi^{3/2} w_0^2 z_0. \tag{2.5}$$

The ideal detection volume is depicted in Figure 2.4. On the basis of a Fourier transform of the detection profile and basic diffusion equations a relation can be established between $G(\tau)$, shape of the detection volume and average time of residence of the fluorophore in this volume, τ_D [145, 151]:

$$G(\tau) = G(0) \left(1 + \frac{\tau}{\tau_D}\right)^{-1} \left(1 + \frac{\tau}{\kappa^2 \tau_D}\right)^{-1/2}. \tag{2.6}$$

κ is a measure of elongation of the detection volume, called the structure parameter and defined as

$$\kappa = \frac{z_0}{w_0}. \tag{2.7}$$

$G(0)$ in Equation 2.6 is the amplitude of the ACF at $\tau = 0$. It can be shown that due to Poissonian distribution of fluorophores in the sample [145],

$$G(0) = \frac{1}{N}, \tag{2.8}$$

where N denotes the average number of probes in the detection volume. Therefore, from the amplitude of the autocorrelation function the probe concentration can be inferred. Since a mean distance covered by a spontaneously diffusing molecule in time τ is proportional to $\sqrt{D\tau}$, it can be shown [145] that, within the approximation of a Gaussian detection profile, the diffusion time extracted from Equation 2.6 is

$$\tau_D = \frac{w_0^2}{4D}. \tag{2.9}$$

Thus, if the beam waist is known (from calibration experiments), diffusion coefficient of the probe can be easily calculated on the basis of an FCS measurement.

A common issue is a sharp burst of the ACF amplitude at short time-scales due to a specific detector noise, known as afterpulsing [152]. This artefact is observed both in avalanche photodiodes and photomultiplier tubes. It is related to random generation of spurious signals short after the detection of photon, and therefore is highly correlated. The most effective way of its elimination is using a beam splitter before the detector unit and two independent detectors (as on the scheme in Figure 2.2). Then, a cross-correlation is performed instead of autocorrelation and Equation 2.2 is modified to

$$G(\tau) = \frac{\langle \delta I_1(t) \delta I_2(t+\tau) \rangle}{\langle I_1(t) \rangle \cdot \langle I_2(t) \rangle} \,, \tag{2.10}$$

where indices 1 and 2 refer to signal recorded by the two detectors. Afterpulses on the two detectors appear independently, but fluctuations of the actual fluorescence signal reaching both of them are the same. Therefore, such treatment effectively removes the afterpulsing issue, leaving the diffusion information intact and improving the signal to noise ratio.

Another issue are changes of brightness of the probes residing in the observation volume. If the fluorophore bleaches, it is not detected any more even though the particle has not physically moved. To avoid this kind of errors, stable fluorophores and no excessive laser power should be used. However, most dyes may enter a triplet state, which has a lifetime of the order of microseconds. During this time, the molecule is dark. Entering the triplet state is manifested as blinking of the fluorophore and influences the shape of the autocorrelation function. To account for that, an additional factor should be added to Equation 2.6, producing a formula [151]:

$$G(\tau) = G(0) \left(1 + \frac{p}{1-p} \exp\left(\frac{-\tau}{\tau_\mathrm{t}}\right)\right) \left(1 + \frac{\tau}{\tau_D}\right)^{-1} \left(1 + \frac{\tau}{\kappa^2 \tau_D}\right)^{-1/2} , \tag{2.11}$$

where p is the average fraction of fluorophores being in a triplet state and τ_t is the lifetime of this state.

If there is more than one population of fluorescent probes of a distinct diffusion coefficient, it should be included in Equation 2.6 by applying a summation:

$$G(\tau) = \sum_i G_i(0) \left(1 + \frac{\tau}{\tau_i}\right)^{-1} \left(1 + \frac{\tau}{\tau_i \kappa^2}\right)^{-1/2}, \tag{2.12}$$

where the i index refers to the i-th population of probes. However, it should be noted that the more complex the model fitted to the ACF, the less reliable the estimated values of its parameters. Therefore, if there is more than one population of the fluorophores in the sample, it is advisable to perform additional measurements on isolated probes of given kinds to fix some of the parameters in Equation 2.12.

2.2 Total Internal Reflection Fluorescence (TIRF) Microscopy

Confocal microscopy allows to limit the thickness of the observed plane of focus to a few micrometers (depending on the wavelength and optical setup). However, such resolution along the z axis is not sufficient for some studies. Using total internal reflection fluorescence (TIRF) microscopy, it is possible to observe a slice of sample of thickness of less than 100 nm [153]. The main limitation of TIRF is that, unlike in case of confocal microscopy, the choice of the focus plane is arbitrary: only the immediate neighbourhood of the cover-glass can be observed. It is due to the physical principle of TIRF, briefly described below.

The technique is based on the phenomenon of total internal reflection. According to Snell's law, when a light beam is incident at a phase boundary at an angle θ_1, its angle of refraction θ_2 is such that

$$\frac{\sin\theta_1}{\sin\theta_2} = \frac{n_2}{n_1}, \tag{2.13}$$

where n_1 and n_2 refer to the indices of refraction of the two phases. If $n_1 > n_2$ and θ_1 is large enough, the above relation seems to require $\sin\theta_2 > 1$, which is of

course not possible. In such case, the beam cannot pass the phase boundary, but gets totally reflected. The minimum value of θ_1 for such effect to occur in a given system is denoted as the critical angle.

However, due to the wave nature of light, in case of total reflection an evanescent electromagnetic wave appears on the other side of the interface. The evanescent wave is exponentially attenuated in the z direction, providing an effective illumination of a layer of less than 100 nm of the specimen. If there are fluorophores (of absorption spectrum matching the wavelength of the light used) within this layer, they are excited and the fluorescence can be observed. A schematic visualization is presented in Figure 2.5.

TIRF microscopy is extremely useful in biology, *e.g.* in observation of membrane processes in adherent cells. Modern techniques of surface decoration and passivation allow for tailoring the TIRF experiments to observe selected processes occurring in two dimensions with extremely low background signal.

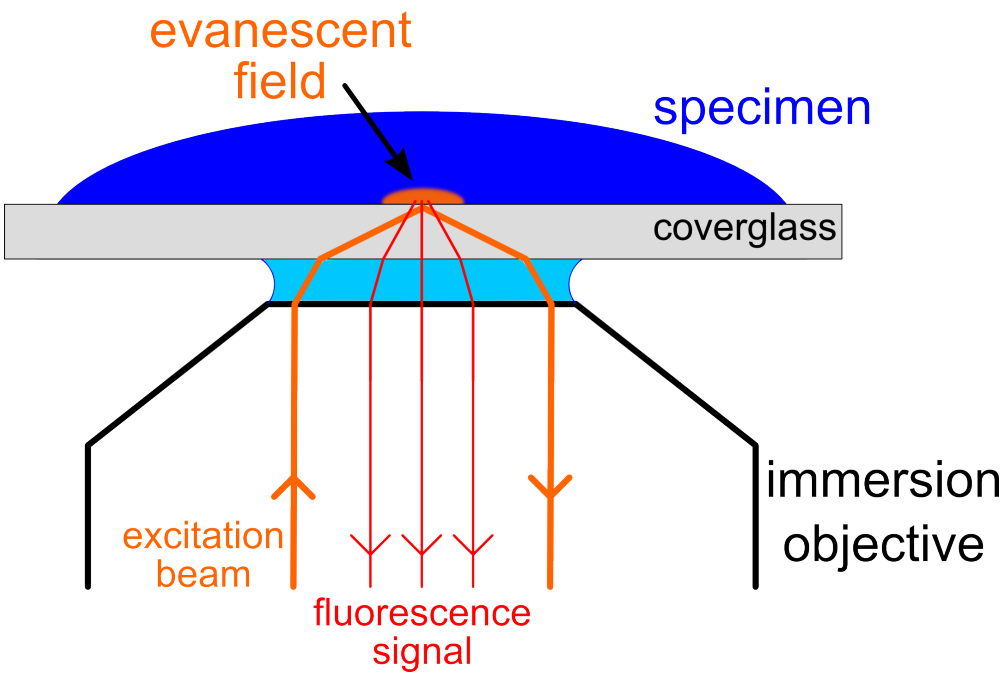

Figure 2.5: Schematic representation of an exemplary realization of a TIRF microscopy experiment.

2.3 Rheometry

The simplest way of measuring macroscopic, dynamic viscosity of liquids is viscometry. Two basic types of viscometers are distinguished: U-tube (Ostwald) and falling ball. In the first kind, time of gravitational flow of a given amount of liquid through a capillary is measured. In the falling ball viscometer, a narrow vertical pipe is filled with the investigated liquid and a ball of diameter slightly lower that the pipe and density higher than the liquid is dropped into the pipe. From the parameters of the ball and time of flight through a stretch of a given length the liquid viscosity is inferred (the ball experiences hydrodynamic friction – see Equation 1.21). Although both methods have been developed to provide high accuracy, proper temperature control and automation of the measurement process, they are only useful in case of ideal viscous flow.

In complex liquids, such as polymer solutions, elastic properties are frequently observed. In an intuitive Maxwell model, viscoelastic response of a liquid to an applied force is compared to response of a serial connection of a spring and a dashpot (damper) [154]. Elasticity of polymer solutions is attributed to relatively slow relaxation of the system due to entanglements between the chains. Therefore, it is possible for a liquid to present viscoelastic properties at high shear, while at low shear the rate of relaxation processes is sufficient to allow for Newtonian response of the liquid.

Rheometry comprises a set of techniques developed to study the response of such complex liquid systems. A most popular type of equipment used in such research is a rotational rheometer. The core of modern appliances of this kind is a high-precision servo motor, providing torque to a rotor placed on low-friction bearings. Angular speed of the rotor is precisely measured by a position encoder to provide results as well as feedback control of the motor. The momentary torque is inferred from the current supplied to the motor. At the end of the rotor pivot, the measurement geometry is mounted where the sample is put (see Figure 2.6).

The response of the sample to the shear applied via the rotor is assessed by the resistance of the sample (both rotational velocity of the rotor and torque are constantly monitored).

Depending on the properties of the sample, different measurement geometries may be used. Perhaps the most popular and universal assembly is the cone-plate system, as presented in Figure 2.6. Different cone angles and diameters are available. However, for low viscosity specimens often the so-called *cup and bob* geometries are used, such as coaxial cylinder or double gap cylinder. Such systems require a greater sample volume and are usually characterized by higher inertia, but offer high surface of friction.

Modern rheometers allow for rotational and oscillatory measurements, as well

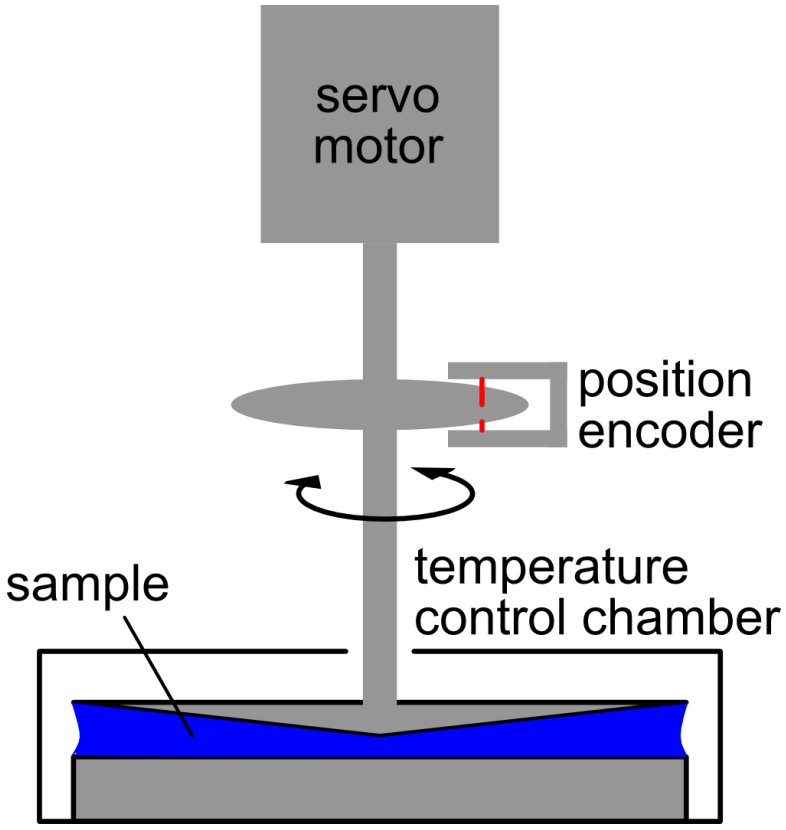

Figure 2.6: The core of a rotational rheometer is a measurement system (here, the most popular cone-plate geometry is depicted), coupled with a servo motor providing torque and position encoder providing readout of position and angular speed of the rotor.

as application of step functions to the system. Both shear stress and shear rate can be controlled [154]. Different parameters of liquids, such as yield stress, tixotropy, viscoelastic modulus, or creep and recovery can be evaluated. However, from the point of view of this Thesis, most important are precise measurements of shear viscosity. A rotational rheometer allows to perform experiments at a broad range of shear to find the region where the response of the sample is Newtonian. Then, this range is used for precise evaluation of viscosity which can be extrapolated to zero-shear conditions (which is a standard for data analysis and presentation).

2.4 Dynamic Light Scattering (DLS)

Dynamic light scattering (DLS), also known as photon correlation spectroscopy or quasi-elastic light scattering [36], is a technique developed to measure diffusion coefficients of macromolecules and colloidal particles (of sizes below *ca.* 100 nm). It is similar to FCS from the mathematical perspective, since it also relies on the autocorrelation function. It is based on light scattering, so, unlike FCS, it does not require fluorescent labelling of the probes. This however may also be viewed as a disadvantage, as it does not allow for easy observation of a given population of labelled probes in a matrix composed of macromolecules (*e.g.* protein in a polymer solution).

When light interacts with matter, it can be either absorbed or scattered. During elastic scattering, the wavelength does not change. However, if a beam is scattered from a moving particle, an effect similar to the Doppler effect is observed: the wavelength is slightly shifted. If a colloidal dispersion is illuminated with a light beam, scattering occurs on multiple, randomly diffusing (due to Brownian motion) objects. Therefore, the scattered rays vary in frequency which causes both constructive and destructive interference – hence, fluctuations of the intensity of the scattered light appear [56].

A scheme of a typical DLS setup is presented in Figure 2.7. Usually, a contin-

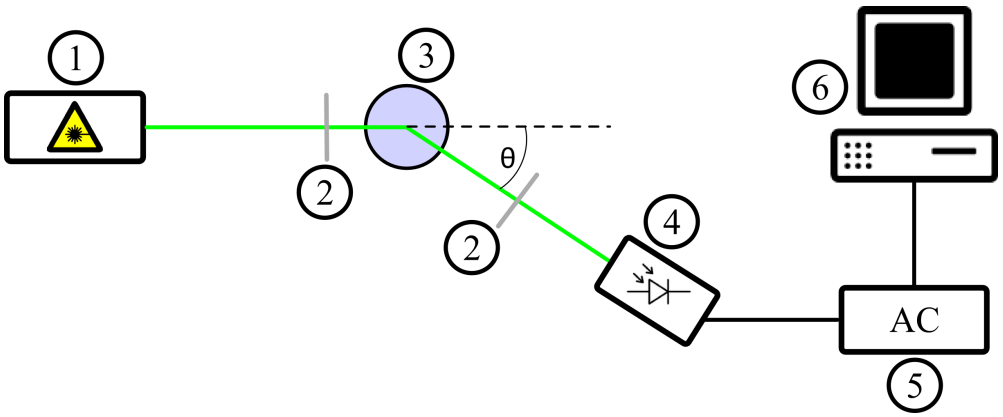

Figure 2.7: Simplified scheme of a typical DLS setup. **1** – laser; **2** – lens; **3** – sample (in a round cuvette); **4** – detector (photomultiplier); **5** – autocorrelator; **6** – workstation for data analysis. θ is the scattering angle, which can be adjusted by means of a goniometer. In principle, the incident beam can be scattered isotropically and θ is an experimental parameter, and not a sample property. In the scheme, scattered light is drawn as a well-defined beam going towards the detector only for the sake of clear demonstration of the principle of the DLS measurement.

uous wave laser beam is used to illuminate a sample contained in a cuvette. By means of a goniometer, a photon detector is placed at a certain θ angle respective to the primary laser beam, so that it would collect light scattered at this angle. The idea behind the analysis of the fluctuations in the scattering intensity is the autocorrelation function [56]:

$$G(\tau) = \langle I(t)I(t+\tau)\rangle\,. \tag{2.14}$$

The above notation is analogous to the (not normalized) ACF equation used in FCS (Equation 2.2). $I(t)$ is here the scattering intensity at a given time t. In a standard data analysis procedure, the autocorrelation function is calculated, normalized and plotted against τ. In the simple cumulant method, applicable to monodisperse samples, a third degree polynomial is fitted to the logarithm of the correlation function to yield τ_{D}. Polydisperse/multimodal samples require a more sophisticated approach, *e.g.* based on the CONTIN algorithm [155]. τ_{D} is interpreted here as a mean diffusion time over the distance proportional to the inverse of the length of the wave vector $\mathbf{q}$, which is determined by the experimental

setup. The modulus of $\mathbf{q}$ is given as

$$|\mathbf{q}| = \frac{4\pi n \sin(\theta/2)}{\lambda}, \tag{2.15}$$

where λ denotes wavelength of the scattered beam and n is the refraction index of the solution. If the scattering object performs a random walk, its diffusion coefficient can be calculated as

$$D = \frac{1}{|\mathbf{q}|^2 \tau_{\mathrm{D}}}. \tag{2.16}$$

Therefore, from a single DLS measurement the diffusion coefficient of a scatterer can be inferred. If the diffusion particle is significantly smaller than the wavelength of the scattered beam, the obtained result does not depend on the θ angle. The technique is frequently utilized to measure hydrodynamic radii of (macro)molecules – from the diffusion coefficient measured in a dilute solution, R_{h} can be inferred via the Stokes-Sutherland-Einstein relation (Equation 1.22). It is also important to notice that in case of DLS measurements performed on semi-dilute polymer solutions, a signal from a „scattering unit" is recorded, which does not necessarily correspond to a single polymer chain [16].

2.5 Quartz Tuning Fork (QTF) Microoscillators

Quartz tuning fork (QTF) is a mass-produced vibrating piezoelectric device, often used as a frequency reference in digital real time clocks. It is manufactured with hermetic vacuum housing, which may be removed to expose the piezoelectric element, depicted in Figure 2.8. When excited using an electric signal at resonance frequency, QTF vibrates in flexural mode in which its prongs move perpendicular to their side surfaces. It can serve as both an actuator and a detector, offering very good stability of resonance frequency, small dimensions and low price. Therefore, numerous scientific applications of such devices have recently been developed, including specific biosensors [156], humidity sensors [157], or even atomic force

microscopy actuators [158]. Particular attention is given to the application of QTFs in measurements of density and viscosity of liquids [159–162]. Such sensors can be very accurate, as damping of the vibrations of a QTF immersed in a fluid strongly depends on the viscosity of the medium [161–163].

The principle of QTF is similar to quartz crystal microbalance (QCM), which also has been used as a viscosity sensor [30,164,165]. The main difference between these two appliances is that the QCM vibrations occur along the direction parallel to its surface. Therefore, only shear parallel to the surface can be observed, while the QTF is a 3D object immersed in the liquid and most friction is due to movement of the surface normal to the oscillation direction. Physically different phenomena may therefore be observed in these two cases.

The piezoelectric element of the QTF is excited with alternating current, at frequency corresponding to its mechanical resonance. A shift in the resonance frequency corresponds to a change in the mass of the oscillator and/or the density of its environment (which effectively also means a change of total mass displaced during oscillations). Viscosity measurements are based on the rate of decay of

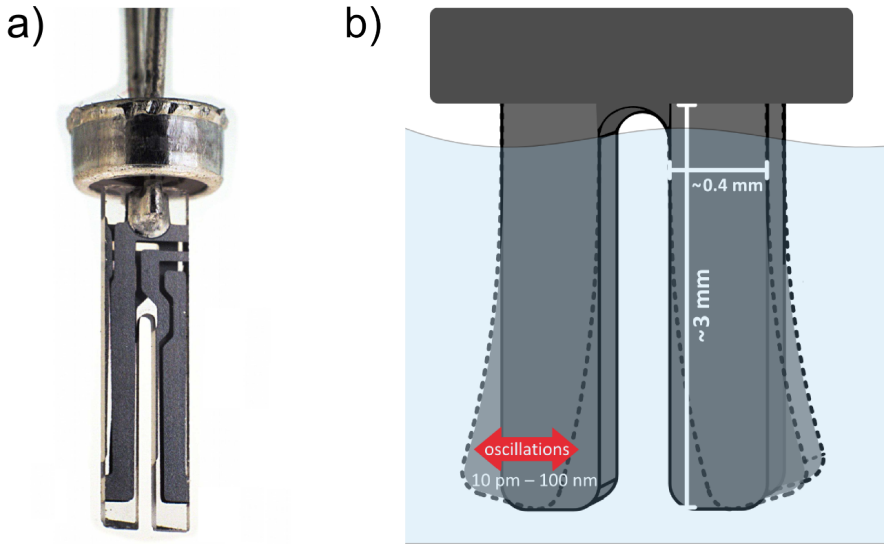

Figure 2.8: Quartz tuning fork oscillator used for viscosity measurements. a) Real-life image; b) Scheme depicting the sizes and main oscillation mode of the QTF (displacement magnitude drawn not to scale).

oscillations. When the excitation current is switched off, the QTF behaves as a dampened oscillator whose amplitude decreases exponentially. The current generated due to the piezoelectric effect can be measured, which allows to analyse the rate of decrease of the amplitude of oscillations.

The time constant t_c of the exponential decay of the oscillation amplitude depends on the damping coefficient of the QTF and viscosity of its environment η. Both modelling [166] and previous measurements [162] imply that $t_c \propto \eta^{-1/2}$. Therefore, η of the investigated liquid can be evaluated by comparison of the decay time constants of the QTF measured in the sample t_c and in a reference liquid of known viscosity $t_{c_{ref}}$:

$$\eta = \eta_{ref} \left(\frac{t_{c_{ref}}}{t_c} \right)^2 . \tag{2.17}$$

Importantly, the excitation voltage can be controlled to fine-tune the initial oscillation amplitude in a subnano- to submicrometer range. This allows to use the QTF (which is a mm-sized device) to probe the response of a liquid to displacements at extremely short length-scales.

Chapter 3

Materials and Methods

This chapter compiles all crucial information on the chemicals, procedures and equipment used throughout the presented research projects. In Section 3.1, the FCS setup is presented, along with the data acquisition and analysis procedures, as well as characterization of fluorescent probes. Sections 3.3 and 3.4 cover rheometry and DLS equipment, respectively. Next, the novel system for measurements of liquid viscosity by means of a quartz tuning fork (Section 3.5) and kinesin stepping assays (Section 3.2) are described. Section 3.6 provides size characterization of the polymers used in all the experiments.

3.1 FCS Experiments

All the fluorescence correlation spectroscopy experiments described within this thesis were performed on dedicated FCS systems, based on a Nikon A1 and Nikon C1 inverted confocal microscopes (Nikon Instruments, Tokyo/Yokohama, Japan). Both setups comprised complete time-correlated single photon counting systems from PicoQuant GmbH (Berlin, Germany) and water immersion objectives Nikon PlanApo 60x, NA=1.20 with a ring for cover-glass thickness correction. A configuration with two independent detectors working in parallel was always used to allow for cross-correlation and elimination of the afterpulsing effect. The detectors used were single-photon avalanche photodiodes by Micro Photon Devices (Milan, Italy) and PerkinElmer Optoelectronics (Dumberry, Canada). The reminder of the setups comprised a dual-channel SPAD power supply DNS 102, TCSPC module PicoHarp 300 and PHR 800 router, all by PicoQuant. A 543 nm He-Ne laser (Melles Griot, Carlsbad, USA) and 488 nm diode laser (PicoQuant) working in constant wave mode were used as excitation beam sources, depending on the spectrum of the dye used. Long-pass and band-pass filters by Chroma (Olching, Germany) and Semrock (Rochester, USA) were applied to separate the fluorescence signal. Lab-Tek 8-well chambers were used as sample containers except for the temperature dependence measurements, where a custom-made chamber was used.

Home-Made Temperature Control System

Although microscope objectives are generally prepared for operation in different temperature conditions, significant changes of temperature influence the optics in a way that disqualifies accurate FCS measurements due to changes of size and shape of the confocal volume. The problem becomes particularly pronounced when temperature dependencies of processes occurring in the sample are to be studied. On the other hand, use of immersion objectives is strongly recommended

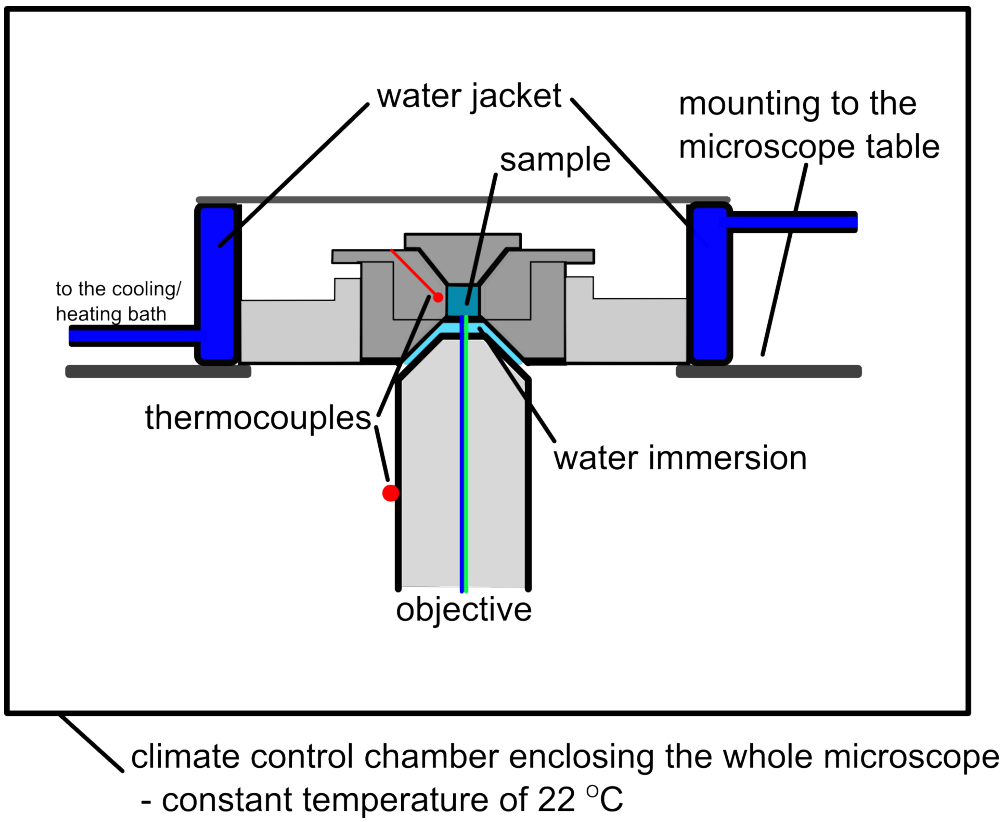

Figure 3.1: Scheme of the temperature control system used for FCS measurements.

because of the high NA requirement. This results in a significant heat flux between the sample and the objective. To solve this issue, we constructed a two-stage system, utilizing an Okolab H201 cage incubator (Okolab S.R.L., Ottaviano, Italy), enclosing the whole microscope, and a top stage incubator, based on Okolab H101-CRYO. The temperature of the cage incubator was kept constant. The main part of the system was a self-designed, solid aluminium sample container, inspired by work of Muller and Richtering [167]. Its scheme is presented in Figure 3.1. The dimensions of the sample container were set to fit with the steel Okolab H101 water chamber, which enabled efficient heating/cooling of the container via a water jacket coupled with a Lauda RP200 thermostat. At the bottom of the sample container a replaceable glass cover slip was placed. The bottom part of the sample container (below the cover slip) was shaped to fit the top of the objective, leaving some space for the immersion. Due to such construction, the whole body

of the objective did not need to be cooled/heated. The temperature gradient in the sample and immersion liquid was minimized, as it was shifted towards the length of the objective. Sample temperature was measured by means of a thermocouple installed in an oblique fissure in the container, so that its tip was located right next to the measurement spot. Tests against another thermocouple placed inside the sample (at its bottom) revealed no discrepancies after *ca.* 10 minutes of equilibration at a given temperature. The temperature and air flow in the large microscope enclosure was controlled to keep the body of the objective and other parts of the optical path in possibly constant conditions. The temperature of the objective body was constantly monitored by a thermocouple taped to it. It was within the 297±2 K range at all times, while the sample temperature could be set in the range of 278–315 K with accuracy of ±0.1 K. As viscosity of liquids strongly depends on the temperature, such range is enough for detailed studies of this parameter. Further details on the construction of the system and its influence on reduction of FCS measurement errors can be found in the master thesis by the author of this Thesis [168].

Refractive Index Matching

Other important factor influencing the shape of confocal volume (and, consequently, obtained diffusivity results), was the non-standard refractive index n of the samples. There was a certain n mismatch between the immersion liquid suiting the objective we used (water, n measured at 543 nm equal 1.3371) and the investigated polymer solutions (n up to 1.3790). Moreover, there were significant differences in the refractive index between the samples. It has been shown that such discrepancies may have a great impact on the geometry of the detection volume and obtained diffusion coefficients [152]. The observed effects are neither linear nor easy to describe mathematically within a simple model. Detection volume calibration for polymer solutions of different n proved to be very

time-consuming and inaccurate, partially due to lack of reference data. To enable quantitative comparisons between samples differing significantly in n, a method of relative analysis was developed.

Reference curves of refractive index as a function of crowder concentration were produced and glycol solution of same n was matched to each of the investigated solutions. For every FCS experiment a reference measurement was performed with the same fluorescent probe and temperature, but a matching glycol solution instead of the actual sample. All the conditions (laser power, probe concentration, cover slip thickness, correction ring setting, sample alignment *etc.*) were kept identical in such a pair of experiments. Along with the n match between the sample and glycol solutions, it ensured consistency in shape and size of the confocal volume.

Literature data on the viscosity of ethylene glycol as a function of temperature and concentration [169] were used to calculate the diffusion coefficients of probes in monomer solutions, D_{glycol}, in particular experiments. Due to the small size of monomeric glycol particles, the calculation could be done using the Stokes-Sutherland-Einstein relation with fixed, macroscopic viscosity. As the parameters of observed volume were identical in PEG and glycol, D_{sample} could be calculated from a simple relation:

$$\frac{D_{sample}}{D_{glycol}} = \frac{\tau_{glycol}}{\tau_{sample}} \tag{3.1}$$

where τ denotes the time of diffusion through the confocal volume. Therefore, the investigated value of diffusion coefficient of a nanoscopic probe in a complex liquid was obtained solely form the experimental data and data on macroscopic properties of ethylene glycol [169] and water [170].

The data acquisition and analysis method utilizing reference experiments allowed for minimization of errors of measurement of the diffusion coefficients. Since all the experimental parameters (including the refractive index) were the same within a given sample–reference pair, errors stemming from the imperfect shape of the detection volume mostly cancelled out. The procedure could be in fact

treated as a method of simplified calibration, adjusted and independently performed for each sample. It enabled direct, quantitative comparison between FCS data obtained for samples exhibiting pronounced differences in the refractive index. Further details on the refractive index measurements and application of the n matching method can be found in the master thesis by the author of this Thesis [168].

Fluorescent Probes

A range of fluorescent probes differing in size was used in the FCS experiments. They are listed in Table 3.1, along with their hydrodynamic radii R_{h}. The values of R_{h} were established by FCS measurements of diffusion coefficients in pure water/buffer and application of the Stokes-Sutherland-Einstein relation (Equation 1.22). In case of rhodamine dyes, which were used for calibration of the instruments, the diffusion coefficients were taken from the literature [171, 172].

High purity rhodamine dyes as well as proteins were purchased from Sigma-Aldrich. The proteins were labelled on-site with bright and stable dyes: Atto 488 and Atto 550. Labelling kits were obtained from Sigma-Aldrich. The dyes were functionalised with N-hydroxysuccinimide ester groups, which coupled to free, exposed amine groups of the proteins. The reactions were performed according to the protocols suggested by the manufacturer. The labelled proteins were purified by means of size exclusion chromatography (filled columns were a part of the protein labelling kits). The prepared proteins were either stored at 4°C and used

Table 3.1: Probes used in FCS measurements and their hydrodynamic radii, R_{h}.

Probe	R_{h} [nm]
Rhodamine 110	0.52
Rhodamine B	0.57
Chicken egg lysozyme	1.9
Kinesin-1–GFP construct	2.5
Horse spleen apoferritin	6.9

within a few days from labelling or diluted in phosphate buffer and frozen for longer storage. If after thawing a batch of protein partial detachment of the dye was observed (two distinct diffusion coefficient in FCS tests), the protein was purified using centrifuge filters (obtained from Merck Millipore) of appropriate pore size. The dye:protein ratio was adjusted to obtain, on average, 1-2 dye molecules per protein. Therefore, the labelling did not affect the dimensions of the protein significantly. Truncated, dimeric kinesin-1 with GFP attached at the C-terminus [173] was courtesy of prof. Stefan Diez, B-CUBE Dresden.

Whenever proteins were used as probes, experiments were performed in buffer solutions instead of deionised water to prevent protein denaturation. The buffer of choice for lysozyme and apoferritin was phosphate buffer of pH 7.2 (adjusted against an electronic pH-meter with a combined glass electrode, Hanna Instruments HI2221) with NaCl added to keep physiological ionic strength (154 mM). In case of kinesin-1, BRB80 buffer was used containing 0.1% of Tween 20 (Sigma-Aldrich). Salts of analytical purity used for buffer preparation were purchased from POCH S.A. Deionised water of conductivity below 0.1 μS/cm was produced using HLP Smart purifier by Hydrolab (Gdańsk, Poland).

3.2 Kinesin Stepping Assays

The stepping assay used in TIRF microscopy has been extensively described by Korten *et al.* [174]. Briefly, we performed the experiments in flow channels [175], self-built from two glass cover-slips (22x22 mm and 18x18 mm; Corning Inc., Corning, USA), which were cleaned in piranha solution (H_2O_2/H_2SO_2, 3:5; both purchased from Sigma-Aldrich), silanised with 0.05% dichlorodimethylsilane in trichloroethylene (Sigma-Aldrich) and glued into a sandwich-like flow cell using heated pieces of Parafilm M (Pechiney Plastic Packaging, Chicago, USA). The surface of the channels was functionalised in five consecutive steps:

1. The flow cell was filled with a solution of TetraSpeck microspheres (diameter

100 nm; Invitrogen) diluted 200-fold in BRB80;

2. After 2 minutes, the solution was exchanged with a BRB80 solution containing 77.5 μg/ml anti-β-tubulin antibodies (SAP4G5; Sigma-Aldrich);

3. After another 5 minutes, the surface was blocked with a solution with 1% Pluronic F-127 (Sigma-Aldrich) in BRB80;

4. Taxol-stabilized microtubules [174], diluted ninefold to prevent crossing microtubules, were incubated for 5 minutes to bind to the tubulin antibodies;

5. Microtubule solution was finally replaced by the motility solution (BRB80 containing 10 μM taxol, 40 μM glucose, 0.2 mg/ml glucose oxidase, 0.02 mg/ml catalase, 10 mM DTT, 0.1 mg/ml casein, 1 mM Mg-ATP, 0.1% Tween 20; all from Sigma-Aldrich) with an addition of 4 μg/ml rKin430-6HIS-GFP [173] as well as appropriate molecular crowding agents.

Fluorescence imaging was performed using an inverted fluorescence microscope (Zeiss Observer Z1; Zeiss, Jena, Germany) with a 100x oil immersion objective (Zeiss Apochromat, NA=1.46) with an additional 1.33x magnifying optovar. The final pixel size was 117 nm. Microtubules were observed by epifluorescence using a Lumen 200 metal arc lamp (Prior Scientific Instruments Ltd., Fulbourn, UK) with a TRITC filter set. Kinesin-GFP was observed in TIRF mode, using a PhoxX 488 nm laser (Omicron-Laserage, Rodgau-Dudenhofen, Germany) with a GFP filter set by Zeiss. Image acquisition was performed at 100 ms exposure time by an electron-multiplied charge-coupled device camera (iXon Ultra DU-897U; Andor, Belfast, Northern Ireland) in conjunction with a Metamorph imaging system (Universal Imaging Corp., Downingtown, USA). For each sample, at least 5 image stacks were recorded at different locations in the sample, each stack comprising 1500 frames. Stacks were analysed separately using a MATLAB-based software package, FIESTA 1.02 [176]. For each stack (except for samples where

kinesin motion was heavily impaired), at least 200 independent kinesin walks were recorded. Velocities of walks were inferred from kymographs (*i.e.* representations of fluorescence intensity in a 2D space: position along microtubule *vs.* time) and averaged. Temperature was kept at 297±2K at all times; reference experiments (with no viscosity increasing agents present in the kinesin solution) performed directly before each measurement series allowed for temperature drift correction. Only linear movement of individual Kinesin molecules was included, disregarding any stalled proteins or stop-and-go events. Only stuck molecules were detected in experiments where a zero velocity was reported.

3.3 Rheometry Experiments

Macroscopic viscosity measurements were performed using a rotational rheometer Malvern Kinexus Pro (Worcestershire, England). The geometry of the measurement system was adjusted to the rheological properties of the sample. For low viscosity samples (of the order of pure solvent viscosity), a double-cylinder geometry was used, whereas for high viscosity samples a cone-plate system was applied. For every sample, measurements at a broad range of shear rate were first performed to establish a window where the response of the sample was purely Newtonian and the data quality was satisfactory. The resulting range of shear stress applied during viscosity measurements was usually *ca.* 0.01 to 10 Pa. Linear extrapolation of the recorded data was performed to obtain the value of viscosity at zero shear conditions, which is the standard for viscosity results presentation. Due to Newtonian behaviour of the samples, viscosity did not change systematically with the shear stress, so the extrapolation can be viewed as a way of averaging the results obtained at different shear. The sample temperature was controlled by a built-in heating/cooling module, providing accuracy of ±0.1 K. In case of activation energy measurements, the investigated temperature range was 278–323 K. All other experiments were performed at 298 K.

3.4 DLS Experimental Setup

The dynamic light scattering (DLS) measurements were performed using a custom-assembled setup, based on a Stabilite 2017 argon ion laser (514 nm wavelength; Spectra-Physics, Mountain View, USA) and a Brookhaven BI-200SM goniometer (Brookhaven Instruments Corp., Holtsville, USA). Unless stated otherwise in the description of a given experiment, the measurements were performed at 298 K; sample temperature was controlled with a water bath providing accuracy of ±0.1 K. For every sample, data were collected at several angles ranging from 30° to 150°. For each angle (*i.e.* wave vector), autocorrelation of scattered photons was analysed as a function of time. Since multimodal curves are frequently observed for polymer solutions, we applied the robust CONTIN algorithm [155] for data analysis. The apparent diffusion coefficients were calculated as an average of the results obtained at different scattering angles.

3.5 Quartz Tuning Fork Experiments

The studies described within this Thesis concern aqueous solutions of polymers. Even highly purified water is electrically conductive to some extent, which makes typical electric measurements of the QTF vibration curve difficult or even impossible to perform [163]. To overcome this limitation, a novel method for QTF excitation and measurement of vibrations was used [177]. The simplified schematic of the measurement setup employing this technique is shown in Figure 3.2a. The method is based on modulation of the excitation signal in a series of sinusoidal bursts. It allows to minimize the influence of the current resulting from the conductivity of the liquid, represented by Y_P in Figure 3.2a, on the total measured current [177]. During a burst, QTF vibrations are excited. When the excitation voltage is switched off, the vibrations decay and the current generated due to the piezoelectric effect in the QTF is measured using the current-to-voltage

converter. Its output is then amplified, which results in the effective ratio of current-to-voltage conversion of 0.4 V/nA. Signal is processed using an analogue-to-digital converter and analysed using custom-written software. The software controls the measurement and calculates the parameters of the exponential decay of the vibrations caused by the viscosity-dependent damping. To improve the signal-to-noise ratio, hundreds of excitation–decay cycles are recorded during a single experimental run. Exemplary recording of the ringdown current is shown in Fig. 3.2b.

The initial value of the amplitude of the current generated by QTF (A_i) is used to calculate the amplitude of physical vibrations of the QTF during the excitation. It is only possible if the QTF used in the experiments has a known value of the electromechanical coupling coefficient α. For a QTF vibrating at the

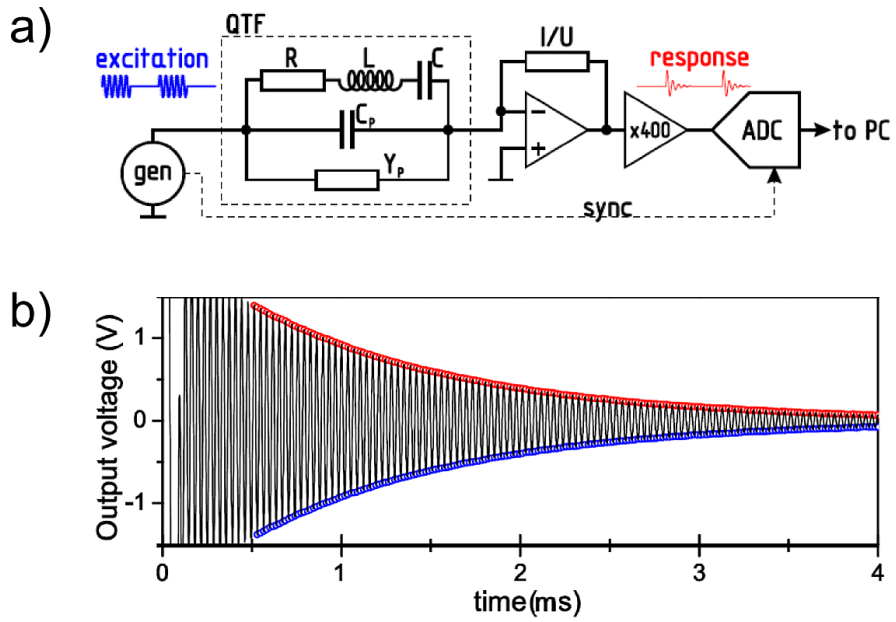

Figure 3.2: a) Block diagram of the device using modulated excitation signal to measure the vibrations of the QTF. Shown are: the excitation signal, the electric equivalent circuit of the QTF in conductive liquid, current-to-voltage converter, amplifier, and analogue-to-digital converter; b) Exemplary registered current generated by a QTF oscillating in water during its ringdown after excitation with 100 mV(RMS) voltage. The parameters of the exponential decay of vibrations are the time constant t_c and the initial amplitude of vibrations A_i.

radial frequency ω,

$$\frac{I}{\omega} = \alpha \cdot x, \tag{3.2}$$

where I is the amplitude of the current generated by the QTF and x is the amplitude of displacement of the QTF prongs [178]. The actual value of α was established in simultaneous electric and optical measurements using a SIOS SP-S 120 laser-interferometric vibrometer (SIOS Messtechnik GmbH, Ilmenau, Germany). The QTFs used in the experiments described herein were characterized by an α value of 16.8 μC/m, while the amplitudes of vibrations ranged from $\sim$ 0.01 to $\sim$ 100 nm.

The setup for QTF measurements was designed, assembled and developed by dr T. Piasecki, dr K. Waszczuk and prof. K. Nitsch from the group of prof. T. Gotszalk at the Faculty of Microsystem Electronics and Photonics, Wrocław University of Technology. Further details on the measurement system can be found in recent papers from this group [162, 177].

3.6 Characterization of Viscosity-Modifying Agents (Crowders)

Most experiments described herein were performed in aqueous polymer solutions. They are frequently used as model complex liquids since their characteristic length-scales are well defined, which facilitates a general physical description. The polymer of choice was polyethylene glycol (PEG), which is soluble in water, flexible, relatively inert and biocompatible. To capture the influence of the system geometry (polymer hydrodynamic radius, correlation length) on mobility of probes and viscosity at different length-scales, a broad range of polymer molecular masses and concentrations was tested.

The average molecular masses as well as dispersity of polymers purchased from Sigma-Aldrich were established by means of gel permeation chromatography

(GPC). These PEGs had long tails of distribution of M_n, which would in some cases impair proper interpretation of the results. Therefore, PEGs of low Đ index were purchased from Polymer Standards Service GmbH (Mainz, Germany). Such high-grade polymers are usually used as calibration standards for chromatography. Therefore, in this case GPC data were supplied by the manufacturer within appropriate analysis certificates. Most results presented throughout this Thesis concern solutions of such standards; their M_n and Đ values can be found in Table 3.2. Any samples prepared with non-standardized PEGs are denoted with an asterisk, *. To keep the notation concise and clear, PEG samples are named in short by their approximate M_n, *e.g.* „PEG 6k" denotes polyethylene glycol of M_n close to 6000 kg/mol (for exact values used for calculations, see Table 3.2).

In various experiments and reference measurements, aqueous solutions of relatively small ($R_h \leqslant 0.5$ nm), inert molecules were used. These included tetraethylene glycol (TetraEG), ethylene glycol and sucrose. All of these compounds were of high purity; TetraEG and sucrose were purchased from Sigma-Aldrich, while glycol from Chempur S.A. (Piekary Śląskie, Poland).

Table 3.2: Compilation of values of molecular weight of all the compounds used to adjust viscosity throughout the experiments, along with the dispersity indices Đ (where available) and estimated hydrodynamic radii. In case of non-polymeric compounds, M_w is molecular weight, for polymers it denotes weight-average molecular weight. * denotes non-standardized polymers.

Sample label	M_n [kg/mol]	M_w [kg/mol]	Đ	R_h [nm]	R_g [nm]
PEG 1k	895	1020	1.14	0.75	1.22
PEG 3k	2800	3052	1.09	1.41	2.31
PEG 6k	6170	6550	1.06	2.17	3.61
PEG 12k	10600	12190	1.15	3.09	5.18
PEG 18k	14900	17900	1.20	3.85	6.48
PEG 20k*	20390	28460	1.40	∼4.1	∼7.0
PEG 500k	339000	495000	1.46	25.5	45.0
PEG 600k*	–	–	–	∼28	∼50
PEG 1M	879000	941000	1.07	36.8	65.3
ethylene glycol	–	0.062	–	∼0.15	–
TetraEG	–	0.194	–	∼0.3	–
sucrose	–	0.342	–	∼0.5	–

Hydrodynamic and gyration radii of PEGs were calculated according to empirical formulae, based on light scattering experiments [179]:

$$R_{\mathrm{h}} = 0.0145 M_{\mathrm{w}}^{0.57}, \tag{3.3}$$

$$R_{\mathrm{g}} = 0.0215 M_{\mathrm{w}}^{0.583}. \tag{3.4}$$

For small crowders, R_{h} was estimated directly on the basis of molecular structure.

An important issue was preparation of the samples, especially for rheometric measurements. Polymers were dissolved and mixed for up to three days (slow dissolution kinetics being a particular problem for the high molecular weight polymers). A syringe could not be used for sample application due to the risk of disruption of the polymer network. Instead, appropriate volume of sample was measured and slowly poured into the system.

Chapter 4

Results and Discussion

The results are presented in three distinct blocks, according to the main theses stated in the abstract (page XVI). Section 4.1 deals with activation energy for mobility in polymer solutions. In Section 4.2 the influence of relaxation rate of polymer mesh on its response to mechanical stimuli is discussed. Finally, in Section 4.3 the crucial influence of local, scale-dependent viscosity on molecular motors is demonstrated.

4.1 Results: Activation Energy for Mobility

Extensive measurements of both macroscopic (rheometry) and nanoscopic (probe diffusion – FCS) viscosity were performed at a broad range of temperature (278–315 K), PEG molecular weight (3–500 kg/mol) and concentration (1–30%, upper limit depending on the M_w of the polymer). Although a significant part of the temperature dependence of viscosity came from the changes in the solvent viscosity, the decrease of relative viscosity (*i.e.* viscosity scaled by the solvent viscosity at given conditions, η_0) with increasing temperature was accurately captured. η/η_0 displayed a general exponential dependence on $1/T$; exemplary curves are given in Figure 4.1. This was in line with the predictions concerning an Arrhenius-type dependence in the formula for relative diffusivity, based on the Eyring equations [24].

Eyring's approach to diffusion and viscosity was combined with the descrip-

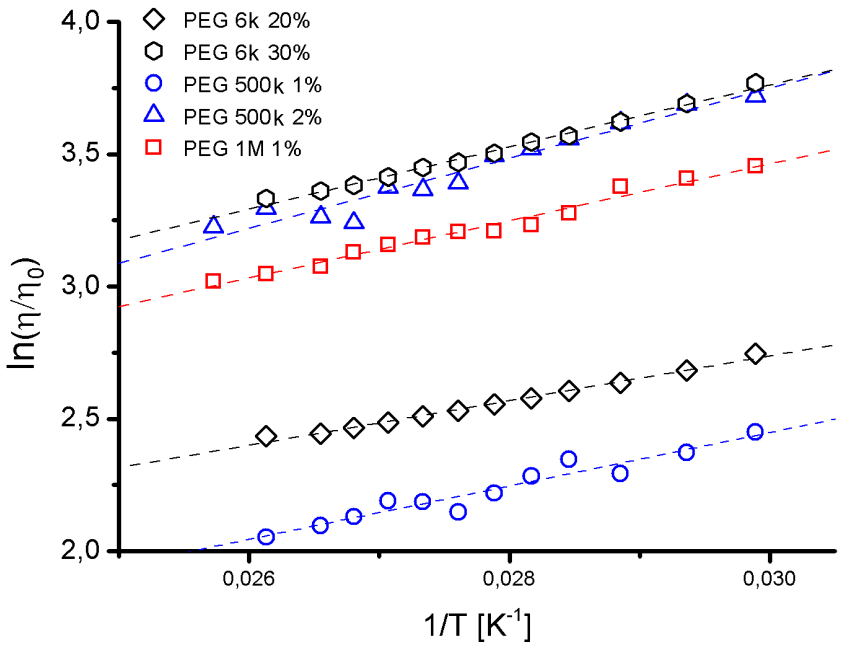

Figure 4.1: Temperature dependence of macroviscosity for exemplary PEG solutions. The differences in slopes of the curves are practically negligible, even though the results concern samples vastly differing in polymer concentration and molecular weight.

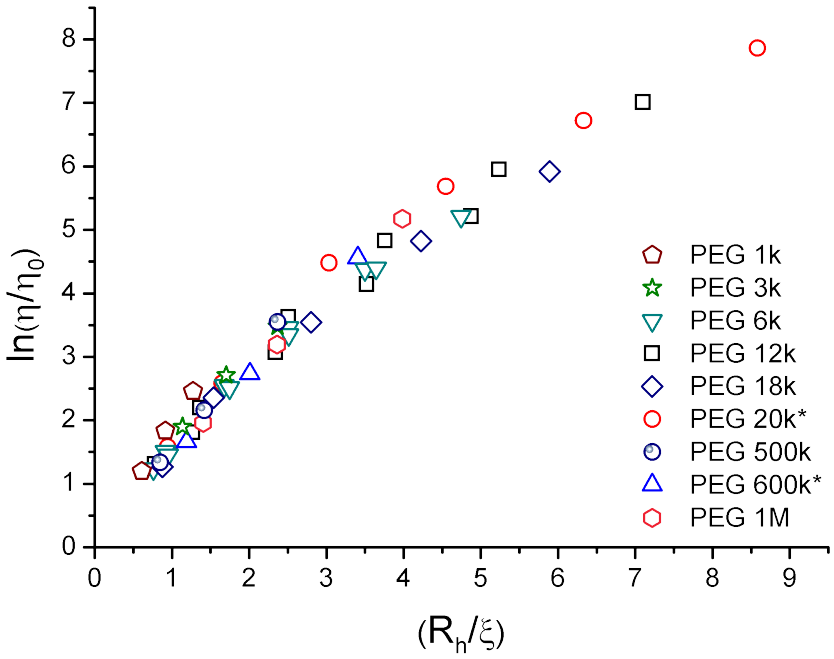

Figure 4.2: Results of additional rheometry measurements performed at 298 K, serving as a basis for estimation of parameter a for the scaling equations for PEG solutions.

tion of rheology of polymer systems based on a logarithmic dependence of relative viscosity on $(R_\mathrm{h}/\xi)^a$ [95,97] (see Section 1.5). Parameter a in analogous equations may vary from system to system, while its physical meaning is still under discussion [74]. It was established for the PEG systems in question on the basis of a separate series of rheometry measurements, conducted at 298 K. The logarithm of relative viscosity (η/η_0) was plotted against R_h/ξ (Figure 4.2). An allometric function of the type $y = b \cdot x^a$ was fitted to the datasets (separately for all the polymers). As no significant discrepancies in the obtained a values were found between the datasets, the results were averaged and thus the value of $a = 0.78$ was obtained.

Since the scaling formulae rely on the value of hydrodynamic radius of polymer coil, possible changes of R_h with temperature had to be examined. To do this, dynamic light scattering (DLS) experiments were executed. Results obtained for a dilute PEG 20k* solution are presented in Figure 4.3. The hydrodynamic radius

of the polymer coil remained constant (within the measurement error) throughout the range of temperatures exploited during rheometry and FCS experiments. This allowed for using constant values of R_h and R_g (established on the basis of Equations 3.3 and 3.4) for a given polymer.

To enable consistent presentation of the subsequent results, Equations 1.23 and 1.25 were applied to present all the data in terms of relative diffusivity (D/D_0). The results concerning temperature dependence observed in rheometric measurements were plotted against $(R_h/\xi)^a(RT)^{-1}$. As can be seen in Figure 4.4, all the data points fell onto one linear curve, regardless of the molecular weight of the polymer or its concentration.

The slope of the curves obtained from the macroscale experiments is a constant, γ, expressed in terms of energy and equal 3.96 ± 0.40 kJ/mol. The error is given here as a maximum discrepancy between the results for fits of individual datasets. γ is characteristic for the system (in this case, PEG/water) and does not depend

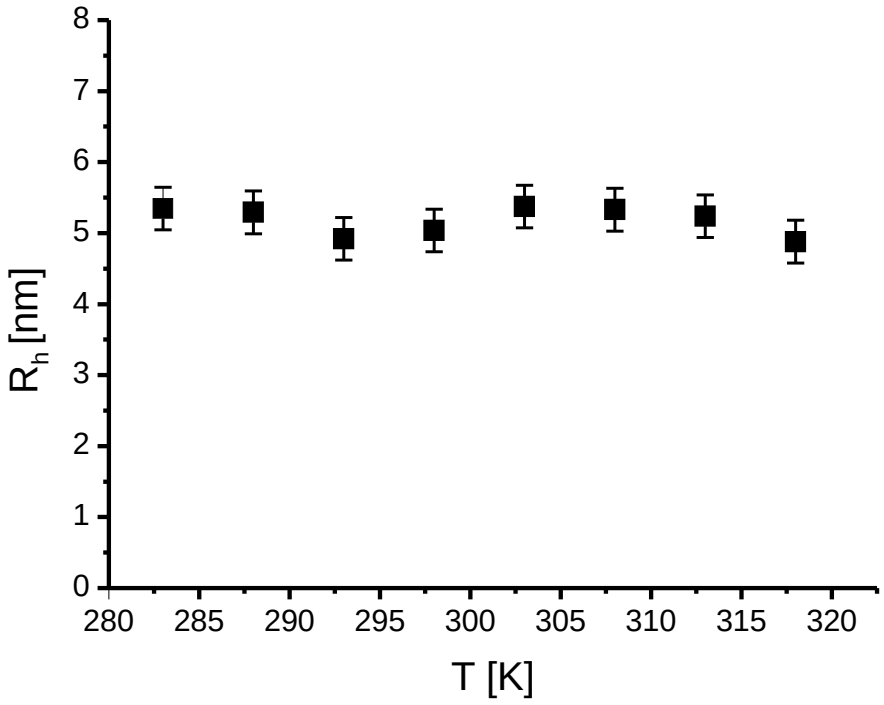

Figure 4.3: Hydrodynamic radius of PEG 20k measured at different temperatures by means of dynamic light scattering. No significant changes are observed.

on either the polymer concentration or its molecular mass. Thus the diffusion coefficient for large objects ($r_\mathrm{p} \gg R_\mathrm{h}$) is given as

$$D = D_0 \exp\left[\frac{-\gamma \left(R_\mathrm{h}\, \xi^{-1}\right)^a}{RT}\right]. \tag{4.1}$$

The above relation, according to Equation 1.23, can be rewritten to describe macroscopic viscous flow:

$$\eta = \eta_0 \exp\left[\frac{\gamma \left(R_\mathrm{h}\, \xi^{-1}\right)^a}{RT}\right]. \tag{4.2}$$

FCS measurements were performed to investigate whether this kind of dependence can be transferred to mobility of probes of nanometer-range size. In this case probe radius, r_p, became an additional variable. It was included by substitution of R_h with effective radius R_eff, defined in Equation 1.27. Such approach was justified, as the macroscopic flow was the limiting case for the postulated scaling: $\lim_{r_\mathrm{p}\to\infty} R_\mathrm{eff} = R_\mathrm{h}$.

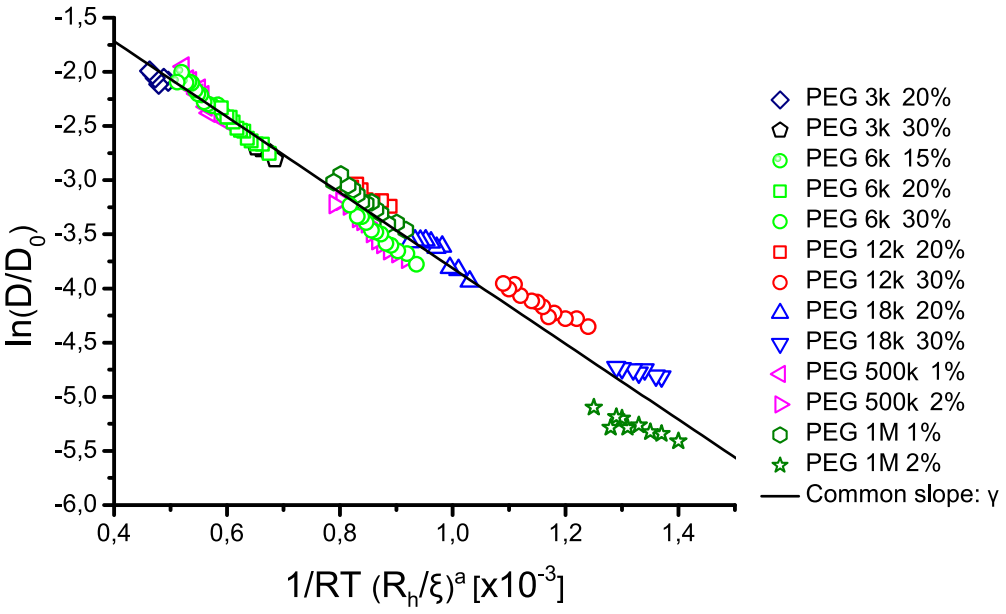

Figure 4.4: Relative diffusivity at the macroscale for different PEG solutions plotted according to the proposed scaling equation. The slope of the concentrate linear fit corresponds to the coefficient γ (see Equation 4.1), equal *ca.* 3.96 kJ/mol. The data are presented as diffusivity instead of viscosity (which was directly measured) to provide a straightforward comparison to the subsequent FCS results. Conversion from η/η_0 to D/D_0 is done according to Equation 1.23.

Logarithm of the relative diffusivity measured for the molecular probes depended reciprocally on the temperature, similarly as was observed for macroscopic flow. Diffusivity scaling was included in an analogous way as at the macroscale, using R_{eff} instead of R_{h}. For each probe/polymer system, all the results fell along a straight line on the scaling plot (Figure 4.5). Therefore, a modification of Equation 4.1 was proposed to include scaling with the probe and polymer chain sizes:

$$D = D_0 \exp\left[\frac{-\gamma \left(R_{\mathrm{eff}}\, \xi^{-1}\right)^a}{RT}\right]. \tag{4.3}$$

The above relation can be rewritten to describe the effective viscosity experienced by a probe diffusing in a polymer solution:

$$\eta_{\mathrm{eff}} = \eta_0 \exp\left[\frac{\gamma \left(R_{\mathrm{eff}}\, \xi^{-1}\right)^a}{RT}\right]. \tag{4.4}$$

The obtained results and their proposed description proved to be fully consistent with the viscosity scaling postulated previously [95, 97]. By analogy to the original Eyring rate theory, the denominator in Equation 4.3 was interpreted as the excess of activation energy for diffusion over the value characteristic for pure

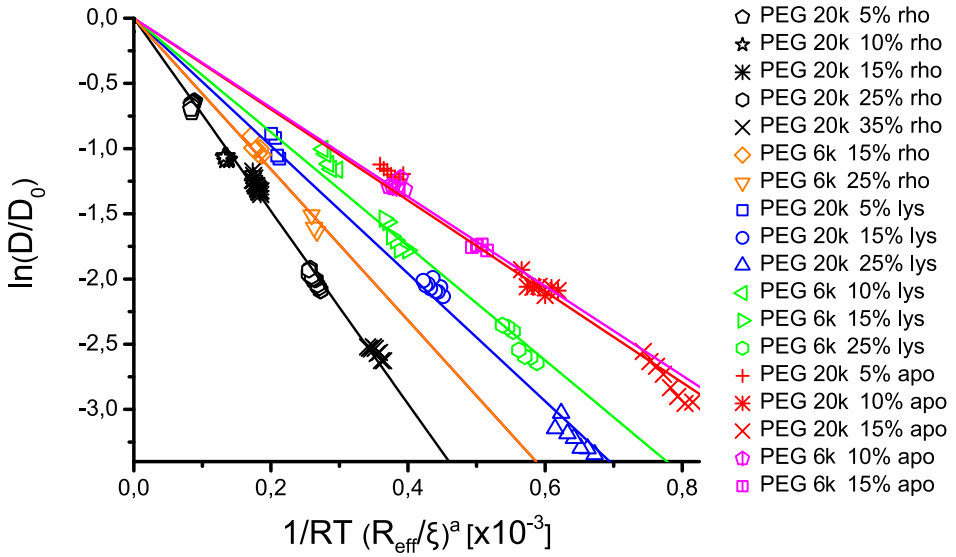

Figure 4.5: Relative diffusivity experienced by molecular probes in PEG solutions plotted according to the proposed scaling equation. Probe descriptions: rho – rhodamine ($r_{\mathrm{p}} = 0.52$ nm); lys – lysozyme ($r_{\mathrm{p}} = 1.9$ nm); apo – apoferritin ($r_{\mathrm{p}} = 6.9$ nm).

solvent, ΔE_a:

$$\Delta E_a = \gamma \left(\frac{R_{eff}}{\xi} \right)^a . \tag{4.5}$$

The FCS results matched the proposed scaling of relative viscosity very well. However, in contrary to the macroscopic case, significant differences in the obtained γ values were observed between different probe/polymer systems. The changes were systematic and corresponded to the transition from the macro- to nanoviscosity range, as shown in Figure 4.6. For systems characterized by $r_p/R_h > 1$, the values of γ coefficient obtained from FCS experiments approached a constant, reproducing the macroscopic value (within experimental errors). This supports both the high quality of the obtained results and the postulated identity in the description of viscous flow and probe diffusion. In the $r_p/R_h > 1$ range the probe gradually starts to experience the macroscopic viscosity of the solution [97]. This smooth shift is manifested by changes in both the relative diffusion coefficient

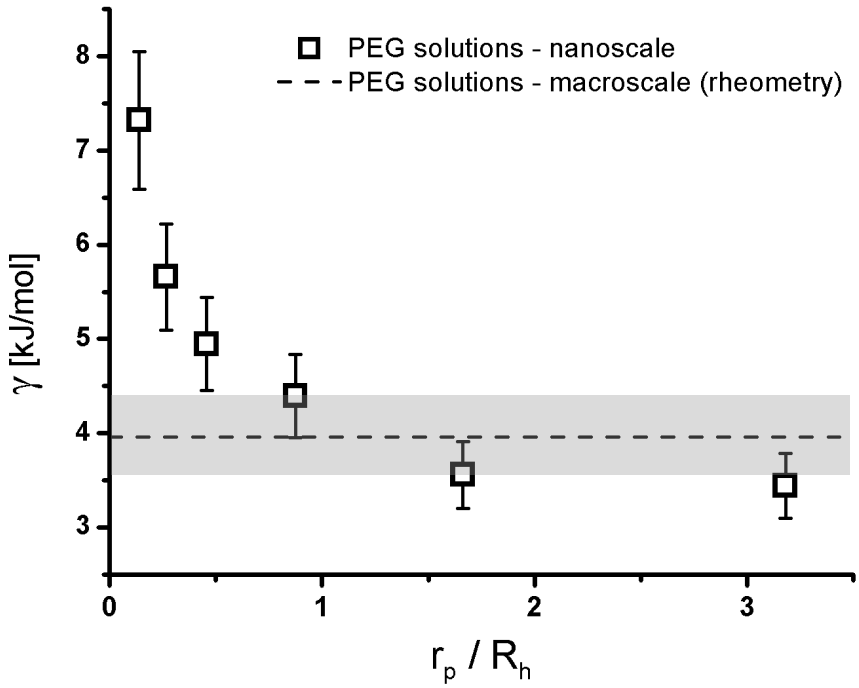

Figure 4.6: Dependence of the γ coefficient (appearing in Equations 4.3 and 4.5) on the probe/polymer size ratio. Relatively large molecular probes reproduce well the results of macroviscosity measurements. The shaded range denotes the maximal error of rheometry results.

Table 4.1: Excess of the activation energy over the one in pure water, ΔE_a; exemplary data for PEG aqueous solutions ($M_n = 20$ kDa). D_0 refers to diffusion in pure water. The activation energy for self-diffusion of water is 19 kJ/mol [181]. According to Equation 1.23, relative diffusivity is an inverse of relative viscosity, which is how the reference values for macroscopic flow are calculated.

Probe, r_p [nm]	Concentration	D/D_0 at 298 K	ΔE_a [kJ/mol]
rhodamine, 0.5	10%	0.34	2.50
lysozyme, 1.9		0.30	4.04
apoferritin, 6.9		0.13	5.17
macroscopic flow		0.077	6.37
rhodamine, 0.58	25%	0.13	4.87
lysozyme, 1.9		0.038	7.87
macroscopic flow		0.0067	12.4

D/D_0 and the excess activation energy ΔE_a – an exemplification can be found in Table 4.1.

The results presented in this Section were published in a paper in *Physical Review Letters* [180].

4.2 Results: Dynamic Depletion Layer Effect

The response of polymer mesh to mechanic stimuli was investigated by means of a quartz tuning fork (QTF) oscillator (see Section 2.5). However, first, reference measurements of viscosity of PEG solutions (same as used later on for QTF experiments) were performed by means of rotational rheometer. Five PEG molecular mass standards were investigated; for each of the polymers, solutions of three different concentrations were prepared. Additionally, few measurements for broad-distribution PEGs were made. The obtained viscosity values ranged from less than 1 to over 150 mPa·s. The results agreed very well with the previously postulated scaling formula for viscosity of complex liquids (Equation 1.28) [97], as can be seen in Figure 4.7.

To investigate the viscoelasticity of the solutions, oscillatory rheometric mea-

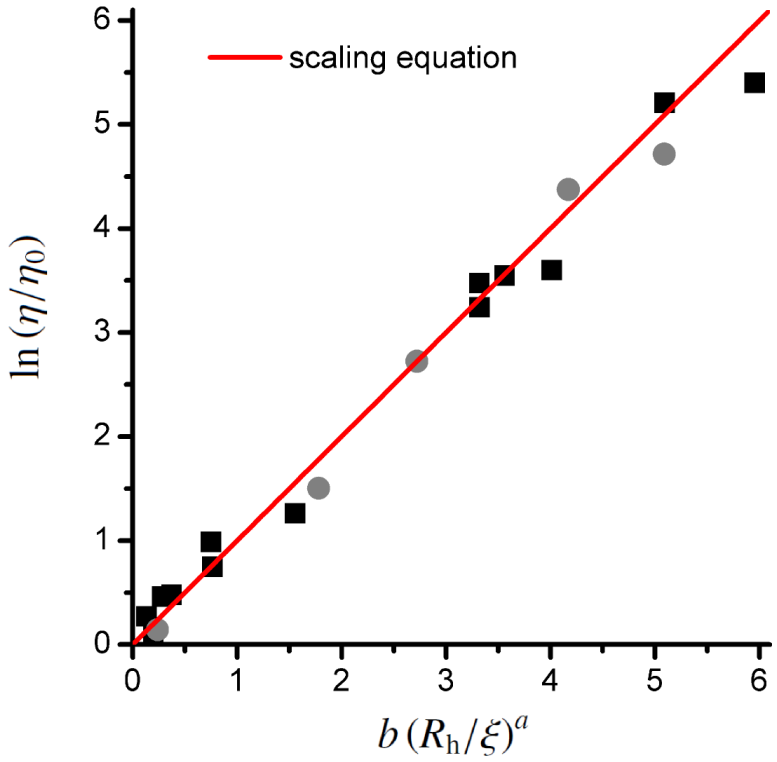

Figure 4.7: Experimental data on the viscosity measured by means of the rotational rheometer, overlaid with the viscosity scaling relation (Equation 1.28). Full consistency is observed. Gray circles correspond to non-standardized polymers of broad M_w distribution.

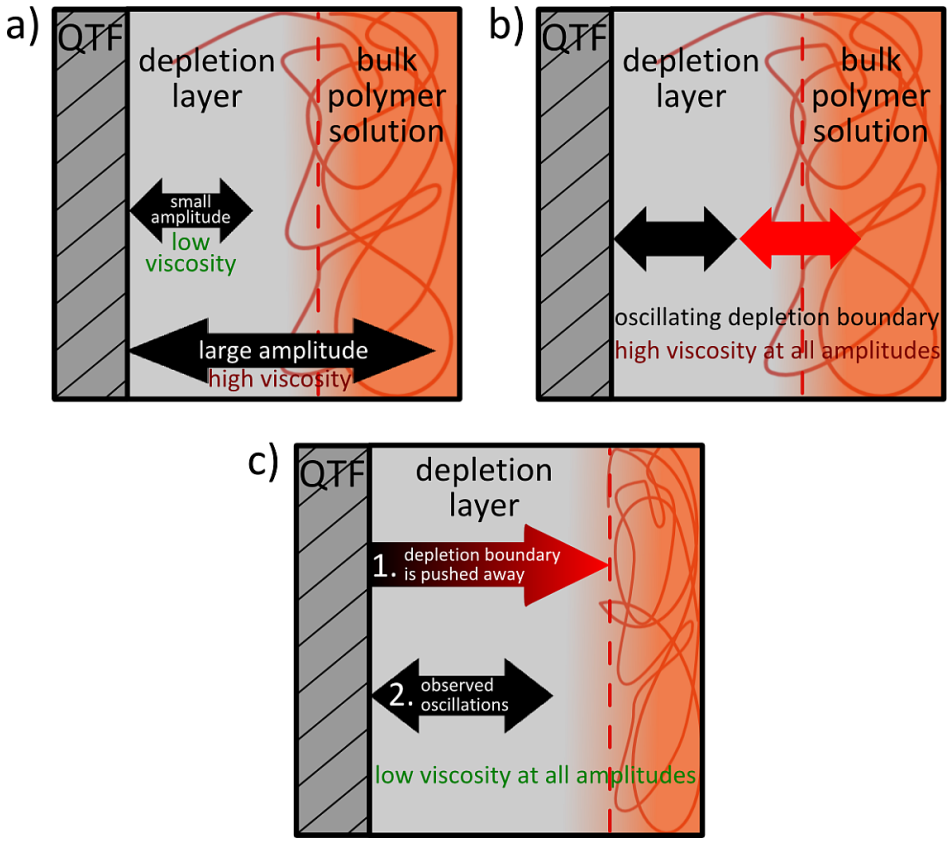

Figure 4.8: Different considered models of depletion layer at an oscillating wall in a polymer solution. a) The depletion layer is static, viscosity at small oscillation amplitudes is of the order of solvent viscosity, strongly increasing when the amplitude exceeds the DL thickness; b) Due to hydrodynamic forces, the depletion layer is moved together with the wall, therefore bulk viscosity is observed irrespective of the oscillation amplitude (the DL is moved as if it was an intrinsic element of the QTF); c) The oscillating wall forces broadening of the depletion layer, so that its thickness corresponds to the oscillation amplitude (polymer chains are pushed away from the surface and do not relax fast enough to fill the available space).

surements were performed. In an attempt to determine the linear viscoelastic region, the G' storage modulus was recorded at variable amplitude of the rheometer geometry oscillations and frequency of 1 Hz, which is a standard value for such experiments. Irrespective of the shear strain, the measured values of G' were below the sensitivity of the apparatus (nothing but the inertia of the geometry was observed). This suggested purely viscous behaviour of the bulk samples, which was in line with the fact that in rotational measurements the recorded viscosity did not change with the shear rate.

While preparing the QTF experiments, different hypotheses concerning the response of the polymer system to oscillations were taken into account, basic three of which are schematically depicted in Figure 4.8. The thickness of the DL was

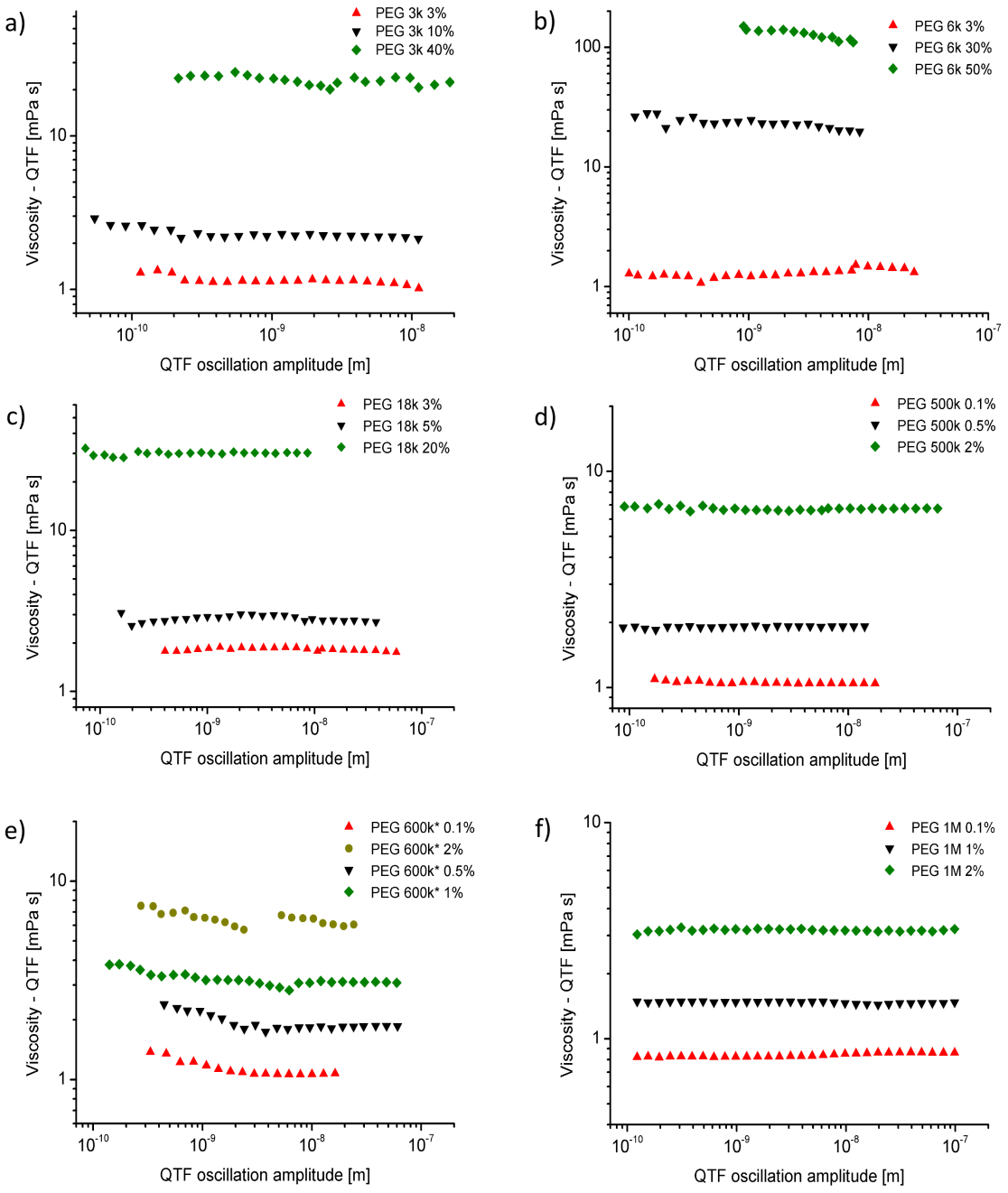

Figure 4.9: Viscosity measured by the QTF in solutions of PEGs: 3k, 6k, 18k, 500k, 600k*, 1M (panels a)-f)) plotted against the fork oscillation amplitude. Bulk viscosities of solutions denoted with symbols matching in both graphs (e.g. 6 kDa 50% and 1 MDa 2%) are roughly the same.

roughly approximated by the values of gyration radii of the polymers [112, 116], *i.e.* ranged from *ca.* 2 to 70 nm for different polymers. Therefore, the experiments were designed so that the amplitude of the oscillations of the QTF would in all cases range both above and below this value. Particular attention was given to measurements of viscosity experienced at low amplitudes. Effectively, it came down to an amplitude range from tens of picometers to *ca.* 100 nanometers.

If the depletion zone boundary did not follow the oscillations nor rearrange in any way (static depletion layer), a distinct crossover should be visible. For small displacements, the fork would experience the low viscosity of the DL (similar to the solvent viscosity), while for displacements exceeding the thickness of the DL, a much higher viscosity of bulk polymer solution would be observed (Figure 4.8a). Moreover, for large initial amplitudes a double-exponential decay of oscillations would be observed. First, heavy damping in the polymer would take place, followed by slow decay when the oscillation amplitude decreased into the depletion zone. However, this was not the case: all the decay patterns fitted perfectly to a single-exponential decay. No meaningful dependence of the measured viscosity on the initial amplitude for any of the samples was observed, as can be seen in graphs in Figure 4.9.

For all solutions of polymers of $M_w < 20$ kg/mol very good agreement between the results from QTF and rheometry measurements was obtained. The QTF method proved therefore accurate even for solutions of viscosity two orders of magnitude greater than the viscosity of water.

An interesting observation was made for solutions of high-M_w polymers (500k, 600k, 1M). Although the viscosity measured with the QTF did not depend on the oscillation amplitude, it was overall much lower than the reference bulk value. For example, in the case of the 2% solution of PEG 1M, the observed discrepancy was fifty-fold. A comparison of viscosities measured with QTF and rheometry is presented in Figure 4.10.

The observed discrepancy between QTF-measured and bulk viscosity for so-

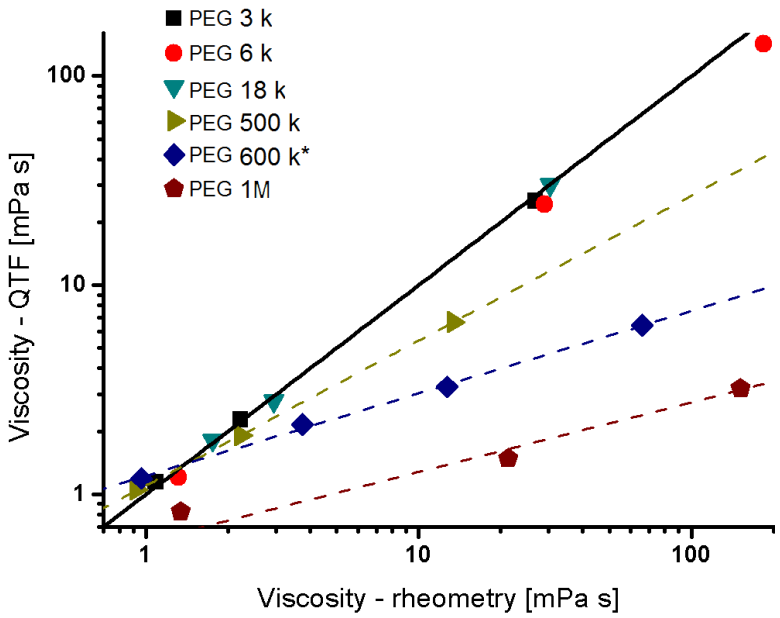

Figure 4.10: Log-log plot comparing viscosities measured by rotational rheometry and QTF. For polymers of $M_w < 20$ kg/mol very good conformity is observed, whereas for high-M_w PEGs significant differences appear. Dashed lines are drawn as a guide for the eye, connecting points corresponding to solutions of same polymer differing in concentration.

lutions of high-M_w PEGs did not seem to find any direct explanation in the size domain (mesh structure). Therefore, the time domain was explored, *i.e.* the dynamic properties of the polymer solutions. Dynamic light scattering was used for that purpose. In all solutions of low-M_w polymers (up to 18k), a single-component fit of the correlation function matched the results very well. However, in semi-dilute solutions of high-M_w PEGs two distinct relaxation modes were observed – exemplary DLS curves are shown in Figure 4.11. The fast mode is ascribed to local relaxation of polymer chains [182] within a single blob of the size corresponding to the correlation length [183]. This is in line with the DLS results, supported also by literature data [184]: the fast mode relaxation time shortens with increasing polymer concentration. As the concentration increases, the correlation length (and, consequently, the blob size) decreases, restricting the length-scale and time-scale of the fast relaxation mode. On the other hand, for the slow mode an increase in relaxation times with polymer concentration was observed. Although the exact

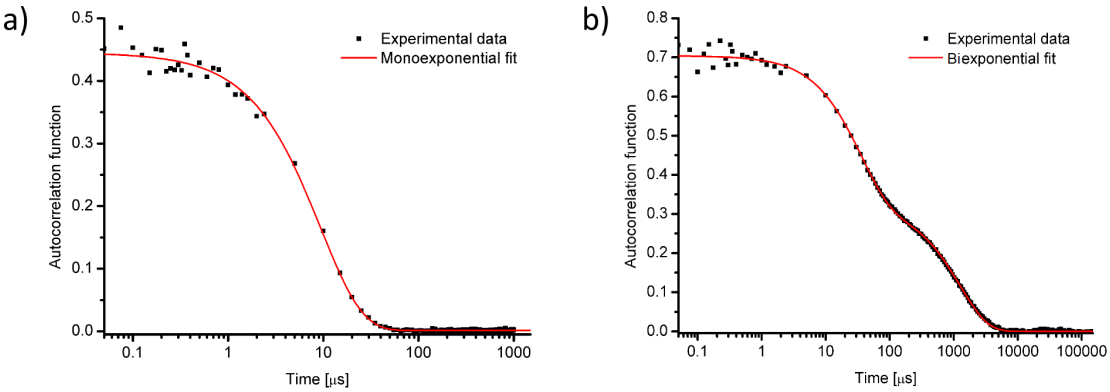

Figure 4.11: Exemplary dynamic light scattering (DLS) correlation curves obtained at $\theta = 90°$for PEG solutions: a) 18k, 5%, monoexponential decay; b) 500k, 2%, double-exponential decay.

interpretation of the origin of the slow mode is still debated, it is generally related to the hindered motions of the entire entangled chains [16]. For small polymers, both phenomena (movement within blobs and of mesh segments) occur at similar length- and time-scales and cannot be easily distinguished. In the hereby described case, the slow relaxation mode should reflect the ability of the polymer mesh to react to the displacement of the QTF prongs.

For each of the samples, we performed DLS measurements at 7 different θ angles, ranging from 30° to 150°. Therefore, the length of the wave vector $\mathbf{q}$ (calculated using Equation 2.15) covered the range of *ca.* 30 to 120 nm. Diffusion times τ_D were established from fitting of the autocorrelation curves – the results are given in Table 4.2. Only the slow mode was taken into account when bimodal correlation curves were observed (*i.e.* for semi-dilute solutions of high-M_w polymers). In the 500k 0.1% solution only one mode was observed due to the fact that the solution fell in the dilute concentration regime and therefore the chains were not interpenetrated (separate coils were present in the solution rather than a polymer mesh). Characteristic diffusion coefficients D were calculated as slopes of the linear plots of τ_D^{-1} drawn as a function of $|\mathbf{q}|^2$ (see Equation 2.16). According to the favoured interpretation of the long relaxation mode, D in semi-dilute solutions refers to motion of large segments of the entangled polymer system,

providing information about the dynamics of the mesh.

The frequency of QTF vibrations was fixed in all the performed experiments (resonance frequency was determined by the geometry of the fork prongs) and the oscillation period τ_{osc} was equal to 37±2 μs. The slight shifts of τ_{osc} were due to differences in sample density and no indication of polymer adsorption on the QTF surface was observed. To incorporate the DLS results into the interpretation of QTF measurements, diffusion coefficients were used to calculate root mean square displacement of polymer mesh segments, d_{RMS} occurring during a single

Table 4.2: Diffusion coefficients D (both slow and fast mode) obtained from DLS measurements for different PEG solutions. For each sample, autocorrelation of scattered photons was captured at 7 different θ angles (30 – 150°), *i.e.* at different wave vectors $\mathbf{q}$. Fitting of mono- or biexponential models yielded characteristic correlation times τ_{D}. D values were calculated as slopes of the linear $\tau_{\mathrm{D}}^{-1}(|\mathbf{q}|^2)$ plots. d_{RMS} was calculated as $d_{\mathrm{RMS}} = (6D\tau_{\mathrm{osc}})^{1/2}$, where τ_{osc} is the QTF oscillation period (∼37 μs). d_{RMS} is a measure of space explored by segments of the polymer mesh during a single QTF oscillation period; therefore, for high-M_{w} PEGs it concerns only the slow diffusion mode. Asterisk denotes non-standardized polymer of broad M_{w} distribution.

Polymer	% w/w	D_1 [μm^2 s^{-1}]	D_2 [μm^2 s^{-1}]	d_{RMS} [nm]
3 kDa	3%	146.8	–	181
	10%	180.7	–	200
	40%	211.3	–	217
6 kDa	3%	109.2	–	156
	30%	250.2	–	236
	50%	225.1	–	224
18 kDa	3%	81.6	–	135
	5%	87.7	–	140
	20%	148.2	–	181
500 kDa	0.1%	11.0	–	49.4
	0.5%	36.0	2.70	24.5
	2%	47.5	0.88	14.0
600 kDa*	0.1%	22.6	4.51	31.6
	0.5%	23.0	2.14	21.8
	1%	25.5	0.21	6.9
	2%	30.3	0.073	4.0
1 MDa	0.1%	11.9	1.02	15.1
	1%	24.9	0.077	4.1
	2%	38.3	0.017	2.0

τ_{osc} period:

$$d_{\mathrm{RMS}} = (6D\tau_{\mathrm{osc}})^{1/2}. \tag{4.6}$$

d_{RMS} is a measure of the extent of space, at which polymer relaxation can be expected during the QTF oscillation period. Another key factor is the thickness of the equilibrium DL, which determines the extent of space at which a decrease of polymer concentration is observed at equilibrium conditions. As the DL boundary is not sharp nor well defined, we shall settle with the rough approximation of the DL thickness as R_{g} in the further discussion.

The dependence observed in Figure 4.12 implies a direct relation between the decrease of QTF-measured local viscosity of entangled solutions of high-M_{w} polymers and the geometric parameters d_{RMS} and R_{g}. Let us consider the limiting case for long polymer chains, when $d_{\mathrm{RMS}} \ll R_{\mathrm{g}}$, *i.e.* the mesh relaxes very slowly and the depletion region is relatively broad. At low initial amplitudes of QTF oscillations ($A_i \ll R_{\mathrm{g}}$), the DL/bulk boundary can be treated as stationary. The QTF moves within the DL, experiencing viscosity similar as in pure solvent. However, when A_i approaches or exceeds R_{g}, the QTF-measured viscosity does not increase. This can be explained by the „dynamic depletion" phenomenon: during the initial phase of forced oscillations, the polymer is pushed away and the DL is broadened (*cf.* Figure 4.8c). Since the relaxation of the polymer mesh is slow, the boundary of the DL does not follow the motion of the QTF. Therefore, only the low viscosity of the DL is observed.

On the other hand, when $d_{\mathrm{RMS}} \gg R_{\mathrm{g}}$, the polymer chains are mobile and the mesh can follow the movement of the QTF in an extent sufficient for dynamic reconstruction of the DL. Even at small amplitudes ($A_i < R_{\mathrm{g}}$) the DL/bulk boundary is not immobile: it follows the oscillations of the QTF to keep the equilibrium thickness of the DL at any given point of the oscillation cycle. Such assumption is fully supported by experimental data: for all QTF measurements in the $d_{\mathrm{RMS}} > R_{\mathrm{g}}$ regime (*i.e.* for polymers of $M_{\mathrm{w}} < 20$ kg/mol), bulk viscosity was reproduced within a 15% error margin, irrespective of the amplitude. Unfortu-

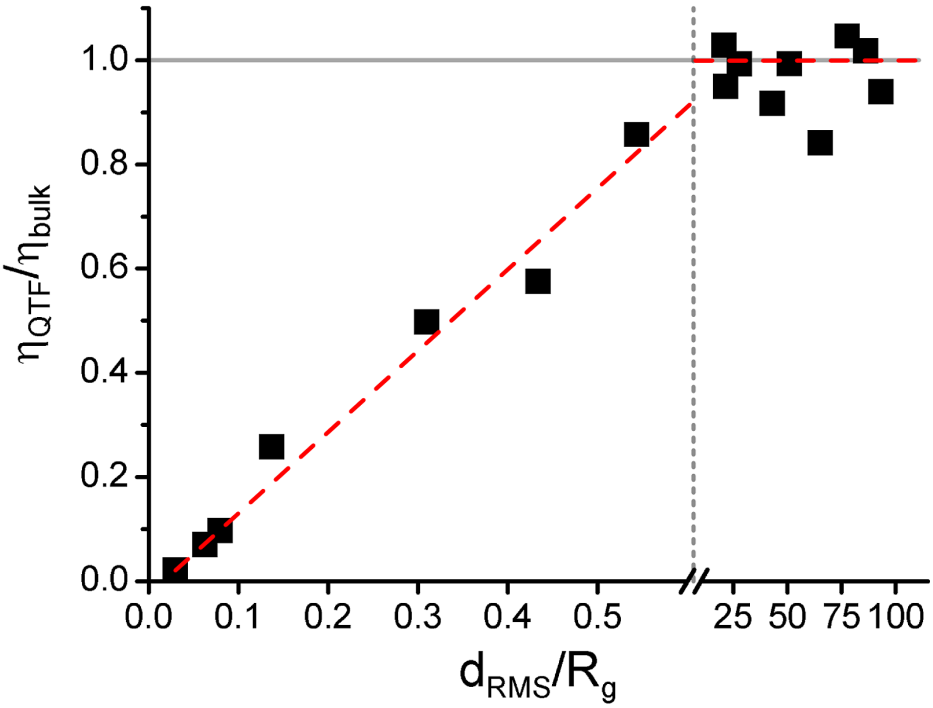

Figure 4.12: QTF-measured viscosity of entangled polymer solutions strongly decreases when d_{RMS}, *i.e.* root mean square displacement of a polymer unit during one QTF oscillation period, drops below the thickness of the depletion layer (roughly approximated by the polymer gyration radius, R_{g}). In this regime, the DL/bulk solution boundary approaches a stationary state, while the QTF moves inside the DL. Oscillation amplitude is not relevant: even if $A_i \gg R_{\mathrm{g}}$, the DL is broadened to A_i during the initial period of the experiment (forced QTF oscillations), while its return to the equilibrium state is relatively slow at low d_{RMS}. Dashed red line is drawn as a guide for the eye.

nately, due to technical limitations we were not able to perform measurements at A_i exceeding d_{RMS} for the low-M_{w} polymers (where d_{RMS} is of the order of hundreds of nm – see Table 4.2). However, the limiting case for high amplitudes of QTF oscillations in PEG solutions is simple Newtonian flow at high shear rate, characterized by the bulk solution viscosity. Therefore, no significant changes of effective viscosity at high amplitudes should be expected.

There are no other available reports on viscosity measurements conducted by means of a QTF in complex liquids, where the DL dynamics could be probed. Quartz crystal microbalance (QCM) viscosity measurement method has been applied to polymer solutions and a significant decrease in viscosity compared to the

bulk value was observed [164, 165]. The authors attributed this phenomenon to the adsorption of polymer on the microbalance surface. However, in the view of current results and the development of the DL theory, it seems that this effect could have rather been due to depletion: since in case of QCM oscillations occur only in the direction parallel to the surface, the shear is mostly constrained to the low-viscosity, polymer-depleted zone. In case of QTF, which is a 3D object immersed in the sample, most friction is due to movement of the prongs normal to their surface. Therefore, physically different phenomena are observed than for QCM and dynamics of the DL can be probed. Moreover, no adsorption of polymer on the QTF surface was noticed (which would be apparent by changes in the resonance frequency).

The results presented in this section were published in an article in *Soft Matter* [185].

4.3 Results: Motion of Kinesin in Crowded Environment

The crucial experiments concerning mobility of kinesin-1 in crowded environment were performed by means of total internal reflection fluorescence microscopy (TIRF – see Section 2.2). Microtubules (MTs) were synthesized and attached to cover-glass surface in a flow channel, which was then filled with motility buffer containing *i.a.* kinesin and appropriate crowders. Details concerning the preparation of stepping assays were described in Section 3.2. A range of substances was used to modify the viscosity of the motility buffer: PEG 6k, 18k, and 1M, tetraethylene glycol (TetraEG), as well as sucrose. A range of concentrations was examined for each of these substances. Reference viscosity measurements of the solutions were performed using the rotational rheometer.

In the control motility experiments an average kinesin velocity of 810 nm/s was observed, which was the expected value [124, 127, 186]. For 1M PEG solutions, no significant deviations from this value were observed – even at PEG concentration of 2%, which corresponded to viscosity of 116 mPa·s (*i.e.* 111 times the viscosity of the buffer). The conclusion that high macroscopic viscosity does not by itself impair the mobility of kinesin was in line with previous studies concerning work of molecular motors against viscous load [130, 131]. However, increasing the concentration of the 6k or 18k PEG, TetraEG, or sucrose in the kinesin solution caused gradual decrease of the stepping velocity and, at a certain point, utter arrest of motion, as depicted in Figure 4.13a.

Although results obtained for low- and high-M_w crowders seem incongruous, they are easily reconciled within the viscosity scaling paradigm (see Section 1.5). Following the idea that diffusion of the kinesin head from one binding site on the microtubule to the next one is amongst the crucial phases of the motor's step [120, 126, 133], effective viscosity η_{eff} experienced by the head was estimated for all the investigated solutions. The head was approximated as a sphere of

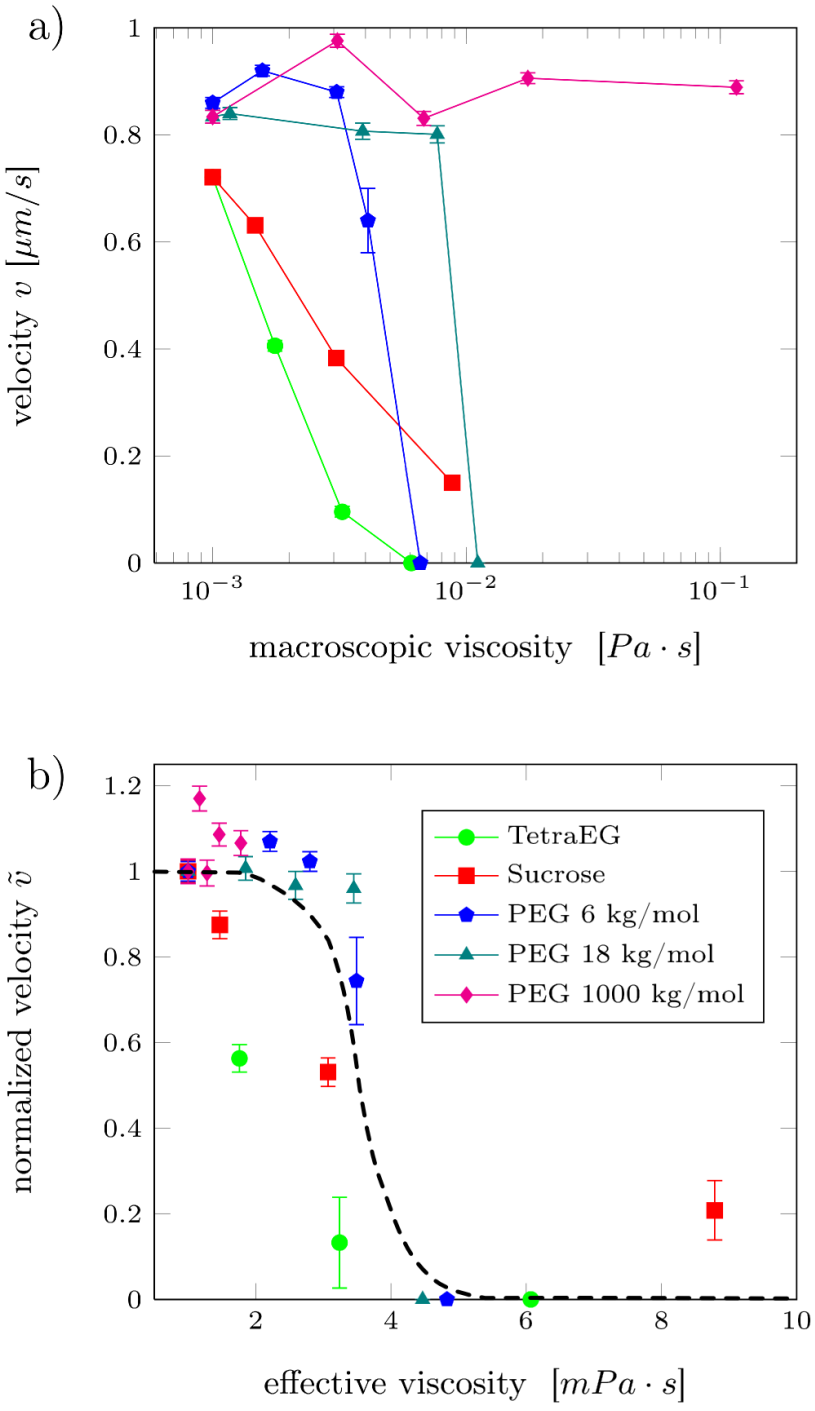

Figure 4.13: Velocity of kinesin-1 motion along the MTs measured in stepping motility assays. a) v plotted against the macroscopic viscosity; b) $\tilde{v}$ (velocity normalized by the v_0 velocity obtained in control experiment in the absence of crowders) plotted against the effective viscosity experienced by an individual kinesin-1 head domain (Equation 1.28). Dashed line drawn as a guide for the eye. Legend refers to both panels.

diameter of 5 nm. Equation 1.28 was applied, with scaling parameters established beforehand for aqueous PEG solutions [97, 180]. η_{eff} calculated for small crowders is equal to macroscopic viscosity η; however, significant discrepancies between these two values arise for large crowders, as can be seen in Figure 4.14. In the 1M PEG solutions, η_{eff} for a 5 nm sphere is of the order of pure solvent viscosity. Therefore, the effect of large crowders on the motion of kinesin is negligible (the motor domain experiences no viscosity increase), which is in line with previous studies [130, 131].

The depletion effect occurring in polymer solutions should also be considered (see Section 1.6). The depletion layer extends over distances comparable to the hydrodynamic radius of the polymer coil – which, in case of 1M PEG is more than 35 nm [179]. This causes an apparent facilitation for kinesin motion, hence the concentration of polymer is additionally decreased in the vicinity of the

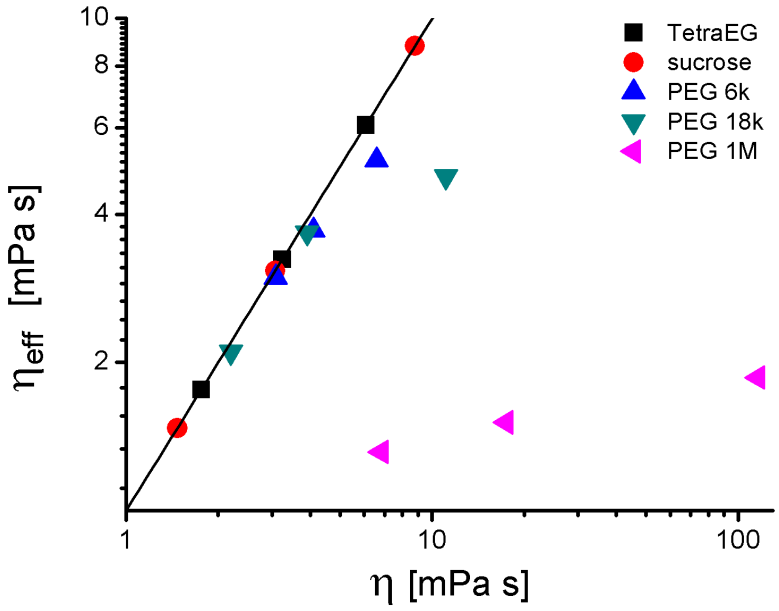

Figure 4.14: Relation between the effective viscosity experienced by the kinesin head (calculated) and macroscopic viscosity of different solutions. For low-M_{w} crowders, the two values are nearly identical (solid line). However, for 1M PEG solutions, η_{eff} is lower than η by even two orders of magnitude.

microtubule. The situation becomes qualitatively different for polymers of low molecular weight. Hydrodynamic radii of 6k and 18k PEGs are 2.17 and 3.85 nm, respectively. Therefore, the kinesin head detaching from the microtubule does not remain in the depletion zone. Moreover, the difference between η and η_{eff} for an object of the size of kinesin head becomes negligible, as depicted in exemplary plots of η_{eff} (scaled by solvent viscosity η_0) *vs.* r_{p} in Figure 4.15. This is also the case for sucrose and TetraEG solutions.

A decrease of the kinesin velocity with increasing η_{eff} is observed, with a complete arrest of motion at *ca.* 5 mPa·s, as depicted in Figure 4.13b. Also, a change in the fraction of mobile kinesin molecules is apparent, especially in case of TetraEG and sucrose: while in dilute solutions the recorded fluorescent particles are mostly mobile, in the concentrated ones walk events became rare (in spite of the same kinesin concentration).

The relationship between the observed kinesin stall and the mechanism of its

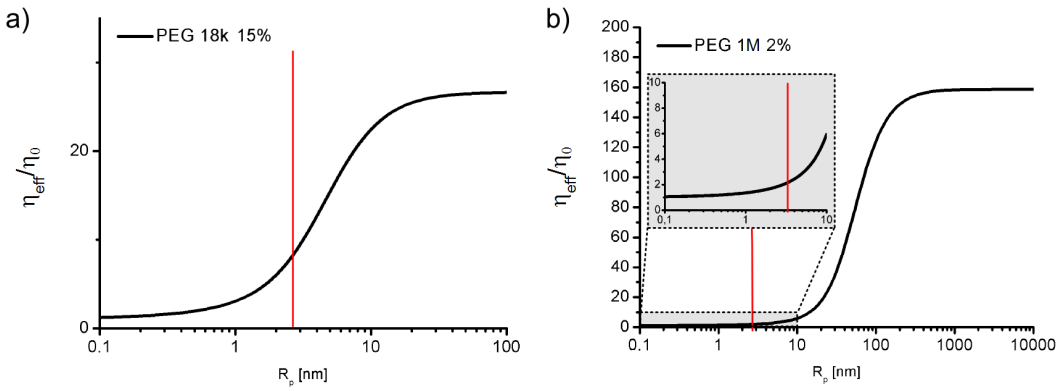

Figure 4.15: Viscosity scaling according to Equation 1.28. Effective viscosity η_{eff} of a complex liquid experienced by a probe is a function of the hydrodynamic radius of the probe, r_{p}. Plots a) and b) illustrate this dependence for a 15% aqueous solution of 18k PEG and a 2% solution of 1M PEG, respectively. η_0 is solvent viscosity. Red line corresponds to estimated r_{p} of a kinesin head. Although the macroscopic viscosity (large probe limit) in case a) is lower than in case b) by nearly an order of magnitude, the kinesin head experiences lower viscosity in case b).

processive motion can be established on the basis of the well-grounded model, summed up in a recent paper from the Block group [187]. The main phases of a single step according to this model are schematically depicted in Figure 4.16. In the following paragraphs, different possible reasons for loss of kinesin functionality in crowded environment are critically evaluated.

Hypothesis 1: Protein aggregation – no binding to microtubules. Presence of a significant amount of polymer in a protein solution may lead to aggregation due to the depletion forces and excluded volume effects [102, 188, 189]. This possibility was ruled out by fluorescence correlation spectroscopy (FCS) measurements. The measured diffusion times of Kin430-GFP in solutions of TetraEG (concentrations up to 50%) and PEG 18k (up to 15%) are presented in Figure 4.17.

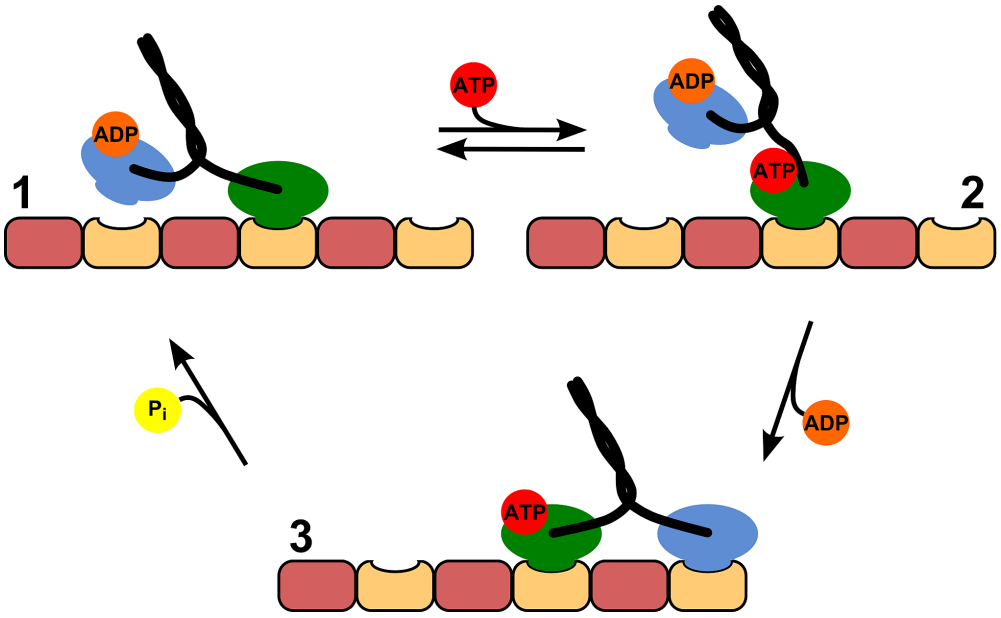

Figure 4.16: Mechanism of the kinesin forward step along the microtubule (MT). The protein spends most of the time in the ATP-waiting state, **1**. Binding of ATP changes the conformation of the MT-bound head, presumably enhancing the orientational freedom of the linker. The **1**→**2** reaction is largely reversible [187]. As long as ATP is coupled to the MT-bound head, the free head can reach the subsequent binding site on the MT and release ADP. The movement is realized by diffusion, constrained by tension arising in the linker. ATP is hydrolysed to detach the trailing head from the MT (**3**→**1**) and the system returns to the ATP-waiting state.

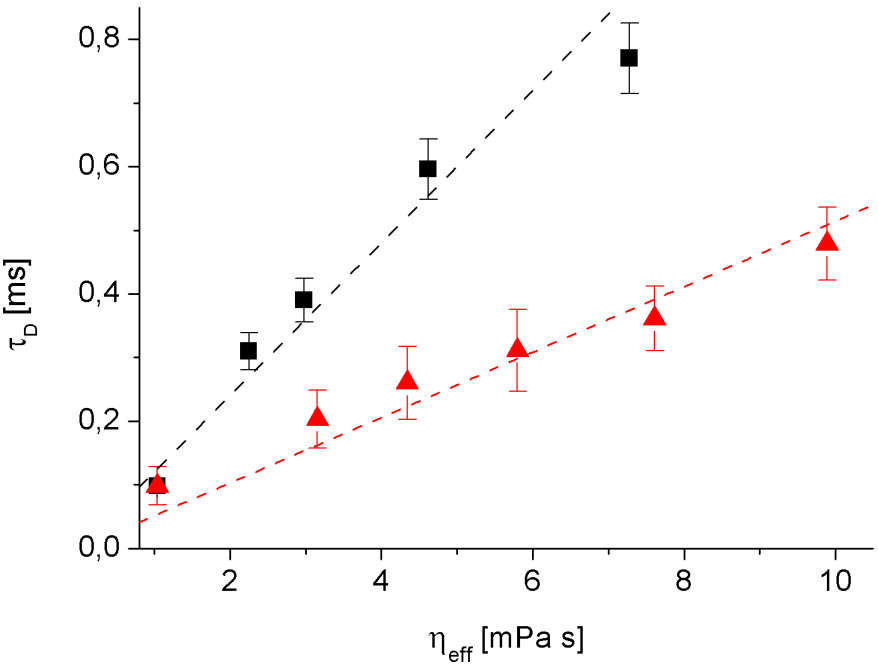

Figure 4.17: Diffusion times τ_D of kinesin measured by FCS for different concentrations of TetraEG (black squares) and 18k PEG (red triangles). In both cases, the diffusion times depend linearly on the effective viscosity experienced by the protein, η_{eff}. No aggregation of kinesin is observed, which would cause a rapid, non-linear increase of diffusion time due to a change of the hydrodynamic radius of the probe. The difference in slopes is mostly due to expansion of the focal volume in TetraEG solutions of high refractive index.

In both cases, the decrease of diffusion rate is linearly correlated with the increase of the effective viscosity of the solution. This implies that the hydrodynamic radius of the protein remains constant irrespective of the crowder concentration, thus disproving kinesin aggregation. Furthermore, in TIRF experiments immobile fluorescent particles were observed at the MTs. This suggests that kinesin binding to the MTs was not disabled.

Hypothesis 2: Osmotic depletion and disjoining pressure – trapping of kinesin head on the MT. During each step, one of the kinesin heads detaches from the MT. This event requires energy; it is coupled with hydrolysis of the ATP molecule at the detaching head [187]. Work is performed against the

Table 4.3: Estimation of the influence of osmotic pressure Π on the energy required for detachment of kinesin head from the MT in polymer solutions. Data on Π for 6k PEG taken from [191]; for other polymers Π was calculated as for the ideal case – some underestimation is therefore probable. ΔG was obtained as volume expansion work performed against pressure Π over a volume corresponding to a cylinder of radius equal to kinesin head hydrodynamic radius (2.5 nm) and height of the polymer coil's diameter.

Solution	Concentration [% w/w]	Π [kPa]	$\Delta G[k_{\mathrm{B}}T]$
PEG 6k	5.0	0.53	1.09
	7.5	1.38	1.84
	10.0	2.63	5.41
	14.0	4.91	10.11
PEG 18k	3.0	0.041	0.15
	5.0	0.068	0.25
	10.0	0.14	0.51
PEG 1M	0.25	$6.1 \cdot 10^{-5}$	$2.3 \cdot 10^{-3}$
	0.5	$1.2 \cdot 10^{-4}$	$4.5 \cdot 10^{-3}$
	1.0	$2.5 \cdot 10^{-4}$	$9.0 \cdot 10^{-3}$
	2.0	$4.9 \cdot 10^{-4}$	$1.8 \cdot 10^{-2}$

disjoining pressure. It accounts not only for breaking the non-covalent bonds between the head and MT (this energy should not vary significantly upon addition of polymer), but also for the depletion interactions [99, 102, 188, 190]. When the head incrementally moves away from the MT, free space is created between these two surfaces, which is instantaneously filled by solvent molecules. However, large crowders cannot penetrate this space due to steric limitations. The arising gradient of osmotic pressure pushes the surfaces back together.

The depletion-dependent energetic barrier ΔG for separation of kinesin head and MT can be crudely estimated as comparable to ΠdV. Π is the difference in osmotic pressure [191] between the polymer solution and pure buffer; dV corresponds to the volume of a cylinder of radius equal to kinesin head hydrodynamic radius (2.5 nm) and height of the polymer coil's diameter. Thus estimated barrier in a 10% solution of 18k PEG (where kinesin is stopped) is 0.4 $k_{\mathrm{B}}T$, while for a 10% solution of 6k PEG (where enzymatic activity is retained) the calculations give 5.4 $k_{\mathrm{B}}T$. A difference in energy of more than an order of magnitude between

the two cases, coupled with an effect contrary to the expected, suggests that the depletion-related barrier is not the key issue. Moreover, the aforementioned values (as well as those calculated for other investigated systems, compiled in Table 4.3) are well below the energy obtained from hydrolysis of a single ATP molecule, *i.e.* 20–25 $k_{\mathrm{B}}T$.

Hypothesis 3: Poor availability of ATP due to its hindered diffusion. Combining Equation 1.28 with the Stokes-Sutherland-Einstein equation, the diffusion rates of ATP molecules in the investigated solutions were estimated. On this basis, the root mean square displacement of an ATP molecule during kinesin's dwell time (10 ms) was calculated. The minimum obtained value of *ca.* 1.5 μm was found for the 45% sucrose solution. As at 1 mM (standard experimental conditions) there are *ca.* $6 \cdot 10^5$ ATP molecules per $\mu\mathrm{m}^3$, the influence of hindered ATP diffusion on kinesin mobility seems highly improbable. Also, no change in the stall viscosity limit was observed upon the increase of ATP concentration to 10 mM.

Hypothesis 4: Limitations imposed on the diffusion of kinesin head. It is well documented that Brownian motion of the unbound head is crucial for the kinesin motion [120, 125, 126, 133]. Although the motor takes up to 100 steps per second (*i.e.* one step per 10 ms), most of this time is the dwell time, when the MT-bound head is waiting for ATP [126, 187] (state **1** in Figure 4.16). A single step requires displacement of the head over a distance of 16 nm. Within the simplistic model of the kinesin head treated as a sphere of hydrodynamic radius of 2.5 nm freely diffusing in a liquid of $\eta_{\mathrm{eff}} = 5$ mPa·s (boundary of stall conditions), it covers such distance in less that 4 μs. This is far below the expected step duration. However, such model neglects the fact that the diffusing head is connected to the other one, which is bound to the MT. To take a step, kinesin needs to stretch: molecular dynamics simulations suggest a tension of up to 15–35 pN arising in the linker [192, 193]. According to Hyeon and Onuchic [192], the linker is extended by 3.1±0.8 nm. From an approximation of a worm-like chain,

a spring constant $K = 5$ mN·m^{-1} is estimated. A model of particle diffusing in a harmonic potential field based on a simplified solution of the Smoluchowski equation can be applied: [194]

$$P(x) = (K/2\pi k_{\mathrm{B}}T) \exp\left(-Kx^2/2k_{\mathrm{B}}T\right), \tag{4.7}$$

where P is the probability of finding the particle at the distance x away from the equilibrium position. Integrating this equation over $x > 3.1$ nm, we obtain a probability of finding the unbound head at sufficient distance from the MT-bound one of only *ca.* 0.03%.

The estimated energy required to stretch the linker is 4 $k_{\mathrm{B}}T$ [192], which poses a barrier for reaching the binding site. Diffusion is also an activated process, characterized by a specific, Arrhenius-like activation energy (see Section 1.3). As described in detail in Section 4.1, an increase of viscosity of a solution by addition of a crowding agent is equivalent to the increase of the activation energy for diffusion. It can be expressed as $\eta_{\mathrm{eff}} = \eta_0 \exp\left(\Delta E_{\mathrm{a}}(RT)^{-1}\right)$, where ΔE_{a} is the difference in activation energy for viscous flow between solution and pure solvent. A 5-fold increase of the effective viscosity corresponds to a rise of ΔE_{a} by nearly 4 kJ/mol, which is *ca.* 1.6 $k_{\mathrm{B}}T$ in molecular terms.

The increase of ΔE_{a} may impair the functionality of kinesin. Energy obtained from ATP hydrolysis is used to detach one of the kinesin heads from the MT and induce conformational changes in the protein, while the rest of it is dissipated. Although the 4 $k_{\mathrm{B}}T$ of potential energy stored in the strained neck is released when the trailing head unbinds from the MT, its contribution to the directional head displacement is limited due to fast draining of momentum through Brownian motions of surrounding particles. The energy required for overcoming the barrier for motion and stretching the linker comes therefore mostly from the thermal motions, and not from the ATP dissociation.

There is also a strict time limit for overcoming the barrier. According to the presumed chemomechanical cycle [187], transition between states **1** and **2** in

Figure 4.16 is reversible. Rate of the **2**→**3** step, including the diffusion of head, is estimated to be 600 s^{-1} in optimal conditions [187]. Rate of ATP dissociation from the leading head (**2**→**1**) is *ca.* 100 s^{-1}. Increased effective viscosity hinders the **2**→**3** transition, while it does not affect the **2**→**1** reaction. This may lead to a situation where the head-ATP complex preferably dissociates before the step occurs and the ATP-ase activity is suppressed.

The arguments listed above constitute a coherent explanation of the observed kinesin stall. Hypothesis concerning the crucial importance of the limitations imposed on the diffusion of kinesin head by increase of η_{eff} is therefore strongly supported.

The results presented in this Section are described within a paper which at the moment of submission of this Thesis is under external editorial review.

Chapter 5

Summary and Conclusions

Biochemistry, biophysics and molecular biology brought in the last decades many crucial answers concerning the structure and functions of the basic gears of the molecular machinery of life. A lot is also known about the chemical pathways connecting these gears into functional organisms. However, understanding the dynamics of living systems is a remaining challenge: there still are significant shortcomings in the description of kinetics, regulation and synchronisation in biological systems within the strict framework of physics and thermodynamics. One of the most general factors influencing such processes is molecular mobility. Ever since the experiments of Schachman and Harrington in the 1950s [64], it is known that diffusion rates in complex liquids are length-scale-dependent. The recently proposed viscosity scaling paradigm [92, 95–97] is a basis for quantitative explanation of the apparent enhancement of mobility (*i.e.* decrease of effective viscosity) for small probes. Even though the basic studies usually utilize polymer systems as model complex liquids (which provide better control and easier parametrization than *in vivo* studies), it has been shown that the resultant scaling equations can be successfully applied to living cells [97, 195].

Within this Thesis, polymer model systems are exploited to demonstrate and describe several related phenomena concerning the dynamics of complex liquids at the nanoscale. The results are not only a contribution to the polymer science,

but may also have important biophysical implications. In the paragraphs below, the results are summed up according to the division adopted in the initial theses (page XVI) and placed in a broader context.

1. As was first suggested by Eyring [20, 21] in the 1930s, both diffusion and viscous flow can be treated as activated processes, characterized by a given value of activation energy, E_a – similarly as *e.g.* chemical reactions. Such classic approach is merged in this Thesis with the viscosity scaling paradigm. The experimental focus is on flow and probe diffusion in polymer systems, studied by means of fluorescence correlation spectroscopy and rheometry in aqueous polyethylene glycol solutions. Careful measurements of effective viscosity as a function of temperature allowed to establish the excess of E_a over the value characteristic for the pure solvent (ΔE_a) for different molecular probes as well as for the macroscopic flow. The activation energy for diffusion in polymer solutions proved to depend on the structure of the system (Equation 4.5). Probes which are small enough with respect to the characteristic length-scales of the liquid experience an activation energy similar as in pure solvent (ΔE_a close to zero). ΔE_a increases with the probe size, r_p. For r_p significantly larger than the hydrodynamic radius of the polymer chain, ΔE_a reaches a limit corresponding to the value measured for the macroscopic flow. For instance, the value of ΔE_a calculated for rhodamine in 3% PEG 500k solution (small probe/long polymer chains) is *ca.* 1.1 kJ/mol, for apoferritin (larger probe) in the same polymer solution it reaches 6.3 kJ/mol, while for macroscopic flow ΔE_a is *ca.* 12 kJ/mol.

   As has been shown previously, mobility scaling equations can be transferred from PEG solutions to other complex liquids, such as micellar systems or even living cell cytoplasm [97]. In cytoplasm, mobility of macromolecules is mostly influenced by high concentration of proteins [195], as well as by presence of the DNA [196] and cytoskeleton [197]. All these physical „obsta-

cles" can be included in the simplified geometric description of the structure of the complex liquid, allowing for application of the scaling equation to such systems. Significant increase of ΔE_a over the one predicted by the presented benchmark formula should imply molecular association processes, hindering the motion. On the other hand, molecular traffic in cells is in fact an interplay between the spontaneous diffusion and active transport [198]. The work exerted in the active process can be inferred from the comparison of the measured and predicted (for the purely Brownian motion) ΔE_a values. Confrontation of the work done with the total amount of energy used for the motion enhancement (which can be monitored *e.g.* via ATP usage in a number of enzyme-based systems [199]) should enable the determination of the intrinsic energy dissipation – which in turn allows for estimation of the molecular motor efficiency. Furthermore, application of the fluctuation-dissipation theorem and Stokes' law leads to a dependence between E_a and the power, P, of a motor moving at a constant velocity, u: $P \propto u^2 \exp(E_a/(RT))$. Utilization of the notion of activation energy for mobility in complex liquids may therefore provide a new insight into the description of molecular transport – both passive and active – and improve the understanding and modelling of dynamic processes in different diffusion-controlled systems.

2. According to Equation 1.6, viscous stress in a liquid is related to the *rate of change* of deformation of the system. However, there is another contribution to the total stress within a flow, which is attributed to the elasticity of the liquid. The rate of relaxation of the system to the equilibrium state after a mechanical disturbance may have a crucial impact on the motion in complex liquids, especially at short length-scales. This phenomenon was studied here in polymer solutions by means of a novel technique, based on observation of decay of oscillations of a piezoelectric resonator – quartz tuning fork (QTF).

The QTF is as a macroscopic object (mm scale – approximation of a flat wall) moving in a polymer solution at nanoscopic amplitudes. Viscosity measurements performed using a QTF oscillating at different amplitudes (covering nearly three orders of magnitude and crossing the key length-scales in polymer solutions: coil radius and correlation length) revealed no dependence of the experienced viscosity on the amplitude. In solutions of relatively short polymer chains, bulk viscosity was well reproduced. In case of high-M_w polymers, a significant (even 50-fold) decrease of QTF-measured viscosity versus the bulk value was observed. Dynamic light scattering was applied to capture the internal dynamics of the polymer mesh and correlated the drop of the effective viscosity with the mobility of mesh segments and thickness of the depletion layer. It was proved that if the relaxation of the polymer system is overrun by the motion of the fork, the DL/bulk boundary can be treated as stationary and the oscillator measures the viscosity of the depletion layer. Furthermore, at high oscillation amplitudes a significant broadening of the DL can be forced, as the polymer chains are pushed away from the QTF surface. Due to slow diffusion of segments of heavily entangled mesh of long polymer chains, the DL does not return to its equilibrium thickness until the oscillation amplitude drops well below R_g.

Experimental observation of the dynamic properties of the depletion layer proves that not only the length-scale domain should be considered in the description of the structure of complex liquids, but – in case of any dynamic systems – also the time domain. This opens a perspective for new studies on the dynamics in nanorheology as well as in-depth analysis of the nature of slow relaxation modes in polymer systems. The presented paradigm should also prove important in research on micro- and nanosized machines operating in crowded environment; both the engineered and natural ones (mechanoenzymes). If the rate of the repetitive/oscillating motion of such machines was high enough to overrun the relaxation dynamics of the surrounding mesh,

they should experience greatly reduced mechanical resistance of the environment. This would result in the facilitated operation of the machines and lower energy consumption.

3. Even minor changes of the effective viscosity may have a determining influence on functioning of the molecular machines. As demonstrated in this Thesis, processive motion of kinesin – a model motor protein, ubiquitous in eukaryotic cells – is utterly stopped at η_{eff} of *ca.* 5 mPa·s. Importantly, the enzyme retains its functionality even in solutions of viscosity higher than this value even by orders of magnitude, on condition that the crowders are much larger than the motor domain. This is the reason why the viscosity-related stall of kinesin has not been noted in previous studies of kinesin working against viscous load [130, 131]: they mostly relied on high-M_{w} polymer solutions, wherein η_{eff} for the motor domain is in fact similar as in pure solvent.

   Hindrance of the diffusive motion of the kinesin head at increased η_{eff} causes a shift of the pseudoequilibrium in the mechanochemical cycle of the motor step, effectively switching it off. The slowdown of diffusion can be described in terms of increase of activation energy for motion. Such phenomenon is not observed *in vivo*, as viscosity experienced by a kinesin head in the cytoplasm of an eukaryotic cell is of the order of 2-4 mPa·s [97]. On the other hand, in the much more congested prokaryotic cells, tubulin/kinesin active transport system is not present (specific cases of introduction via horizontal gene transfer were observed in bacteria, however with no mechanochemical activity) [200]. The presented results strongly support the kinesin stepping mechanism, wherein transfer of the head to the subsequent binding site on the MT relies on diffusion. In a broader perspective, the case of kinesin demonstrates the vital role of the viscosity scaling for description and design of micro- and nanomachines operating in crowded environment.

The conclusions listed above contribute to a better understanding of transport properties of complex fluids. Qualitatively new observations (scaling of activation energy for diffusion in polymer solutions, dynamic depletion layer, viscosity-related stall of kinesin) are quantitatively described and interpreted from a point of view of physical chemistry. However, they only constitute few pieces of a puzzle of dynamics in crowded environment, especially in the context of extreme chemical complexity of biological systems. It seems that the crucial direction of further studies is towards understanding the interactions in such systems: starting from general electrostatic attraction/repulsion between charged macromolecules, ending on mechanisms of molecular recognition. Any intermolecular interactions vastly influence the mobility – therefore, observation of mobility can be a convenient way to assess the strength and durability of the physical bonds. Phenomena such as viscosity scaling, depletion layer and relaxation-related effects need to be carefully taken into account in this sort of studies. This may open a perspective towards understanding not only the structure, but also the regulation and synchronization of biochemical pathways.

Bibliography

[1] T. Graham, in: H. Colburn, R. Bentley (editors), *The Quarterly Journal of Science, Literature and Art* (1829)

[2] H. Mehrer, N. Stolwijk, *Diffusion Fundamentals*, **11**:1 (2009)

[3] J. Philibert, *Diffusion Fundamentals*, **2**:1 (2005)

[4] A. Fick, *Phil. Mag.*, **10**:30 (1855)

[5] R. Brown, *Phil. Mag.*, **4**:161 (1827)

[6] R. Brown, *Phil. Mag.*, **6**(33):161 (1829)

[7] W. Sutherland, *Phil. Mag.*, **9**:781 (1905)

[8] A. Einstein, *Ann. Phys.*, **549**(17):549 (1905)

[9] A. Einstein, R. Fürth, *Investigations on the theory of the Brownian movement*, Dover Publications (1956)

[10] M. Smoluchowski, *Ann. Phys.*, **326**:756 (1906)

[11] M. Smoluchowski, *Prace Matematyczno-Fizyczne*, **25**(1):187 (1914)

[12] J. Perrin, *Les Atomes*, Alcan (1913)

[13] S. Chandrasekhar, *Rev. Mod. Phys.*, **21**:383 (1949)

[14] R. Huang, I. Chavez, K. M. Taute, B. Lukic, S. Jeney, M. G. Raizen, E.-L. Florin, *Nat. Phys.*, **7**:576 (2011)

[15] P. N. Pusey, *Science*, **332**(6031):802 (2011)

[16] J. Li, T. Ngai, C. Wu, *Polym. J.*, **42**(8):609 (2010)

[17] A. D. McNaught, A. Wilkinson (editors), *IUPAC. Compendium of Chemical Terminology, 2nd ed.*, Blackwell Scientific Publication (1997)

[18] P. W. Atkins, *Physical Chemistry, 7th Edition*, Oxford University Press (2006)

[19] S. Arrhenius, *Z. Physik. Chem.*, **4**:226 (1889)

[20] H. Eyring, *J. Chem. Phys.*, **4**:283 (1936)

[21] H. Eyring, J. Hirschfelder, *J. Phys. Chem.*, **41**(2):249 (1937)

[22] P. B. Macedo, T. A. Litovitz, *J.Chem. Phys.*, **42**(1):245 (1965)

[23] W. Kauzmann, H. Eyring, *J. Am. Chem. Soc.*, **62**(11):3113 (1940)

[24] R. E. Powell, W. E. Roseveare, H. Eyring, *Ind. Eng. Chem.*, **33**(4):430 (1941)

[25] D. Turnbull, M. H. Cohen, *J. Chem. Phys.*, **52**(6):3038 (1970)

[26] H. Guangze, F. Zengke, C. Mingdong, *Sci. China Ser. G*, **53**(10):1853 (2010)

[27] J. H. Wang, C. V. Robinson, I. S. Edelman, *J. Am. Chem. Soc.*, **75**(2):466 (1953)

[28] L. G. Longsworth, *J. Phys. Chem.*, **58**(9):770 (1954)

[29] S. Morioka, M.-H. Sun, *J. Non-Cryst. Solids*, **355**(4-5):287 (2009)

[30] I. Avramov, *Phys. Chem. Glasses-B*, **48**(1):61 (2007)

[31] J.-L. Barrat, J.-P. Hansen, *Basic Concepts for Simple and Complex Liquids*, Cambridge University Press (2003)

[32] P. Flory, *Principles of Polymer Chemistry*, Baker Lectures 1948, Cornell University Press (1953)

[33] H. Staudinger, *Berichte der Deutschen Chemischen Gesellschaft*, **53**(6):1073 (1920)

[34] M. Doi, S. Edwards, *The Theory of Polymer Dynamics*, Clarendon Press (1986)

[35] I. Teraoka, *Polymer Solutions: An Introduction to Physical Properties*, Wiley (2002)

[36] T. Tadros, *Encyclopedia of Colloid and Interface Science*, Springer (2013)

[37] P.-G. de Gennes, *Scaling Concepts in Polymer Physics*, Cornell University Press (1979)

[38] B. H. Zimm, *J. Chem. Phys.*, **24**(2):269 (1956)

[39] Y. Heo, R. G. Larson, *J. Rheol.*, **49**(5):1117 (2005)

[40] P. Flory, *Principles of Polymer Chemistry*, Cornell University Press (1971)

[41] A. Dondos, C. Tsitsilianis, G. Staikos, *Polymer*, **30**(9):1690 (1989)

[42] R. S. Cheng, *Macromol. Symp.*, **124**:27 (1997)

[43] C. Wu, *J. Polym. Sci. Pol. Phys.*, **32**(8):1503 (1994)

[44] A. Dondos, C. Tsitsilianis, *Polym. Int.*, **28**(2):151 (1992)

[45] A. Dondos, D. Papanagopoulos, *Polymer*, **36**(2):365 (1995)

[46] E. C. Cooper, P. Johnson, A. M. Donald, *Polymer*, **32**(15):2815 (1991)

[47] Q. Ying, B. Chu, *Macromolecules*, **20**(2):362 (1987)

[48] J. P. Cotton, M. Nierlich, F. Boue, M. Daoud, B. Farnoux, G. Jannink, R. Duplessix, C. Picot, *J. Chem. Phys.*, **65**(3):1101 (1976)

[49] W. W. Graessley, *Polymer*, **21**(3):258 (1980)

[50] G. C. Berry, H. Nakayasu, T. G. Fox, *J. Polym. Sci. Pol. Phys.*, **17**(11):1825 (1979)

[51] A. Wisniewska, K. Sozanski, T. Kalwarczyk, K. Kedra-Krolik, C. Pieper, S. A. Wieczorek, S. Jakiela, J. Enderlein, R. Holyst, *Polymer*, **55**(18):4651 (2014)

[52] R. P. Wool, *Macromolecules*, **26**(7):1564 (1993)

[53] M. Rief, M. Gautel, F. Oesterhelt, J. M. Fernandez, H. E. Gaub, *Science*, **276**(5315):1109 (1997)

[54] F. Rico, A. Rigato, L. Picas, S. Scheuring, *J. Nanobiotechnology*, **11**(Suppl 1):S3 (2013)

[55] F. Oesterhelt, M. Rief, H. E. Gaub, *New J. Phys.*, **1**(1):6 (1999)

[56] W. Schärtl, *Light Scattering from Polymer Solutions and Nanoparticle Dispersions*, Springer (2007)

[57] M. Adam, M. Delsanti, *Macromolecules*, **10**(6):1229 (1977)

[58] Y. Cheng, R. K. Prud'homme, J. L. Thomas, *Macromolecules*, **35**(21):8111 (2002)

[59] O. W. Webster, *Science*, **251**(4996):887 (1991)

[60] R. Stepto, *Pure Appl. Chem.*, **81**(2):351 (2009)

[61] K. Dill, S. Bromberg, *Molecular Driving Forces: Statistical Thermodynamics in Chemistry and Biology*, Garland Publishing (2003)

[62] E. Frey, K. Kroy, *Ann. Phys.*, **14**(1-3):20 (2005)

[63] R. Kubo, *Rep. Prog. Phys.*, **29**(1):255 (1966)

[64] H. K. Schachman, W. F. Harrington, *J. Am. Chem. Soc.*, **74**(15):3965 (1952)

[65] T. C. Laurent, A. Pietruszkiewicz, *Biochim. Biophys. Acta*, **49**(2):258 (1961)

[66] D. Langevin, F. Rondelez, *Polymer*, **19**(8):875 (1978)

[67] M. R. Wattenbarger, V. A. Bloomfield, Z. Bu, P. S. Russo, *Macromolecules*, **25**(20):5263 (1992)

[68] M. Tokita, T. Miyoshi, K. Takegoshi, K. Hikichi, *Phys. Rev. E*, **53**(2):1823 (1996)

[69] T. F. Kosar, R. J. Phillips, *AIChE J.*, **41**(3):701 (1995)

[70] A. Chrambac, D. Rodbard, *Science*, **172**(3982):440 (1971)

[71] S. P. Radko, A. Chrambach, *Electrophoresis*, **17**(6):1094 (1996)

[72] D. Rodbard, A. Chrambac, *Anal. Biochem.*, **40**(1):95 (1971)

[73] G. D. J. Phillies, G. S. Ullmann, K. Ullmann, T. H. Lin, *J. Chem. Phys.*, **82**(11):5242 (1985)

[74] T. Odijk, *Biophys. J.*, **79**(5):2314 (2000)

[75] A. R. Altenberger, M. Tirrell, *J. Chem. Phys.*, **80**(5):2208 (1984)

[76] B. Amsden, *Polymer*, **43**(5):1623 (2002)

[77] R. I. Cukier, *Macromolecules*, **17**(2):252 (1984)

[78] G. D. J. Phillies, *J. Non-Cryst. Solids*, **131**(Part 2):612 (1991)

[79] G. D. J. Phillies, W. Brown, P. Zhou, *Macromolecules*, **25**(19):4948 (1992)

[80] G. D. J. Phillies, D. Clomenil, *Macromolecules*, **26**(1):167 (1993)

[81] F. B. Wyart, P. G. de Gennes, *Eur. Phys. J. E*, **1**(1):93 (2000)

[82] A. G. Ogston, *T. Faraday Soc.*, **54**(11):1754 (1958)

[83] J. Stone-Masui, A. Watillon, *J. Colloid Interf. Sci.*, **28**(2):187 (1968)

[84] S. P. Meeker, W. C. K. Poon, P. N. Pusey, *Phys. Rev. E*, **55**:5718 (1997)

[85] J. C. van der Werff, C. G. de Kruif, *J. Rheol.*, **33**(3) (1989)

[86] P. N. Segrè, S. P. Meeker, P. N. Pusey, W. C. K. Poon, *Phys. Rev. Lett.*, **75**:958 (1995)

[87] J. Szymanski, A. Patkowski, A. Wilk, P. Garstecki, R. Holyst, *J. Phys. Chem. B*, **110**(51):25593 (2006)

[88] I. V. Nesmelova, V. D. Skirda, V. D. Fedotov, *Biopolymers*, **63**(2):132 (2002)

[89] T. Kalwarczyk, K. Sozanski, S. Jakiela, A. Wisniewska, E. Kalwarczyk, K. Kryszczuk, S. Hou, R. Holyst, *Nanoscale*, **6**:10340 (2014)

[90] M. Elowitz, M. Surette, P. Wolf, J. Stock, S. Leibler, *J. Bacteriol.*, **181**(1):197 (1999)

[91] G. Lukacs, P. Haggie, O. Seksek, D. Lechardeur, N. Freedman, A. Verkman, *J. Biol. Chem.*, **275**(3):1625 (2000)

[92] A. Tuteja, M. E. Mackay, S. Narayanan, S. Asokan, M. S. Wong, *Nano Lett.*, **7**(5):1276 (2007)

[93] J. Liu, D. Cao, L. Zhang, *J. Phys. Chem. C*, **112**(17):6653 (2008)

[94] I. Kohli, A. Mukhopadhyay, *Macromolecules*, **45**(15):6143 (2012)

[95] R. Holyst, A. Bielejewska, J. Szymanski, A. Wilk, A. Patkowski, J. Gapinski, A. Zywocinski, T. Kalwarczyk, E. Kalwarczyk, M. Tabaka, N. Ziebacz, S. A. Wieczorek, *Phys. Chem. Chem. Phys.*, **11**(40):9025 (2009)

[96] L.-H. Cai, S. Panyukov, M. Rubinstein, *Macromolecules*, **44**(19):7853 (2011)

[97] T. Kalwarczyk, N. Ziebacz, A. Bielejewska, E. Zaboklicka, K. Koynov, J. Szymanski, A. Wilk, A. Patkowski, J. Gapinski, H.-J. Butt, R. Holyst, *Nano Lett.*, **11**(5):2157 (2011)

[98] J. F. Joanny, L. Leibler, P.-G. de Gennes, *J. Polym. Sci. Pol. Phys.*, **17**(6):1073 (1979)

[99] H. Lekkerkerker, R. Tuinier, *Colloids and the Depletion Interaction*, Springer (2011)

[100] F. Oosawa, S. Asakura, *J. Chem. Phys.*, **22**(7):1255 (1954)

[101] P. Jenkins, M. Snowden, *Adv. Colloid. Interfac. Sci.*, **68**:57 (1996)

[102] S. Asakura, F. Oosawa, *J. Polym. Sci.*, **33**(126):183 (1958)

[103] R. Tuinier, J. K. G. Dhont, T. H. Fan, *Europhys. Lett.*, **75**(6):929 (2006)

[104] S. Hou, N. Ziebacz, T. Kalwarczyk, T. S. Kaminski, S. A. Wieczorek, R. Holyst, *Soft Matter*, **7**(7):3092 (2011)

[105] T.-H. Fan, J. K. G. Dhont, R. Tuinier, *Phys. Rev. E*, **75**:011803 (2007)

[106] R. Tuinier, T.-H. Fan, T. Taniguchi, *Curr. Opin. Colloid In.*, **20**(1):66 (2015)

[107] T. Odijk, *Physica A*, **337**(3):389 (2004)

[108] A. Ochab-Marcinek, R. Holyst, *Soft Matter*, **7**(16):7366 (2011)

[109] A. Ochab-Marcinek, S. A. Wieczorek, N. Ziebacz, R. Holyst, *Soft Matter*, **8**(43):11173 (2012)

[110] N. Ziebacz, S. A. Wieczorek, T. Kalwarczyk, M. Fialkowski, R. Holyst, *Soft Matter*, **7**:7181 (2011)

[111] B. Vincent, *Colloid. Surface.*, **50**:241 (1990)

[112] G. J. Fleer, A. M. Skvortsov, R. Tuinier, *Macromolecules*, **36**(20):7857 (2003)

[113] T. Odijk, *Macromolecules*, **29**(5):1842 (1996)

[114] C. Allain, D. Ausserre, F. Rondelez, *Phys. Rev. Lett.*, **49**(23):1694 (1982)

[115] D. Ausserre, H. Hervet, F. Rondelez, *Macromolecules*, **19**(1):85 (1986)

[116] D. Ausserre, J. Edwards, J. Lecourtier, H. Hervet, F. Rondelez, *Europhys. Lett.*, **14**(1):33 (1991)

[117] A. Cuenca, H. Bodiguel, *Phys. Rev. Lett.*, **110**(10):108304 (2013)

[118] H. Lodish, A. Berk, S. L. Zipursky, *Molecular Cell Biology. 4th edition.*, W. H. Freeman, New York (2000)

[119] G. Woehlke, M. Schliwa, *Nat. Rev. Mol. Cell Bio.*, **1**(1):50 (2000)

[120] S. M. Block, *Biophys. J.*, **92**(9):2986 (2007)

[121] N. Hirokawa, R. Takemura, *Exp. Cell Res.*, **301**(1):50 (2004)

[122] David S. Goodsell, *PDB Molecule of the Month*, April 2005, DOI: 10.2210/rcsb_pdb/mom_2005_4

[123] F. Kozielski, D. Svergun, G. Zaccai, R. Wade, M. Koch, *J. Biol. Chem.*, **276**(2):1267 (2001)

[124] K. Svoboda, S. M. Block, *Cell*, **77**(5):773 (1994)

[125] M. Nishiyama, H. Higuchi, T. Yanagida, *Nat. Cell Biol.*, **4**(10):790 (2002)

[126] N. Carter, R. Cross, *Nature*, **435**(7040):308 (2005)

[127] E. Toprak, A. Yildiz, M. T. Hoffman, S. S. Rosenfeld, P. R. Selvin, *P. Natl. A. Sci. USA*, **106**(31):12717 (2009)

[128] C. M. Coppin, D. W. Pierce, L. Hsu, R. D. Vale, *P. Natl. Acad. Sci. USA*, **94**(16):8539 (1997)

[129] H. Kojima, E. Muto, H. Higuchi, T. Yanagida, *Biophys. J.*, **73**(4):2012 (1997)

[130] A. J. Hunt, F. Gittes, J. Howard, *Biophys. J.*, **67**(2):766 (1994)

[131] J. Gagliano, M. Walb, B. Blaker, J. C. Macosko, G. Holzwarth, *Eur. Biophys. J. Biophy.*, **39**(5):801 (2010)

[132] B. Gutiérrez-Medina, A. N. Fehr, S. M. Block, *P. Natl. Acad. Sci. USA*, **106**(40):17007 (2009)

[133] W. R. Schief, J. Howard, *Curr. Opin. Cell Biol.*, **13**(1):19 (2001)

[134] C. L. Asbury, A. N. Fehr, S. M. Block, *Science*, **302**(5653):2130 (2003)

[135] A. Yildiz, M. Tomishige, R. D. Vale, P. R. Selvin, *Science*, **303**(5658):676 (2004)

[136] Q. Shao, Y. Q. Gao, *Proc. Natl. Acad. Sci. USA*, **103**(21):8072 (2006)

[137] S. Rice, A. W. Lin, D. Safer, C. L. Hart, N. Naber, B. O. Carragher, S. M. Cain, E. Pechatnikova, E. M. Wilson-Kubalek, M. Whittaker, *Nature*, **402**(6763):778 (1999)

[138] C. V. Sindelar, M. J. Budny, S. Rice, N. Naber, R. Fletterick, R. Cooke, *Nat. Struct. Mol. Biol.*, **9**(11):844 (2002)

[139] J. Yajima, R. A. Cross, *Nat. Chem. Biol.*, **1**(6):338 (2005)

[140] F. J. Kull, S. A. Endow, *J. Cell Sci.*, **126**(1):9 (2013)

[141] J. Howard, in: V. Rivasseau (editor), *Biological Physics*, 47–59, Springer (2011)

[142] A. U. Acuna, F. Amat-Guerri, P. Morcillo, M. Liras, B. Rodriguez, *Org. Lett.*, **11**(14):3020 (2009)

[143] G. G. Stokes, *Philos. T. R. Soc. Lond.*, **142**:463 (1852)

[144] B. Valeur, *Molecular Fluorescence: Principles and Applications*, Wiley-WCH (2001)

[145] J. Lakowicz, *Principles of Fluorescence Spectroscopy*, Springer (2006)

[146] S. J. Mulligan, B. A. MacVicar, A. Méndez-Vilas, J. Díaz, *Modern Research and Educational Topics in Microscopy*, 881–889 (2007)

[147] J. B. Johnson, *Phys. Rev.*, **32**:97 (1928)

[148] H. Nyquist, *Phys. Rev.*, **32**:110 (1928)

[149] D. Magde, E. Elson, W. W. Webb, *Phys. Rev. Lett.*, **29**:705 (1972)

[150] E. L. Elson, D. Magde, *Biopolymers*, **13**(1):1 (1974)

[151] O. Krichevsky, G. Bonnet, *Rep. Prog. Phys.*, **65**(2):251 (2002)

[152] J. Enderlein, I. Gregor, *Rev. Sci. Instrum.*, **76**(3):033102 (2005)

[153] D. Axelrod, *Traffic*, **2**(11):764 (2001)

[154] T. Mezger, *The Rheology Handbook: For Users of Rotational and Oscillatory Rheometers*, Vincentz Network (2006)

[155] S. W. Provencher, *Comput. Phys. Commun.*, **27**(3):229 (1982)

[156] X. D. Su, C. C. Dai, J. Zhang, S. J. O'Shea, *Biosens. Bioelectron.*, **17**(1-2):111 (2002)

[157] X. Zhou, T. Jiang, J. Zhang, X. Wang, Z. Zhu, *Sensor. Actuator. B-Chem.*, **123**(1):299 (2007)

[158] F. J. Giessibl, M. Herz, J. Mannhart, *Proc. Natl. Acad. Sci. USA*, **99**(19):12006 (2002)

[159] L. F. Matsiev, in: S. C. Schneider, M. Levy, B. R. McAvoy (editors), *1999 IEEE Ultrasonics Symposium Proceedings*, 457–460 (1999)

[160] J. Zhang, C. C. Dai, X. D. Su, S. J. O'Shea, *Sensor. Actuator. B-Chem.*, **84**(2-3):123 (2002)

[161] Y. Liu, R. DiFoggio, K. Sanderlin, L. Perez, J. Zhao, *Sensor. Actuator. A-Phys.*, **167**(2, SI):347 (2011)

[162] K. Waszczuk, T. Piasecki, K. Nitsch, T. Gotszalk, *Sensor. Actuator. B-Chem.*, **160**(1):517 (2011)

[163] L. F. Matsiev, *2000 IEEE Ultrasonics Symposium Proceedings*, **1**:427 (2000)

[164] P. Wang, J. Fang, Y. Hou, X. Du, D.-M. Zhu, *J. Phys. Chem. C*, **113**(2):729 (2009)

[165] S. Qin, X. Tang, L. Zhu, Y. Wei, X. Du, D.-M. Zhu, *J. Colloid. Interf. Sci.*, **383**:208 (2012)

[166] H. Hosaka, K. Itao, S. Kuroda, *Sensor. Actuator. A-Phys.*, **49**:87 (1995)

[167] C. B. Muller, W. Richtering, *Colloid Polym. Sci.*, **286**:1215 (2008)

[168] K. Sozański, *Zastosowanie spektroskopii korelacji fluorescencji do pomiarów energii aktywacji dyfuzji w roztworach polimerów*, Master thesis, University of Warsaw (2013)

[169] N. G. Tsierkezos, I. E. Molinou, *J. Chem. Eng. Data*, **43**(6):989 (1998)

[170] E. Lemmon, M. Mclinden, D. Friend, *Thermophysical Properties Of Fluid Systems, NIST Chemistry Webbook, NIST Standard Reference Database Number 6*, National Institute Of Standards and Technology USA (2012)

[171] C. T. Culbertson, S. C. Jacobson, J. M. Ramsey, *Talanta*, **56**(2):365 (2002)

[172] P.-O. Gendron, F. Avaltroni, K. Wilkinson, *J. Fluoresc.*, **18**(6):1093 (2008)

[173] K. R. Rogers, S. Weiss, I. Crevel, P. J. Brophy, M. Geeves, R. Cross, *EMBO J.*, **20**(18):5101 (2001)

[174] T. Korten, B. Nitzsche, C. Gell, F. Ruhnow, C. Leduc, S. Diez, in: E. J. G. Peterman, G. J. L. Wuite (editors), *Single Molecule Analysis*, volume 783 of *Methods in Molecular Biology*, 121–137, Humana Press (2011)

[175] C. Gell, et al., in: L. Wilson, J. J. Correia (editors), *Microtubules, in vitro*, volume 95 of *Methods in Cell Biology*, 221 – 245, Academic Press (2010)

[176] F. Ruhnow, D. Zwicker, S. Diez, *Biophys. J.*, **100**(11):2820 (2011)

[177] K. Waszczuk, T. Piasecki, K. Nitsch, T. Gotszalk, *Meas. Sci. Technol.*, **24**(8):085304 (2013)

[178] Y. Qin, R. Reifenberger, *Rev. Sci. Instrum.*, **78**(6):063704 (2007)

[179] K. Devanand, J. C. Selser, *Macromolecules*, **24**(22):5943 (1991)

[180] K. Sozański, A. Wiśniewska, T. Kalwarczyk, R. Hołyst, *Phys. Rev. Lett.*, **111**(22):228301 (2013)

[181] J. H. Wang, *J. Am. Chem. Soc.*, **73**(2):510 (1951)

[182] T. Nicolai, W. Brown, S. Hvidt, K. Heller, *Macromolecules*, **23**(24):5088 (1990)

[183] J. Li, Y. Lu, G. Zhang, W. Li, C. Wu, *Chin. J. Polym. Sci.*, **26**(04):465 (2008)

[184] P. Stepanek, C. Konak, J. Jakes, *Polym. Bull.*, **16**(1):67 (1986)

[185] K. Sozanski, A. Wisniewska, T. Piasecki, K. Waszczuk, A. Ochab-Marcinek, T. Gotszalk, R. Holyst, *Soft Matter*, **10**(39):7762 (2014)

[186] T. Korten, S. Diez, *Lab Chip*, **8**(9):1441 (2008)

[187] B. E. Clancy, W. M. Behnke-Parks, J. O. L. Andreasson, S. S. Rosenfeld, S. M. Block, *Nat. Struct. Mol. Biol.*, **18**(9):1020 (2011)

[188] A. Kulkarni, A. Chatterjee, K. Schweizer, C. Zukoski, *J. Chem. Phys.*, **113**(21):9863 (2000)

[189] H.-X. Zhou, G. Rivas, A. P. Minton, *Ann. Rev. Biophys.*, **37**(1):375 (2008)

[190] Y. Mao, M. Cates, H. Lekkerkerker, *Physica A*, **222**(1 - 4):10 (1995)

[191] N. P. Money, *Plant Physiol.*, **91**(2):766 (1989)

[192] C. Hyeon, J. N. Onuchic, *P. Natl. Acad. Sci. USA*, **104**(7):2175 (2007)

[193] V. Hariharan, W. O. Hancock, *Cell. Mol. Bioeng.*, **2**(2):177 (2009)

[194] M. Lindner, G. Nir, A. Vivante, I. T. Young, Y. Garini, *Phys. Rev. E*, **87**(2) (2013)

[195] T. Kalwarczyk, M. Tabaka, R. Holyst, *Bioinformatics*, **28**(22):2971 (2012)

[196] M. K. Daddysman, C. J. Fecko, *J. Phys. Chem. B*, **117**(5):1241 (2013)

[197] E. Dauty, A. Verkman, *J. Biol. Chem.*, **280**(9):7823 (2005)

[198] I. Neri, N. Kern, A. Parmeggiani, *Phys. Rev. Lett.*, **110**:098102 (2013)

[199] H. Hess, V. Vogel, *Rev. Mol. Biotechnol.*, **82**(1):67 (2001)

[200] M. Pilhofer, A. P. Bauer, M. Schrallhammer, L. Richter, W. Ludwig, K.-H. Schleifer, G. Petroni, *Nucleic Acids Res.*, **35**(20) (2007)